Marco Ninghetto

Long-term loss of visual field in ophthalmological patients with central or peripheral degeneration of photoreceptors - fMRI analysis of visual cortex

PhD thesis
Completed in the Laboratory of Brain Imaging
of the Nencki Institute of Experimental Biology
Polish Academy of Sciences

SUPERVISOR
Dr. Kalina Burnat, Ph.D., D.Sc.

Warsaw, 2024

To my supervisor Dr. Kalina Burnat and my faithful colleagues, for their unwavering guidance.

To my blood family in Italy and my new Polish family, for their unshakable support.

To Kinga and Mira, cornerstones of my success. Unyielding forces of nature.

Oświadczenie autora

Ja, niżej podpisana(-y) Marco Ninghetto wyrażam zgodę na przechowywanie i udostępnianie mojej pracy doktorskiej pt.: "*Long-term loss of visual field in ophthalmological patients with central or peripheral degeneration of photoreceptors - fMRI analysis of visual cortex*" przez Bibliotekę Instytutu Biologii Doświadczalnej im. M. Nenckiego PAN w formie drukowanej, w czytelni oraz w ramach wypożyczeń międzybibliotecznych, na zasadach dozwolonego użytku. Jednocześnie udzielam Bibliotece Instytutu Biologii Doświadczalnej im. M. Nenckiego PAN nieodpłatnej licencji niewyłącznej na korzystanie z w. w. pracy bez ograniczeń czasowych i terytorialnych na następujących polach eksploatacji:

1) umieszczenie treści pracy w formie pliku pdf wraz z metadanymi, w repozytorium cyfrowym RCIN (Repozytorium Cyfrowe Instytutów Naukowych, kolekcja: Instytut Biologii Doświadczalnej PAN/ Prace dyplomowe) znajdującym się pod adresem: https://rcin.org.pl/dlibra/collectiondescription/121

2) zwielokrotnienie utworu techniką cyfrową (digitalizacja pracy w przypadku konieczności skanowania wersji drukowanej)

Warszawa, 20-01-2025

Badania opisane w niniejszej pracy zostały sfinansowane w ramach konsorcyjnego projektu badawczego Narodowego Centrum Nauki 2018/29/B/NZ4/02435 „Inputs from V5/MT to V1 in cortical reorganization triggered by Retinitis Pigmentosa: significance and functions.”

Table of Contents

Abstract

In the cortical representation of the visual field, receptive fields (RFs) form a gradient from small sizes in the center to the largest at the periphery. Center and peripheral cortical representation of the visual field differs functionally, center being engaged in sharp vision, whereas periphery in motion and attention. In this thesis I aim to analyze brain activity using functional MRI (fMRI) after visual field loss. The thesis is divided into two studies: first is devoted to the analysis of the receptive field (RF) adaptation in primary (V1), secondary (V2), and third (V3) cortical visual areas by population RF (pRF) mapping, second describes motion-based acuity by measuring individual thresholds and establishing whole-brain activations. We gathered two large groups of patients with long-term photoreceptors degeneration: Stargardt (STGD) with loss of the central retina and Retinitis Pigmentosa (RP) with loss in the peripheral retina. We also modelled peripheral vision loss in healthy participants by transiently limiting the visual field bilaterally to 10 degrees. In the first study, we found in V1, that the pRF size increased bilaterally in RP and controls in limited vision, as compared to the controls in full vision. In STDG, we found a clear separation between dorsal and ventral pRF responses, with pRF size increasing significantly only in the dorsal subdivision of V1. The response in V2 and V3 differed depending on the nature of the loss. Both controls in limited vision and RP patients showed a decrease in pRF size in V2 and V3. On the contrary, in STGD, we observed an increase in pRF size, not only in V1, but also in V2 and V3. Interestingly, in the STGD patients, this increase of pRF sizes was predominantly occurring within the dorsal subdivision of the visual cortex. In the second study, fMRI results indicated distinct functional impairments in RP patients that

differed from transient loss of peripheral vision in controls in limited vision. RP patients exhibited higher thresholds for motion-acuity tasks in negative contrast and fast velocity conditions. RP patients when tested in fMRI using the same motion-acuity test, showed significantly lower activations within the cortical representation of the peripheral visual field in V1-3, in line with the behavioral response to the fast velocity in negative contrast stimuli, likely reflecting peripheral vision loss. Outside the visual cortices, we also found higher responses of putamen and dorsal anterior cingulate cortex for the RP patients, likely pointing to a faster adaptation to new stimuli for long-term loss of vision compared to transient loss of vision in controls. Results described in the thesis provide further insight into the interplay between visual field loss and cortical reorganization, emphasizing the role of dorsal subdivisions in compensatory adaptations. The findings extend the understanding of visual system plasticity and possibly direct potential therapeutic approaches for STGD and RP treatments.

Abstract in Polish (streszczenie)

W korowej reprezentacji pola widzenia, pola recepcyjne (RF) tworzą gradient od małych rozmiarów w centrum do największych na peryferiach. Celem niniejszej pracy jest opisanie funkcjonalnych efektów utraty pola widzenia w dwóch badaniach: pierwsze dotyczy adaptacji pól recepcyjnych (RF) w okolicach V1, V2 i V3 z zastosowaniem mapowania polowych pól recepcyjnych (pRF), drugie badanie opisuje ostrość widzenia opartą na ruchu, mierząc behawioralnie ostrość widzenia i ustalając aktywacje mózgowe podczas pomiarów ostrości. Badania prowadzono z zastosowaniem funkcjonalnego rezonansu magnetycznego (fMRI) 3T, u pacjentów z wrodzoną degeneracją fotoreceptorów: w centralnej siatkówce u pacjentów ze Stargardtem (STGD) oraz w peryferycznej siatkówce u pacjentów z retinitis pigmentosa (RP, retinopatia barwnikowa). Modelowano również utratę widzenia peryferycznego u zdrowych osób poprzez przejściowe ograniczenie pola widzenia do 10 stopni. Wyniki badania pierwszego: 1. w okolicy V1 rozmiar pRF zwiększył się obustronnie w grupach RP i kontrolnej; 2. u pacjentów STGD zaobserwowaliśmy rozdzielenie odpowiedzi pRF w obszarach grzbietowym i brzusznym, badanych okolic wzrokowych, z istotnym powiększeniem rozmiaru pRF tylko w grzbietowej części okolicy V1. Zarówno kontrolni uczestnicy z przejściową utratą widzenia peryferycznego, jak i pacjenci RP z wrodzoną utratą widzenia peryferycznego wykazali istotne zmniejszenie rozmiaru pRF w okolicach V2 i V3. Przeciwnie, u pacjentów STGD, z utratą centralnego widzenia, zaobserwowano zwiększenie rozmiaru pRF, nie tylko w V1, ale także w V2 i V3. Co ciekawe, u pacjentów STGD wzrost rozmiaru pRF występował przede wszystkim w grzbietowych partiach kory wzrokowej. W drugim badaniu, otrzymane wyniki wskazują na wyraźne zaburzenia funkcjonalne u pacjentów

RP, które różnią się od przejściowej utraty widzenia obwodowego. Pacjenci RP wykazali istotnie mniejsze aktywacje w korowej reprezentacji obwodowego pola widzenia w okolicach V1-3, zgodnie z uzyskaną odpowiedzią behawioralną na wysoką prędkość w bodźcach o negatywnym kontraście. Poza korą wzrokową, zaobserwowano również wyższe odpowiedzi w jądrze ogoniastym i grzbietowej przedniej korze czołowej u pacjentów RP, co prawdopodobnie wskazuje na adaptację do nowych bodźców w przypadku długoterminowej utraty widzenia w porównaniu do przejściowej utraty widzenia. Wyniki opisane w pracy dostarczają dalszych informacji na temat współzależności między utratą pola widzenia, a reorganizacją korową, podkreślając rolę grzbietowych obszarów kory wzrokowej w adaptacjach kompensacyjnych. Odkrycia te poszerzają zrozumienie plastyczności układu wzrokowego i mogą inspirować potencjalne podejścia terapeutyczne do leczenia STGD i RP.

List of Abbreviations

aIC - anterior insular cortex

BOLD - evoked blood oxygenation level-dependent

dACC - dorsal anterior cingulate cortex

ERG - electroretinography

ETDRS - early treatment diabetic retinopathy study

fMRI - functional magnetic resonance imaging

FO - frontal operculum

FWE - family wise error

GLM - general linear model

MD - macular degeneration

mfERG - multi focal ERG

midFG - middle frontal gyrus

MNI - Montreal Neurological Institute

MT - middle temporal gyrus

MT+/V5 - middle temporal area

OCT - optical coherence tomography

PCC - posterior cingulate cortex

postCG - postcentral gyrus

preCG - precentral gyrus

pRF - population receptive field

RDK - random dots kinematogram

RF - receptive field

ROI - region of interest

RP - Retinitis Pigmentosa disease

SMA - supplementary motor area

SPM - statistical parametric mapping

STGD - Stargardt disease

supFG - superior frontal gyrus

supTG - superior temporal gyrus

suRF - single unit receptive field

V1 - primary visual cortex

V1d, V2d, V3d - dorsal portion of V1, V2, V3

V1v, V2v, V3v - ventral portion of V1, V2, V3

V2 - secondary visual area

V3 - third visual area

1. Introduction

1.1. Analysis of the visual field

The visual system ability to process and interpret visual stimuli is crucial for functions such as object recognition and reading. The visual field can be divided into distinct quadrants along the horizontal and vertical meridians, which are represented retinotopically across the retina and cortical visual areas. The division of the visual field into quadrants and its retinotopic representation across the retina and cortical visual areas, was first demonstrated through electrophysiological studies. Hubel and Wiesel (1968) used single-cell recordings in the primary visual cortex (V1) to reveal a precise mapping of the visual field, with the vertical meridian delineating the left and right visual fields and the horizontal meridian dividing the upper and lower fields. These findings were later repeated non-invasively with imaging techniques like fMRI (Sereno et al., 1995). Figure 1A shows a schematic representation of how the upper and lower visual field information is conveyed to the, in order, inferior and superior hemiretina: the horizontal line divides upper and lower visual field extents of the entire visual field; both are then reflected into the fovea where the image of the lower visual field occupies the superior retina, while the upper visual field image occupies the inferior retina. The image reversion takes place at the lens and retina. Lens, which, for its convexity, causes the light rays to converge and cross over leading to an upside-down projection of the image on the concave retina.

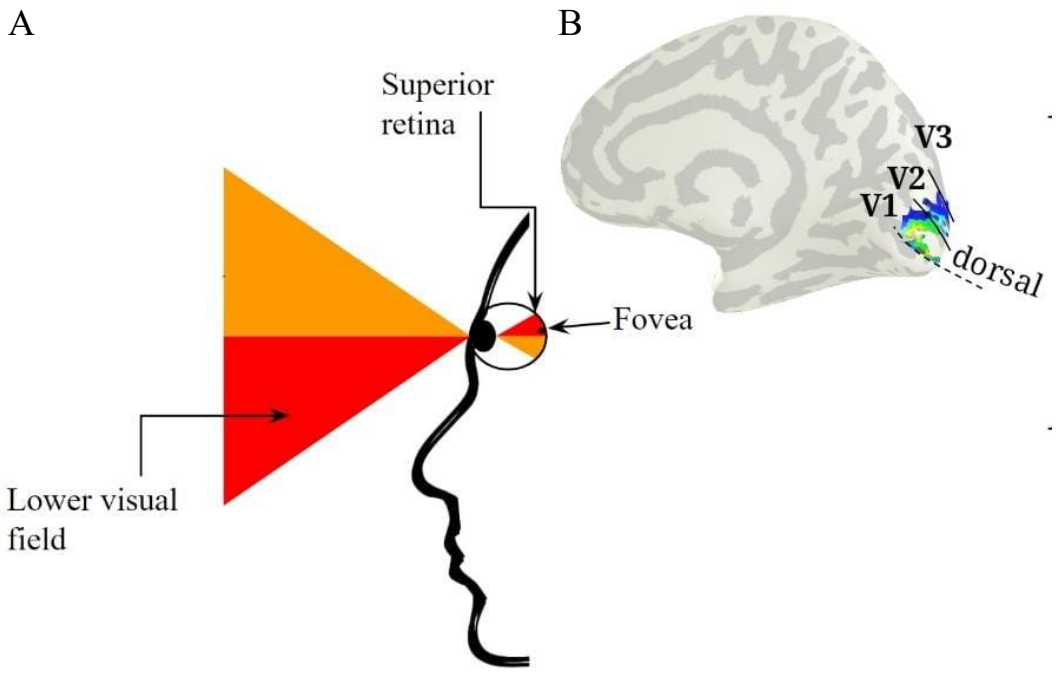

Figure 1. Illustration of the relationship between the visual field, the retina, and the dorsal subdivisions of V1-3 areas. (**A**) Schematic representation of upper and lower visual fields and its image on the retina. (**B**) The dorsal subdivisions of the visual cortex (V1-V3), shown at the inflated right hemisphere. The horizontal line is depicted by the long side of the orange and red triangles, illustrating the, in order, upper and lower visual fields. Both triangles are then reflected upside down into the fovea where the image of the lower visual field occupies the superior retina, while the upper visual field image occupies the inferior retina. The image reversion takes place at the lens, which, for its convexity, causes the light rays to converge and cross over, leading to an upside-down projection of the image on the retina. The lower visual field image projects reflection to the superior retina including fovea, which is transferred to the dorsal subdivisions of visual cortex. Note the location of the fovea in the superior hemiretina marked by black circle. Original figure, based on information learnt from the manual edited by Purves et al (2012, chapter *Vision: The Eye*).

The fovea, located within the superior retina, represents approximately 1–2° of the central part of the visual field (Wandell et al., 2007). Fovea is characterized by a high density of cones and the absence of blood vessels (Provis et al., 2005). Parafovea surrounds the fovea and covers ~2-5°, with a lower density of cones compared to the fovea, and increasing number of rods towards the perifovea. The perifovea covers 5-10° and has a progressively higher concentration of rods compared to fovea, starting to support low-light and peripheral vision functions (Curcio et al., 1990). Along this eccentricity gradient, from fovea to perifovea, the ganglion cell layer thickness

decreases, and the transition to the peripheral retina begins (Polyak, 1941). The fovea is situated at the center of the macula, a specialized retinal region spanning approximately 17–21° of the visual field (Curcio et al., 1990). For this thesis, as suggested earlier by Burnat (2015), we defined the central vision as the central 10° of the visual field.

The cortical representation of the visual field follows a gradient of cortical magnification, where central retinal representation, particularly fovea and parafovea, have disproportionately larger cortical representation as compared to the peripheral retina. This results in a proportionally larger surface of the visual cortex processing central 10 deg vision. Thanks to the cortical magnification factor the fine special processing of high-acuity tasks, essential for reading and recognizing faces are facilitated (Benson et al., 2021). The lower visual field is represented within the dorsal subdivisions of the cortical visual areas (Fig. 1B).

In primates, the precise representation of the very central 2 visual degrees remains not fully described, due to the microsaccades, the small, involuntary eye movements, present within fovea, even in conditions with controlled fixation. These eye movements persist even in anesthetized animals, therefore tracer studies offer most precise analysis of the fovea cortical organization. Last tracer studies in macaques have revealed continuous topographic connectivity across V1, V2, and V4 for the foveal visual field and only a weak connectivity with V3 without topographic continuity (Li et al., 2024). Beyond the foveal region (i.e., parafovea), Li et al. (2024) observed shifts in topographic organization and connectivity patterns, suggesting that functional and structural segregation becomes more prominent as visual field eccentricity increases, further from the foveal representation, in the dorsal and ventral subdivisions.

1.2. Retinal image

The retinal image of an object on which an observer is focusing attention is conveyed to the fovea, located in the superior part of the hemiretina (depicted with a small black dot shown in the superior retina in Fig. 1A). The fovea is the thinnest section of the retina, without blood vessels, and is approximately 0.3 mm thick. In this thin depression, light reaches the photosensitive layer of the photoreceptors - cones and rods - directly, as other retinal cells, including ganglion cells are displaced laterally (Chalupa & Werner, 2015). Cones, which dominate the fovea, are photoreceptor cells responsible for color vision and high-acuity vision, particularly in bright light conditions. There are three types of cones, each sensitive to different wavelengths of light: short (S), medium (M), and long (L), corresponding to blue, green, and red light, respectively. The combined input from cones allows the brain to perceive a spectrum of colors through color opponency, where signals from different cone types are compared to produce color contrasts (Chalupa & Werner, 2015). While the fovea is mostly populated by cone photoreceptors, the peripheral fovea contains a small number of rods, contributing to sensitivity in low-light conditions: this mixed photoreceptor population supports a balance between detailed daytime vision and peripheral night vision (Kolb, 2001). Rod photoreceptors are responsible for vision under low-light conditions, or scotopic vision (Rodieck, 1998). Unlike cones, which function best in bright light and contribute to color vision, rods are sensitive to light but do not detect color. They are concentrated in the peripheral retina and are crucial for detecting movement and shapes in dim environments (Chalupa & Werner, 2015). The signals from cone and rod photoreceptors are transmitted to retinal ganglion cells (RGCs), which integrate the

information from photoreceptors. Amacrine and horizontal cells contribute to the processing of the visual information by modulating the signals between photoreceptors, bipolar cells and RGCs (Chalupa & Werner, 2015). Based on how RGCs respond to light stimuli, they can be classified as ON and OFF cells: ON-center cells are activated when light is increased in the center of their RF, while OFF-center cells are activated when light is decreased in the center. Surrounding the center of these RFs is an antagonistic region (OFF-center for ON cells, and ON-center for OFF cells), which creates a contrast response that enhances the detection of edges and boundaries in the visual scene. The ganglion cells' axons form the optic nerve, which transmits visual information to the lateral geniculate nucleus (LGN) of the thalamus, as well as to other structures, including the superior colliculus for orienting movements and the pretectal nucleus for pupillary reflexes. From there, the information is relayed to the primary visual cortex (Wässle, 2004), allowing the encoding of various aspects of the visual scene, including detailed color perception, motion sensitivity, and the detection of changes in the peripheral visual field. These processes enable the brain to construct a coherent representation of the external world, supporting both high-acuity tasks and broader spatial awareness (Wässle, 2004; Dowling, 2012).

1.3. Receptive Fields

The visual receptive field (RF) is the region of the visual field that, when stimulated at the retina level, by light increments and decrements, initiates the signaling cascade that will generate cortical responses. It is the area of the retinal space that allows a neuron to *see and experience* the external world (Kandel et al., 2000). Retinal RF properties are determined by the arrangement of photoreceptors, which absorb and transform light signals into electrical input for transmission through the optic nerve to the visual system (Dowling, 2012).

In the retina, RFs are organized into center-surround manner, where the center region responds oppositely to the surrounding area. The center is activated by light increments (ON-center) or decrements (OFF-center), while the surrounding area responds in the opposite manner. This ON/OFF structure encodes contrast and edge information, which is processed in the visual cortex to discern patterns, shapes, textures, and spatial information, such as object boundaries and orientation (Chalupa & Werner, 2015). As visual information progresses along the visual pathway, the complexity of RFs increases in V1, simple cells respond to basic features such as edges and their orientation, while complex cells are tuned to motion and more elaborate stimulus properties, forming the foundation for constructing complex perceptual elements. From V1, the visual information travels to V2, which is involved in processing patterns, textures and relationship between contours, and to V3, where motion and perception of dynamic stimuli are further processed. At higher levels, like MT+/V5, neurons

specialize to process depth and motion, integrating input from earlier stages of the hierarchy (DeAngelis et al., 1998).

1.4. Methods for analyzing retinotopic organization

Visual information is organized in a retinotopic manner, meaning that the spatial arrangement of retinal inputs is preserved in the brain's visual areas. Each point in the retina corresponds to a specific location in the visual cortex. The retinotopic organization is maintained throughout V1, where early processing of visual information occurs, and extends to V2, V3, and to higher-order visual areas (Wandell et al., 2007). This organization ensures that visual stimuli are processed in a manner that reflects their spatial arrangement in the external world, allowing for coherent perception.

The detailed description of the retinotopic organized visual cortices and the understanding of visual RF properties was achieved by electrophysiology techniques. Single-unit recordings are performed by inserting microelectrodes into specific cortical areas, allowing to measure the electrical activity of individual neurons *in vivo*. These recordings capture action potentials from single neurons, enabling the mapping of their responses to visual stimuli. In addition to single-unit recordings, the 2-deoxyglucose (2-DG) method has been used to study retinotopic organization. During this technique, an animal is presented with visual stimuli (e.g., a series of concentric rings or flashing light bars) while 2-DG is injected. Neurons active in response to the visual stimulus take up the 2-DG, which accumulates in the regions of the cortex corresponding to the visual

input. After the experiment, the brain tissue is analyzed, and the uptake of 2-DG is mapped to visualize the areas of the cortex that are engaged by specific visual stimuli (Tootell et al., 1988). These methods provided insights into how visual information is spatially organized and processed across different cortical layers, contributing to our understanding of visual perception (Talbot and Marshall, 1941; Daniel and Whitteridge, 1961; Hubel and Wiesel, 1974; Guld and Bertulis, 1976; Dow et al., 1981; Van Essen et al., 1984). Invasive electrophysiological recording of cortical responses has been complemented by functional MRI (fMRI), enabling non-invasive investigation of visual receptive fields through the presentation of visual stimuli during fMRI protocols. The usage of visual stimulation with rotating wedges and expanding rings, allowed Sereno and colleagues (2013) to retrieve retinotopic cortical maps of multiple visual areas (ie., V1, V3a and MT+/V5) without the need to perform invasive protocols, but only by administering an fMRI procedure. To further validate the feasibility to retrieve retinotopic map and to investigate RFs *in-vivo* and non-invasively, based on the retinotopic approach theorized by Sereno and colleagues (1994), Dumoulin and Wandell (2008) elaborated a technique that estimates aggregate neuronal receptive fields (population receptive fields pRF) within fMRI voxels by analyzing aggregate fMRI activity upon visualization of moving stimuli, such as rotating wedges and expanding/contracting rings (Dumoulin and Wandell, 2008). This technique made it possible to estimate the pRF location in the visual field by measuring RF eccentricity (i.e., distance of pRF from the fixation point) and to estimate the size of pRFs (Sereno et al., 1995; Dumoulin and Wandell, 2008). For example, Keliris and colleagues (2019) compared the electrophysiologically recorded responses of single neurons RF, from macaque's V1 with fMRI responses of the same animals to flickering checkerboards of different spatial frequencies. The authors used the spatial frequency-dependent

responses of visual RFs to estimate the average size of single unit RF (suRF): they achieved a significant match between the electrophysiological estimates and estimates from non-invasive fMRI, opening new possibilities to estimate suRF in human studies. Previous research has demonstrated the accuracy of the population receptive field (pRF) model when applied to various visual field defects, including macular degeneration (MD), Stargardt disease (STDG), Retinitis Pigmentosa (RP), rod monochromatism, glaucoma, aging, hemianopsia, and choroideremia, using standard automated perimetry tests (Baseler et al., 2011; Haak et al., 2016; Ritter et al., 2019; Pawloff et al., 2023; Ferreira et al., 2016; Baseler et al., 2005; Duncan et al., 2007; Prabhakaran et al., 2021; Brewer et al., 2014; Silva et al., 2021; Papanikolaou et al., 2014, 2019; Silson et al., 2018).

1.5. Hierarchical organization of visual cortex

The RF organization within cortical visual areas delineates a continuum of pRF size. (Fig. 2). In early visual areas as in V1, pRFs are small at the center, allowing for high-resolution processing of spatial details and precise mapping of visual inputs (Dumoulin & Wandell, 2008; Harvey & Dumoulin, 2011). By moving toward the periphery of the visual field, the size of pRFs gradually increases, reflecting a shift in the type of information processed. This gradient from center to periphery allows for both high-acuity vision in the foveal region and broader spatial awareness in the peripheral visual field. As the visual information moves to higher areas, such as V2, V3, pRFs

progressively increase in size (Wandell, Dumoulin, & Brewer, 2007). This expansion in pRF size reflects a shift from detailed local processing to the integration of information over larger regions of the visual field (Hansen et al., 2007). In the higher visual areas, neurons are able to process more complex visual stimuli, supporting advanced functions such as object recognition, motion perception, and scene analysis (Kay et al., 2013). For instance, in areas like V3 and V5/MT, larger pRFs facilitate the integration of information necessary for perceiving motion and depth, which require a broader sampling of the visual field compared to the fine detail processing in V1. The central areas, with their small pRFs, are specialized for high-acuity tasks like reading and facial recognition, while peripheral areas, with larger pRFs, are better in processing visual functions such as motion detection and the recognition of large objects or scenes. These hierarchical differences in pRF size and organization underline the functional specialization of visual cortical areas and their roles in visual perception.

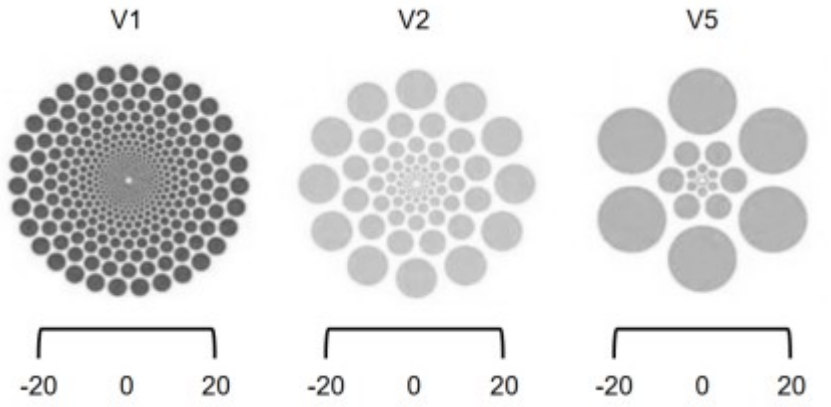

Figure 2. Population receptive field size as a function of eccentricity (±20 deg) schematically shown in V1, V3 and V5. Note, the increment is pRF size and distribution is not only present within each area, but it follows a hierarchical gradient, going from small and highly concentrated pRF in V1, to broader pRF in V5. The radius of each circle represents the pRF size at the corresponding eccentricity. Adjusted from Wandell & Winawer (2015).

The retinotopic organization of the early visual cortex ensures that neighboring cortical regions correspond to neighboring points in visual space. From early postnatal stages, the relationship between neuronal RF size and its position within cortical representation remains stable: smaller RFs are in the representation of the central retina, while larger RFs are positioned in the representation of the peripheral retina (Mazade et al., 2019). In areas V2 and V3, this retinotopic organization is maintained, but neurons in these areas integrate information from larger regions of the visual field which encompass a larger portion of visual space. This leads to progressively larger pRFs and the processing of broader spatial information compared to V1 (Hansen et al., 2007). Beyond upper and lower visual field separation, visual information follows two major visual streams: the dorsal ("where") and ventral ("what") streams, which process distinct aspects of visual input. The dorsal stream receives inputs predominantly from the lower visual field (Wandell et al., 2007). Importantly, it has been demonstrated that random dot kinematograms (RDK) stimuli located in the lower visual field lead to a stronger activation of dorsal visual stream areas compared to the ventral ones (Rossit et al., 2011). Importantly, Nau and colleagues (2018) found that dorsal areas exhibit significant BOLD responses during pursuit eye movements, integrating retinal input with eye movement. The dorsal stream extends into the parietal lobe, including areas such as V1, V2, V3, V5/MT, and the posterior parietal cortex; it specializes in motion detection, spatial awareness, and depth perception.

The ventral stream projects into the temporal lobe, encompassing areas V1, V2, V3, V4, and the inferior temporal cortex (IT). It has a principal role in fine detailed vision, important for object recognition and analysis of visual features (Goodale & Milner, 1992; Ungerleider & Mishkin, 1982). Recent studies have illustrated the practical implications of these pathways in situations where the visual input is transiently, partially occluded. For instance, during the COVID-19 pandemic, face masks, which occlude the lower half of the face, have been found to impede the ventral-stream-mediated facial recognition while leaving the dorsal-stream processing of motion and overall spatial context relatively unaffected (Critelli et al., 2021). Neuroimaging studies have shown lower neural responses in face-selective regions of the ventral stream when participants view masked versus unmasked faces, underlining the differential contributions of these pathways to visual perception and social interaction (Freud et al., 2020). Interestingly, in contrast to the description provided above, Baizer and colleagues (1991) found that inputs to the dorsal pathway predominantly arise from peripheral visual field representations, whereas inputs to the ventral stream are more associated with central visual field representations. However, it is necessary to note that these results were obtained using tracer-based methods, on macaques, that reflect anatomical connectivity rather than functional responses. Importantly, the functional measurements we adopted as in the recent fMRI studies using pRF mapping in humans, directly measure cortical activity patterns in response to visual stimulation (e.g., Wandell et al., 2007; Benson et al., 2021). These studies suggest a functional representation of central visual field input within the dorsal stream, particularly in tasks involving high-acuity and motion-related processing.

1.6. Cortical map plasticity during development

These orderly cortical maps, while stable in the size-location relationship, remain malleable throughout life and exhibit plasticity in response to changes in environment. Such plasticity in the sensory systems is particularly evident when the visual cortex is exposed to sensory deprivation or specific sensory stimulation. For instance, when the visual cortex is subjected to conditions like central retinal lesion, as seen in animal models (Thompson et al., 2017) there is a significant reorganization of the cortical maps. These manipulations force cortical neurons to adapt to a new sensory environment, resulting in changes to their molecular composition and functional properties. Himmelberg and colleagues (2023) investigated developmental plasticity in retinotopic maps of the human visual cortex. They found significant differences in how V1 samples the visual field depending on the age tested: in children, the retinotopic maps show a relatively symmetric representation between the upper and lower vertical meridians (mapped to, in order, ventral and dorsal cortices). On the contrary, in adults, a larger cortical area is devoted to the lower vertical meridian compared to the upper one (Himmelberg et al., 2023). In the animals deprived of early visual pattern information, modelling for congenital cataract, we showed that visual deprivation solely halts maturation of the cortical representation of the peripheral visual field in V1 (Laskowska-Macios et al., 2015a,b). Furthermore, when tested in adulthood, animals with early visual impairment show deficiencies in discrimination of the motion signal in high velocity or motion signal carried by dark dots presented on the bright background (Zapasnik and Burnat, 2013).

1.7. Loss of visual field - plasticity of the visual system

Studies by Gilbert and Wiesel (1992) and Kaas and colleagues (1990) investigated cortical reorganization following induced retinal lesions Gilbert and Wiesel (1992) used binocular retinal lesions in macaques and observed that V1 neurons in the lesion projection zone exhibited more peripheral RFs, located at the edges of the retinal lesion. Kaas and colleagues (1990) found neurons in the lesion zone responding to the inputs from adjacent, unaffected retinal areas. The dynamics of RFs was studied by Giannikopoulos and Eysel (2006) in a cat model of binocular retinal lesion by measuring the cortical responses in the corresponding cortical area to the lesioned retina (i.e., lesion projection zone). The authors found that responses recorded in the lesioned zone have ectopic RF at the retinal lesion border, showing a shift of the unaffected RFs (i.e., those not directly impacted by the lesion) toward the lesioned portion of the cortex. The loss of part of the visual field leads to important changes in how an individual navigates and behaves in space. Not only is there an urge to adapt to the new vision condition but also the partial perception of the visual field requires a continuous modeling of how the brain works. Plastic reorganization is inevitable during healthy development: a specific dorsal neuroplasticity response has been previously demonstrated during and after the induction of central retinal lesions in animal models of macular degeneration (MD; Burnat et al., 2017), which suggests that such neuroplastic changes can occur even in mature sensory systems. Also, this plastic reorganization has a crucial role in case of sensory deficit, such as retinal degeneration. Retinal degeneration, which involves the gradual loss of photoreceptors, disrupts the normal processing of visual information. This degeneration can lead to significant

visual impairment and demands a reorganization of the brain's visual processing pathways. In the case of diseases like photoreceptor degeneration, the retina's inability to detect light signals forces the visual system to adjust its processing strategies to compensate for the loss of sensory input, often involving neural plasticity and the reorganization of cortical representations.

Retinitis Pigmentosa (RP) is a group of inherited retinal disorders characterized by progressive degeneration of rod photoreceptors. As the disease progresses, cone cells are also affected leading to a gradual loss of vision, starting with night blindness and peripheral vision loss and experienced by the patients as tunnel vision. RP affects approximately 1/5000 individuals worldwide, with initial symptoms appearing in young adulthood (Cross et al., 2022). RP is associated with mutations in ~90 different genes (Daiger et al., 2014). Functional Magnetic Resonance Imaging (fMRI) studies have shown that RP patients with peripheral retinal degeneration exhibit reduced cortical activity in V1, V2, and V3 when presented with bright flashes and checkerboard patterns (Masuda et al., 2008, 2010; Wang et al., 2022). Even in advanced stages of photoreceptor degeneration, fMRI reveals cortical activations in totally blind RP patients (Castaldi et al., 2019).

Stargardt disease (STGD) typically manifests during childhood or adolescence, although the age of onset can vary, and is characterized by progressive central vision loss due to the degeneration of photoreceptors in the macula (i.e., the central part of the retina of about 5 mm in diameter containing the fovea, highly populated with photoreceptors). Patients often have trouble with tasks requiring fine visual acuity, such as reading or recognizing faces, while peripheral vision generally remains unaffected in the earlier stages of the disease. STDG is a hereditary retinal disorder and the most

common cause of juvenile macular degeneration (MD), affecting approximately 1 in 10,000 individuals worldwide (Cremers et al., 2020). STGD is predominantly linked to a recessive mutation in the *ABCA4* gene (Cremers et al., 2020; Ścieżyńska et al., 2016). STGD differs from macular degeneration (MD) in their causes, age of onset and progression: STGD is a hereditary condition caused by genetic mutation affecting younger individuals; on the other hand, MD is associated with aging, environmental factors, and genetic predisposition, primarily affecting individuals over 50. While STGD progresses slowly with central vision loss due to macular atrophy, MD can present as either a gradual deterioration or a rapid decline.

Studies on cortical reorganization in these patient groups have generally been limited to small sample sizes. For example, long-term studies of central and peripheral visual field loss in V1 have demonstrated task-dependent effects, with studies involving just a few participants (n=4, Masuda et al., 2008; n=3, Masuda et al., 2010). In patients with MD, where there is central photoreceptor degeneration, the pRF size has been assessed in V1, showing an increase in mean pRF size and a shift toward more peripheral locations. However, these findings were confined to the calcarine sulcus, with studies involving relatively small groups of participants (n=16 patients with MD, Baseler et al., 2011; n=8 STGD patients, Ritter et al., 2019).

2. State of art and aims

The functional relationship between retinal and cortical functional architecture is critical for understanding how visual information is processed. Particularly, the importance of the dorsal and ventral subdivisions of the early visual areas comes from evidence from animal models and human development (Burnat et al., 2017; Himmelberg et al., 2023), where the dorsal areas representing the lower visual field are likely to be prone to a more plastic state.

The ophthalmological acuity assessment is based on the stationary stimuli, processed by the central region of the retina, but leaving the role of the peripheral vision untested. Until now, cortical reorganization in patients with long-term central or peripheral vision loss has been reported in relatively small groups. Therefore, we recruited a larger cohort of patients with Retinitis Pigmentosa (RP) and patients with Stargardt Disease (STGD), ensuring robust statistical power and reliable inter-group comparisons.

Specific aims:

1. Does mechanical limiting peripheral vision in healthy controls effectively model the loss of peripheral vision as observed in RP patients?

2. If and how does long-term peripheral vision loss in RP patients and long-term central vision loss in STGD patients affect pRF size in visual cortical areas (V1-3)?

3. Does the pRF size within dorsal and ventral subdivisions of V1-3 respond similarly to the central retinal loss in STGD patients and peripheral loss in RP patients?

4. Does the motion-acuity test can detect the perceptual and functional differences in control in full vision and controls with transiently modelled loss of peripheral vision?

5. Does the measurement of acuity dependent on motion differ between RP patients and healthy controls?

3. General methods for the thesis

3.1. Participants

We tested patients with central (STGD) and peripheral (RP) photoreceptor degeneration. The initial number of recruited patients was forty-five for the RP patients (mean age = 43.83 ± 9.66), whose probands were sequenced via the RP-LCA smMIP platform (Panneman et al., 2023) and twenty-four for STGD patients (mean age = 36.67 ± 12.38), with mutations in the ABCA4 gene were included (Cremers et al., 2020). The genetic probands of all the RP patients were sequenced with the RP-LCA smMIPs platform. RP patients with tunnel vision had a central residual visual field limited to a 10-degree diameter (Humphrey field analyzer) and best-corrected visual acuity equal to or better than 20/40 (Early Treatment Diabetic Retinopathy Study [ETDRS]. Clinical examination of RP patients revealed optic disc pallor, pigmentary deposits extended throughout the retina and narrowed blood vessels. In full-field flash electroretinography (ERG; RETIscan, Roland Consult, Germany), the rod responses were severely diminished, more than the cone responses, like rod–cone dystrophy. The multifocal ERG (mfERG) was abnormal. Patients with STGD had central scotomas of 10 to 20 degrees without foveal sparing and a best-corrected visual acuity equal to or superior to 20/40. Clinical examinations revealed a “bull’s eye” appearance of the macula. In flash ERG (RETIscan, Roland Consult), the full-field rod responses were normal, and the full-field cone responses were either normal or slightly reduced. Multifocal ERG (mfERG) revealed decreased responses in the central rings, suggesting abnormal

function of the macula. Optical coherence tomography (OCT; Cirrus HD-OT Spectral Domain Technology, Zeiss, Germany) revealed a decreased thickness of the retina, most notably in the foveola. Patient clinical and genetic data are listed in Supplementary Table 1 (RP patients) and 2 (STGD patients).

Forty-six healthy participants (control group; 21 males, 25 females) aged 20–63 years (mean age = 36.67 ± 12.38) were recruited and performed as the control group. All the participants reported no history of psychiatric or neurological disorders. Written consent was obtained from all participants, ensuring that they understood the general purpose of the experiment and the potential risks associated with the MRI procedures. All procedures were performed in accordance with the relevant guidelines and regulations, and approval was obtained from the Bioethical Committee at the Medical University of Warsaw (granted to J. Szaflik: Ethical Committee, WUM (KB/65/A/2019).

3.2. Limited vision condition

To model the peripheral loss of the RP patients transiently and binocularly in the healthy participants, we temporarily blocked the peripheral visual field using swimming goggles with lenses that had been replaced (Ninghetto et al., 2024); specifically, white opaque lenses with an aperture of 1.4 mm that limited the visual field to the central 10º were used. To ensure that the goggles were suitable for every subject and to account for the natural individual interocular distance, we used a set of 14 pairs of

goggles with spacings ranging from 58 mm to 72 mm between the holes (with a step of 1 mm between each pair of goggles) to account for individual's interocular distance. Between the procedure in unrestricted vision condition and the procedure in limited vision, controls were allowed to walk around freely while wearing the goggles for a 15-minute break, and then the procedure was repeated. The RP and STGD patients underwent the procedure only once without goggles.

3.3. Functional MRI

fMRI data acquisition was performed using a 3-Tesla MRI scanner (Siemens Magnetom Trio TIM, Erlangen, Germany) with a 12-channel phased-array head coil. A structural T1-weighted image (repetition time=2530 ms, echo time=3.32 ms) was acquired for each participant. Evoked blood oxygenation level-dependent (BOLD) responses were obtained using a T2*-weighted gradient echo–planar imaging sequence with the following parameters: repetition time=2500 ms, echo time=28 ms, flip angle=80°, field of view=504 × 504, and 72 axial slices with 3 mm slice thickness and no gap between slices. Stimuli were presented on a 32" LCD rear-projection screen with a resolution of 1920 × 1080 pixels, an active area of 69.8 × 39.3 cm, and a refresh rate of 120 Hz (BOLD Screen 32, Cambridge Research Systems).

4. The pRF size analysis after loss of the visual field

4.1. Research goals and hypotheses

The first part of this project aimed at mapping receptive fields of populations of cortical neurons within fMRI voxels. With the model introduced by Dumoulin and Wandell (2008), we planned to compare the cortical reorganization triggered by juvenile central loss of photoreceptors in STGD patients, with matched onset of illness and duration to RP patients, who suffer from peripheral loss of photoreceptors. Using pRF mapping we were able to retrieve information about the size and the preferred location (defined as eccentricity, i.e., the distance of a point from the fixation point) of pRFs in these cohorts of patients. To differentiate between transient and long-term peripheral visual field loss, we covered the peripheral binocular stimulation in the control group using non-translucent goggles with central holes serving as a simulation of the peripheral photoreceptor loss in RP patients. In this study, the investigation on pRF size and preferred location was also pointing to differentiate cortical responses between dorsal and ventral subdivisions of V1, V2 and V3 to assess how the central or peripheral loss of vision would affect the cortical representation of lower and upper visual field. We hypothesized to find a different pRF reorganization based on the specific loss of the visual field and that the long-term and transient loss of visual periphery would lead to a similar pattern of results although different overall reorganization. Moreover, we

hypothesized that the plastic rearrangement of RFs in the dorsal subdivision of early visual areas V1-3 would be more emphasized than the ventral counterpart for its more plastic state.

4.2. Materials and methods

4.2.1. Order of Procedure

To rule out effects of the order of the procedure (i.e., unrestricted vision condition first, followed by transient loss of periphery) on the dynamics of the receptive fields, we tested transient loss of periphery first followed by the unrestricted vision condition in a subset of 12 of the controls. To investigate the possible effect of the procedure sequence, we performed a Student's t test on the pRF size data between transient loss before and after the 15-minute break; we did not find significant differences (t=4.875, p=1.084; before: 3.04±8.89; after: 2.97±8.80).

4.2.2. Participants

From the initial group of patients, we tested twenty-three RP patients and twenty-one STGD patients. We restricted the original size of the patient groups by applying the following exclusion criteria (see also pRF exclusion criteria in Appendix): patients were excluded if they were not able to see the stimuli on the monitor and/or did not meet the inclusion criteria for undergoing MRI (e.g., having metallic implants in their body).

For these reasons, patients 2, 15, 17, 18, 21, 22, 24 and 43 were excluded from the RP patient group, reducing the group size to thirty-seven patients. Patients 2, 13 and 15 were excluded from the STGD patient group, reducing the group size to twenty-one patients. The RP patients also had an extra exclusion criterion: their central 10 visual degrees were required to be functional. We tested this by determining which patients were not able to see the stimuli while wearing goggles and excluded the following: 1, 5, 6, 9, 12, 14, 20, 30, 31, 37, 38, 39, 40 and 45. This reduced the group size to twenty-three.

Forty-five healthy controls with normal or corrected-to-normal visual acuity aged 20–63 years (25 females; age 36.62 ± 12.52) were tested.

4.2.3. fMRI acquisition and preprocessing

We scanned four functional runs (2 for expanding rings and 2 for rotating wedges (counterclockwise rotation), acquiring ninety-seven volumes. Stimuli were generated in MATLAB (http://psychtoolbox.org/) and had a 9.2º radius, covering a total diameter of 18.4º. The stimuli performed 6 full cycles per run; the wedge subtended 45º, and the ring's aperture was 1/4 of the maximum stimulus radius.

We used the FreeSurfer image analysis suite (http://surfer.nmr.mgh.harvard.edu/) to perform cortical reconstruction and volumetric segmentation of the T1-weighted anatomical scan and preprocessed the functional images with SPM12 (https://www.fil.ion.ucl.ac.uk/spm/) to correct for distortions and motion artifacts, coregister the anatomical image to the mean functional image, segment the coregistered

structural image with the default tissue probability maps, and normalize the data to the MNI space. Finally, polar and eccentricity maps were obtained (Fig. 3A-B).

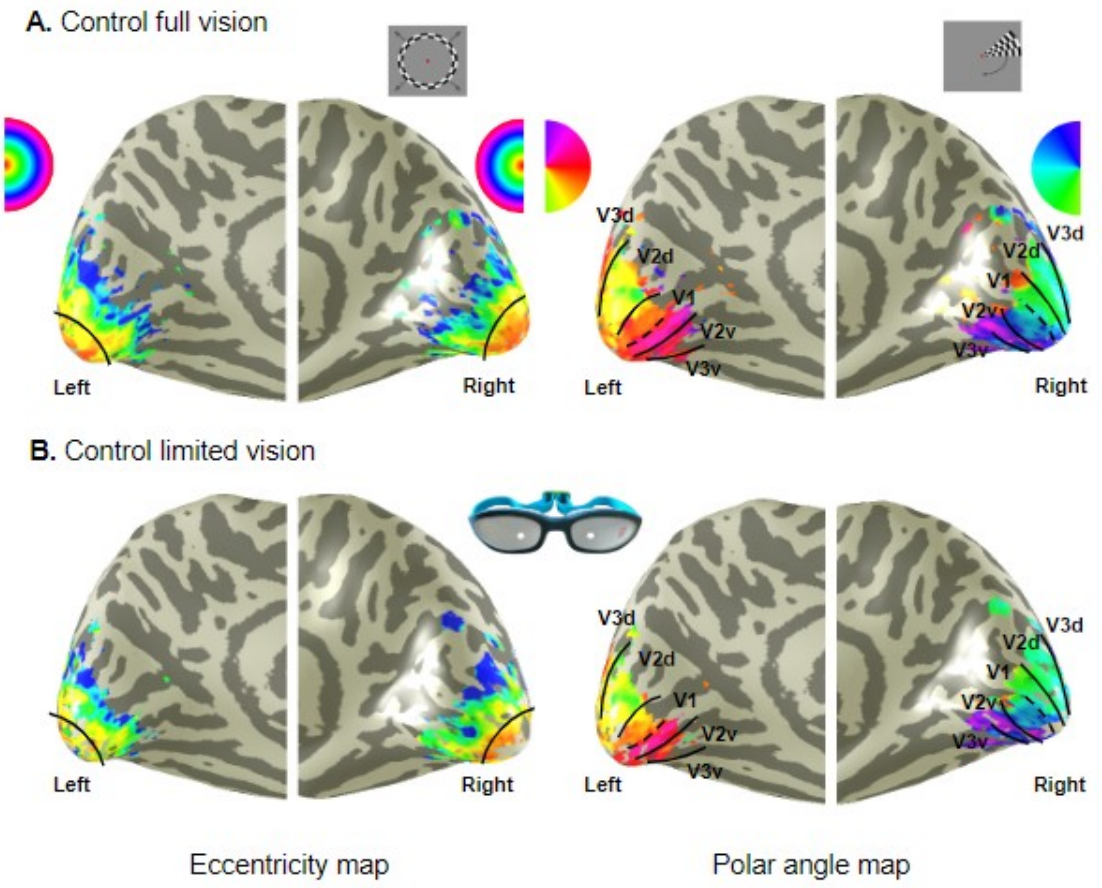

Figure. 3. Polar and eccentricity maps shown on an inflated brain of a control participant #33 with full vision **(A)** and while wearing goggles that limited their peripheral vision **(B)** Retinotopic maps of eccentricity, shown in the left panels, were obtained from the expanding ring stimulus shown at the top. The gradient from yellow to blue depicts central to peripheral eccentricity locations, as shown by the color wheel. The black line depicts a foveal representation of the visual field, colored in red. The polar maps shown at the right panels are obtained with the wedge stimulus that rotated in a counterclockwise direction shown at the top. The borders of V1, V2, and V3 are mapped by reversals in polar angle color gradients. The separation of V1 dorsal and ventral regions by the calcarine sulcus is shown with a dashed line.

We estimated pRF size and eccentricity in mrVista (Vista Lab, Stanford University) via a 2D-Gaussian pRF model and applied a threshold for including only voxels with an explained variance above 15%. For the limited vision condition, the pRF estimates outside the central 10º of the visual field were masked out from the results to remove

any additional noise from outside the goggles' aperture borders. As shown in Figure 4, where we show the inflated brains of one RP patient and one STGD patient, the activation maps are highly different and exhibit several unresponsive spots, making manual delineation of regions of interest (ROIs) inappropriate.

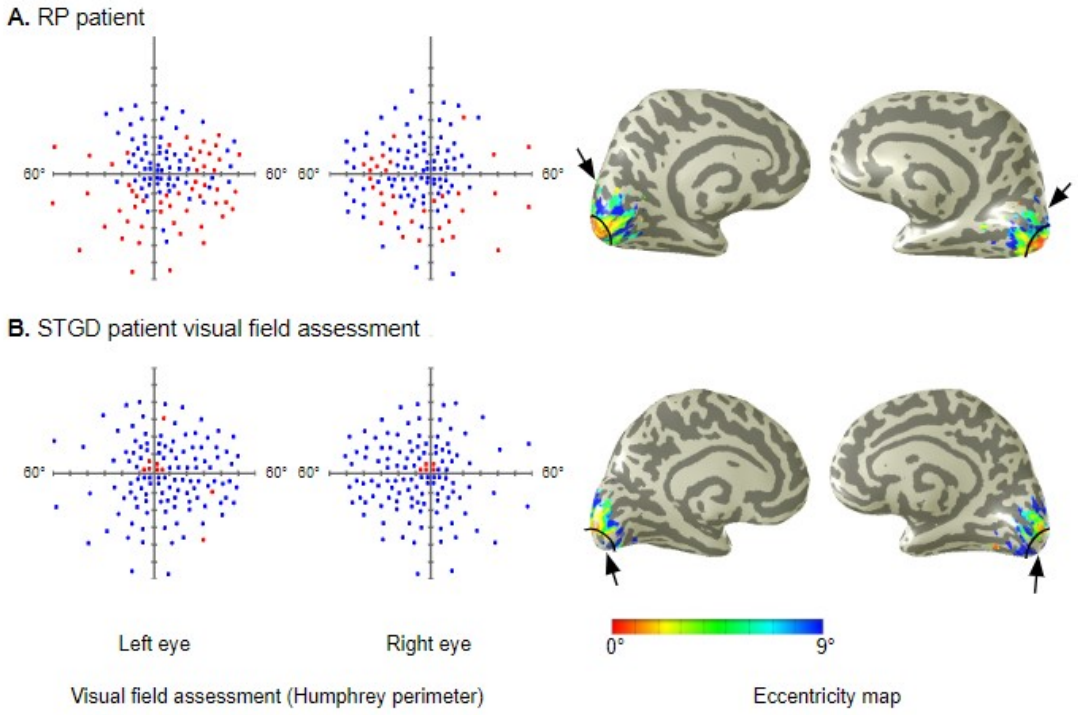

Fig. 4. Representative inflated brains overlaid with eccentricity activation maps. RP patient #1031 **(A)** and STDG patient #1395 **(B).** The Humphrey perimeter test results for the left eye and right eye and the eccentricity maps for the inflated brain. Humphrey results are shown from the full-field 120-point screening, with blue rectangles indicating stimuli that were seen and red rectangles indicating stimuli that were not seen by the participant. The black arrows point to portions of the cortical maps representing the affected part of the visual field: A) peripheral locations for the RP patient; B) the representation of the fovea for the STGD patient.

Therefore, to delineate the ROIs for the V1, V2, and V3 areas and their dorsal/ventral subdivisions, we used the atlas from Wang et al. (2015). We divided the cortical representation of the visual field of each ROI into bins: 1–3º, 3–6º and 6–9º; the 0–1º eccentricity was excluded from the analysis since it reflected the foveal representation, was prone to artifacts due to eye movements and was often difficult to activate

sufficiently. Eccentricities greater than 9 deg were also not analyzed to avoid potential pRF modeling inconsistencies close to the visible stimulus border. Although the final model returns an eccentricity for each area as a continuous variable, bins were specified artificially, and their limits do not correspond to distinct, contiguous regions in the visual cortex. We assessed the quality of the fixation of participants by using eye tracker recording as explained further in the Appendix section Fixation maps during pRF session.

4.2.4. Statistical analyses

To investigate the differences in pRF size per area, we performed three separate nested GLM analyses for comparisons: 1. controls with full vision and controls with limited vision, 2. RP patients with controls with full vision and 3. STGD patients with controls with full vision. We included the pRF size from individual voxels as outputs, and the participants were classified as a random factor, whereas groups, hemispheres and the three visual areas were classified as fixed factors. The areas were nested into the group and hemisphere.

To assess the correlation between the individual extent of the functional visual field, measured with Humphrey full-field perimetry, and the individual mean pRF size, we performed Pearson correlations between the percentage of "seen points" within the central 10º of the visual field and within a 60º radius of the visual field, between the left eye and the right pRF size in V1, V2 and V3, and between the right eye and the left pRF size for RP patients and for STGD patients separately.

To investigate the differences between the dorsal and ventral subdivisions of areas (dorsal: V1d, V2d, V3d; ventral: V1v, V2v, V3v) and eccentricity bins, we performed three nested GLM analyses for comparisons: 1. controls with full vision and controls with limited vision, 2. RP patients and controls with full vision and 3. STGD patients and controls with full vision. We included the pRF size from individual voxels; the participant identity was classified as a random factor, whereas group, hemisphere, bin, visual area and dorsal/ventral subdivision were classified as fixed factors. The bins were nested into groups: visual areas, dorsal/ventral subdivisions and hemispheres. Using the same GLM design, we investigated the shift in pRF location within the visual field using eccentricity as a dependent variable. Descriptive statistics for pRF size and eccentricity are reported in Supplementary Table 3 and Supplementary Table 4. Next, we performed four separate GLM analyses, one for each group (controls in full vision, controls in limited vision, RP patients and STDG patients), to investigate pRF size differences between dorsal and ventral V1-3 in the most central bin (i.e., 1–3 deg) for the left and right hemispheres. For these analyses, areas were nested into hemispheres and dorsal/ventral V1-3. We examined post hoc results for each analyses using a Bonferroni correction. The significance level for all the analyses was set at $p<.05$ and Statistica (1995-2020 TIBCO Software, Inc.) was used for all analyses. Under the Individual pRF responses section of the Appendix, it is possible to gain more insight on the pRF responses per person.

4.3. Results

4.3.1. The pRF size in the visual areas.

Compared with controls with full vision, controls with limited vision and RP patients with peripheral loss showed a main effect of group ($F(1,402314)=36.0$, $p<0.001$; $F(1,277439)=36.5$, $p<0.001$, respectively), hemisphere ($F(1,402314)=1033.4$, $p<0.001$; $F(1,277439)=989.7$, $p<0.001$, respectively) and area ($F=9,402314)=1202.3$, $p<0.001$; $F(9,277439)=1142.7$, $p<0.001$, respectively). Similarly, for the STGD patients, we found a main effect of group ($F(1,219139)=2071.2$, $p<0.001$), hemisphere ($F(1,277439)=989.7$, $p<0.001$) and area ($F(9,219139)=992.6$, $p<0.001$). Figure 5 shows the mean pRF size distribution in the V1, V2, and V3 for controls with full visual (blue), controls with transient peripheral loss (green) and RP patients (magenta) and STDG patients with central loss (orange). In V1, all the groups presented a significant bilateral increase in pRF size compared with that of the controls with full vision (controls with transient loss, $p<0.001$; RP patients: left $p=0.00004$, right $p=0.00002$; and STDG patients, $p<0.001$). In contrast, in V2 patients, controls with transient loss and RP patients showed a bilateral decrease in pRF size (for all comparisons, $p<0.001$), whereas in STDG patients, the pRF size remained bilaterally increased ($p<0.001$). A similar pattern was observed in V3: the unilateral pRF size decreased for controls with transient peripheral loss (left, $p<0.001$) and in RP patients (right, $p<0.001$), and the bilateral pRF size increased in STDG patients ($p<0.001$).

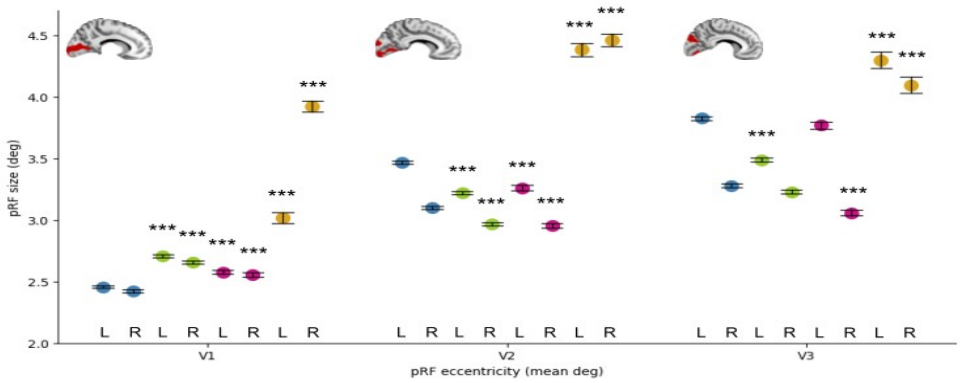

Figure 5. Mean pRF size increases for individuals with peripheral and central visual field loss in V1 but show different dynamics in V2 and V3. Mean pRF size separated for left and right hemispheres in controls in the full vision condition (blue) and in limited vision (green), RP patients (magenta) and STGD patients (orange), for V1, V2 and V3. Significant changes after peripheral and central loss, relative to control subjects with full vision (blue). Note that in V2 and V3, pRFs decrease under peripheral loss and increase under central loss. Points denote pRF mean sizes in the central 9º of the visual field, calculated as means +/- SEM, Whiskers denote the standard error. An * at the top of the points indicates significant difference of each group as compared with control group in full vision. ***p<0.00005.

The individual mean pRF size in the V1, V2, and V3 areas was not correlated with the individual extent of the patients' visual field in RP or STDG patients (Pearson correlation results shown in Supplementary Table 5). Figure 6 shows the well-established linear increase in the mean pRF size in V1, V2, V3 areas as a function of eccentricity in our model separately for the controls with full vision (Fig. 6A), controls with transient peripheral loss (Fig. 6B), STDG patients (Fig. 6C) and RP patients (Fig. 6D).

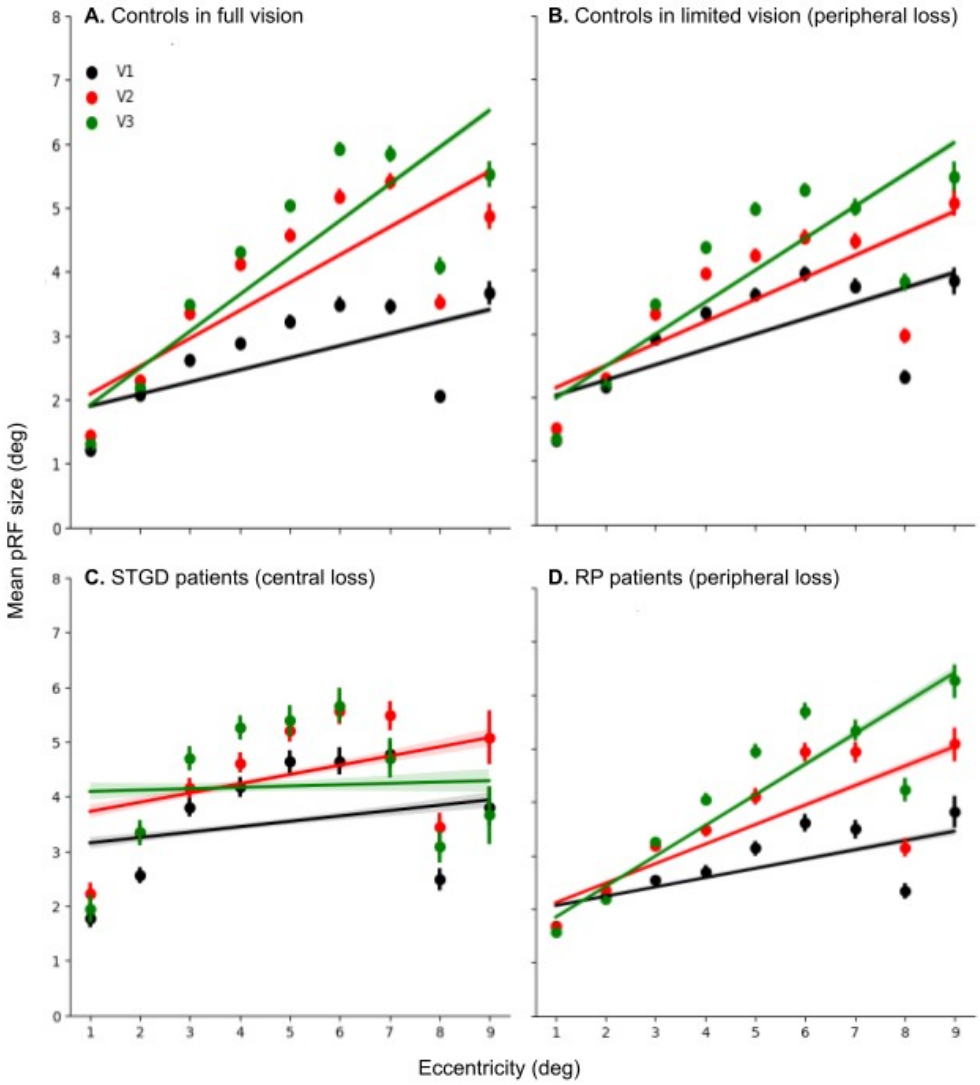

Figure 6. Mean pRF sizes in visual areas V1, V2, and V3 plotted as a function of eccentricity. (A) Controls with full vision. **(B)** Controls with limited vision. **(C)** STGD patients. **(D)** RP patients. Mean pRF size and standard error for visual areas: V1 (black), V2 (red), V3 (green). The best fit is shown for each visual area. Note that in (A-B), the V3 data are overlaid for 1–2º of eccentricity.

4.3.2. Does pRF depend on eccentricity and dorsal/ventral division?

To further explore the difference between peripheral and central loss, we performed another GLM analysis that included dorsal and ventral subdivisions and the eccentricity bins as factors. The main effects of group ($F(1,402254)=43.1$, $p<0.001$; $F(1,277379)=38.6$, $p<0.001$; $F(1,219079)=251.81$, $p<0.001$, respectively), area ($F(2,402254)=7848.8$, $p<0.001$; $F(2,277379)=5760.3$, $p<0.001$; $F(2,219079)=857.51$, $p<0.001$, respectively), hemisphere ($F(1,402254)=631.2$, $p<0.001$; $F(1,277379)=466.6$, $p<0.001$; $F(1,219079)=16.12$, $p<0.001$, respectively), and dorsal/ventral subdivisions ($F(1,402254)=735.7$, $p<0.001$; $F(1,277379)=178.1$, $p<0.001$; $F(1,219079)=792.08$, $p<0.001$, respectively) and the interaction of bins nested in vision condition, areas, hemisphere and dorsal/ventral subdivision ($F(66,402254)=1122.2$, $p<0.001$; $F(66,277379)=831.3$, $p<0.001$; $F(66,219079)=677.45$, $p<0.001$, respectively) were significant.

4.3.3. The increase in pRF size in V1

After peripheral loss in dorsal and ventral divisions, as shown in Figure 7, in the 1–3º eccentricity bin, the data from RP patients resembled that of the controls with transient loss of peripheral vision (left V1d and V1v in RP: $p=0.00058$, $p<0.001$; transient: $p=0.000002$, $p=0.0030$, respectively). Controls with transient peripheral loss showed a significant increase in the right V1v ($p<0.001$). In the 3–6º bin, controls with transient loss showed bilateral increases in the dorsal/ventral subdivisions (V1d: $p<0.001$,

p=0.0004 and V1v p<0.001, p<0.001, left/right, respectively). The RP patients showed an increase in only the right V1v (p=0.020) but a decrease in the right V1d (p<0.001). In the 6-9º bin, the ventral V1 subdivision in RP patients exhibited an increase bilaterally (p=0.00001, p<0.001), and an increase was present in the right for controls with transient peripheral loss (p=0.00004). An increase in pRF size was bilaterally present in the V1d in the transient group (p<0.001, p=0.0007), whereas in RP patients, a decrease in pRF size in the left V1d was shown (p<0.001).

After central loss in STDG patients in the dorsal division, the pRF size within the dorsal subdivision of V1 significantly increased bilaterally in bins in the 1–3º and 3–6º bins (p<0.001 for all comparisons); in the 6–9º bin, a decrease was present in the right (p<0.001). In contrast, in the V1 ventral subdivision, the 1–3º bin did not show any significant changes in pRF size. In the 3–6º bin, pRF size increased on the right (p<0.001) and in the 6–9º bin, it increased bilaterally (p=0.00005, p<0.001).

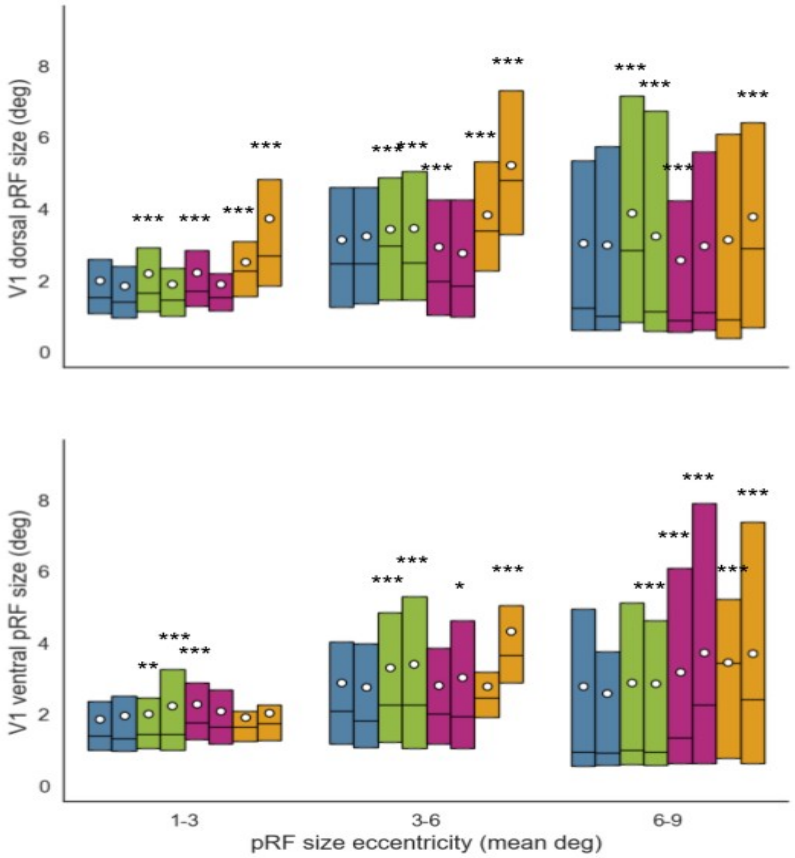

Figure 7. The mean pRF size in V1 increased after loss of the visual field. Mean data separated for left and right hemispheres in subjects with peripheral loss, i.e., transient peripheral loss in controls (green) and RP patients (magenta), and STDG patients with central loss (orange). Significant changes after peripheral and central loss, relative to control subjects with full vision (blue). Subjects with peripheral loss, i.e., transient peripheral loss in controls (green) and RP patients (magenta), and STDG patients with central loss (orange). **Top panel**: dorsal visual hemifield. **Bottom panel**: ventral visual hemifield. In each data box: the horizontal lines denote the median pRF size, the size denotes the upper and lower quartile, white point depicts the mean pRF size. Each result is shown separately for the eccentricity bins: 1–3°, 3–6° and 6–9°. The significance compared with controls in full vision is indicated by *p<0.05, **p<0.0005, ***p<0.00005.

4.3.4. pRF size in V2-3 depends on the visual field loss location.

After peripheral loss, the pRF size decreases in V2. Again, in the 1-3º bin, the data of RP patients resembled that of controls with transient loss of peripheral vision and did not show any significant changes in pRF size compared with the controls with full vision in the dorsal and ventral subdivisions of V2, except for increased pRF size in the right V2v ($p<0.001$; Fig. 8). Similarly, in the 3-6º bin, the data of RP patients resembled that of the controls with transient peripheral loss, as the pRF size decreased bilaterally in V2d ($p<0.001$). In RP patients, the pRF size also decreased in the right V2v ($p<0.001$). In the 6–9º bin, the groups with peripheral loss exhibited a bilateral decrease in V2v (transient: $p=0.00001$, $p<0.001$; RP: $p=0.0219$, $p<0.001$). In the transient group, the pRF size also bilaterally decreased in V2d ($p<0.001$).

4.3.5. After central loss in STDG, pRF in V2 increases dorsally

As in V1 in the 1-3º bin, the STDG patients exhibited the same pattern of bilateral increases in pRF size, which was specific to the dorsal subdivision of the V2 area ($p<0.001$, Fig. 8). In the 3-6º bin, an increase in pRF size was shown in the right V2d and V2v ($p<0.001$). In the 6-9º bin, the pRF size also increased bilaterally at V2d ($p<0.001$, $p=0.00012$). In V2v a bilateral decrease was found ($p<0.001$).

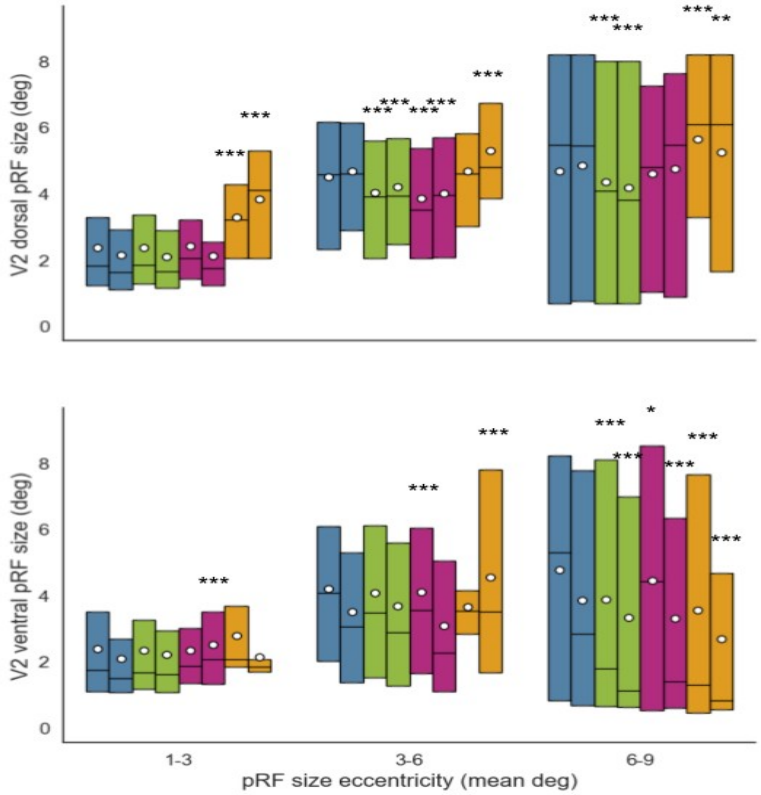

Figure 8. The V2 pRF size decreases in subjects after peripheral loss but increases after central loss. Mean data separated for left and right hemispheres in subjects with peripheral loss, i.e., transient peripheral loss in controls (green) and RP patients (magenta), and STDG patients with central loss (orange). Significant changes after peripheral and central loss, relative to control subjects with full vision (blue). **Top panel**: dorsal visual hemifield. **Bottom panel:** ventral visual hemifield. Note the increased pRF size in V2d for the STGD patients. Denotations as in Figure 7.

4.3.6. After peripheral loss, the pRF size in V3 decreased.

In the 1-3º bin, the pRF size in RP patients decreased significantly in bilateral V3v ($p=0.0218$, $p=0.0149$) and in the left V3d ($p=0.0184$, Fig. 9). This bilateral decrease in V3v in RP patients was also present in the 3–6º bin ($p=0.00002$, $p=0.00064$), whereas the controls with transient peripheral loss exhibited a decrease in pRF size in the left V3d and V3v ($p=0.0006$, $p=0.0002$, respectively). In the 6-9º bin, the transient group showed bilateral decreases in V3d and V3v ($p<0.001$), whereas RP patients showed decreases in the right V3d and V3v ($p=0.00026$, $p<0.001$).

4.3.7. pRF size in patients in the STDG

In V3 as in V1 and V2 in the 1-3º bin, the STDG patients exhibited the same pattern, with a bilateral increase in pRF size in V3d ($p<0.001$) and an increase in the right V3v ($p=0.000011$, Fig. 9). In the 3-6º bin, a pRF size increase was present in the right V3d and V3v ($p<0.001$, $p=0.00063$). In the 6-9º, the pRF size decreased in the left V3d ($p=0.00012$) and in bilateral V3v ($p<0.001$).

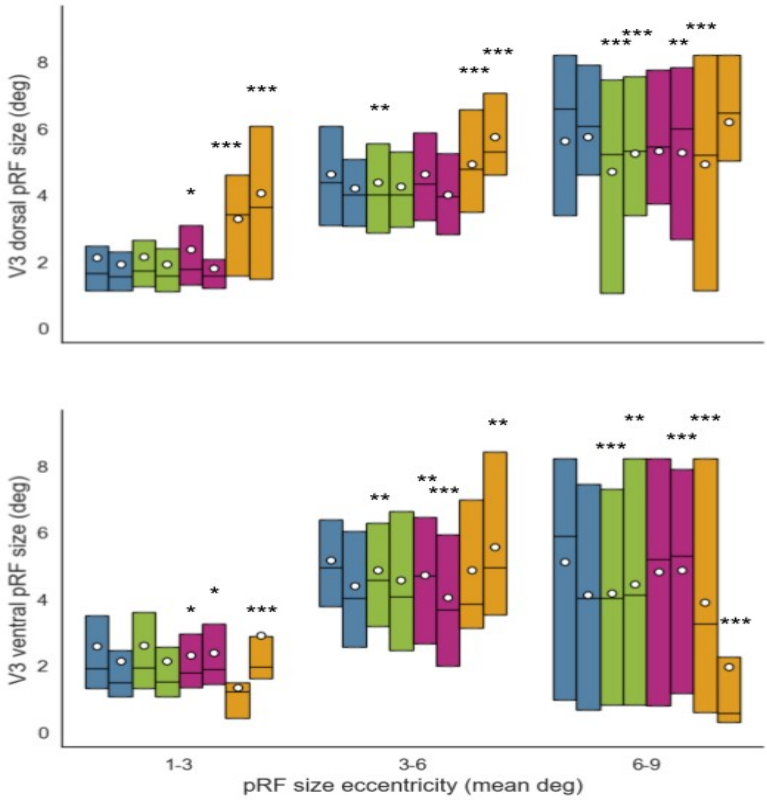

Figure 9. The V3 pRF size decreases in controls with transient peripheral loss and RP patients with long-term peripheral loss. Mean data separated for left and right hemispheres in subjects with peripheral loss, i.e., transient peripheral loss in controls (green) and RP patients (magenta), and STDG patients with central loss (orange). Significant changes after peripheral and central loss, relative to control subjects with full vision (blue). **Top panel**: dorsal visual hemifield. **Bottom panel**: ventral visual hemifield. Notably, for the STGD patients, there was a bilateral increase in pRF size within the dorsal visual hemifield, but not within ventral V3 for the 1–3° and 3–6° bins. Denotations as in Figure 7.

Interestingly, we found out that differences in pRF size between cohorts is often smaller than the difference between hemispheres within a cohort. We inserted that discussion into the Appendix section Hemispherical differences.

4.3.8. Eccentricity shift

To examine the eccentricity shift in the pRF location, we fit a separate GLM for controls with transient peripheral loss and RP patients and for STGD patients with central loss in comparison with controls with full vision. The analysis revealed a main effect of group ($F(1,402254)=60$, $p<0.001$; $F(1,277379)=21$, $p=0.00005$; $F(1,110315)=211$, $p<0.001$, respectively), area ($F(2,402254)=12$, $p=0.000006$; $F(2,277379)=21$, $p<0.001$; $F(2,110315)=3$, $p=0.03516$, respectively), dorsal/ventral subdivision ($F(1,402254)=62$, $p<0.001$; $F(1,277379)=75$, $p<0.001$; $F(1,110315)=43$, $p<0.001$, respectively) and hemisphere for only the patient groups (RP: $F(66,277379)=39669$, $p<0.001$; STGD: $F(1,110315)=17$, $p=0.00003$) and a significant interaction of the bins nested in vision condition, area, hemisphere and dorsal/ventral subdivision for controls and STGD patients ($F(66,402254)=56438$, $p<0.001$; $F(66,110315)=31181$, $p<0.001$, respectively). Therefore, we report only the significant eccentricity shifts for STDG patients. We found that pRFs shifted bilaterally toward peripheral locations in the 1-3º bin in all investigated areas: dorsal subdivisions V1d ($p=0.0001$, $p<0.001$), V2d ($p=0.04$, $p=0.000003$) and V3d ($p=0.0007$, $p<0.001$). In the 3–6º bin, the pRFs shifted toward peripheral locations in the right V1v ($p=0.0008$), bilaterally in V2d and V2v ($p<0.001$; $p<0.001$ and $p<0.001$, $p=0.031$, respectively). In the 6–9º bin, the pRFs shifted toward peripheral locations in V1d left ($p<0.001$), V1v right ($p<0.001$), V2v left ($p<0.001$) and V3v bilaterally ($p<0.001$). In V2d, only in the 6-9º bin did the pRFs shift toward a more central location bilaterally ($p<0.001$; $p=0.018$).

4.4. Discussion

Our findings revealed that the response to transient peripheral visual field loss in healthy adults was similar in the dorsal and ventral areas, with an increase in pRF size in V1 and a decrease in V2 and V3. In contrast, a recent study from Prabhakaran and colleagues (2020) reported an increase in pRF size in V2 and V3 when peripheral stimulation was limited to 4º or 7º and no change in V1. We presume that the difference in the outcome is likely due to our approach of completely removing the peripheral visual input by wearing goggles for 15 minutes prior to and during scanning. The evidence of the effects of longer and full visual input removal prior to the experimental session is supported by research in which monocular occlusion was performed for 10 minutes, and V1 reorganization and perceptual distortion were measured behaviorally (Jamal and Dilks, 2020; Dilks et al., 2009). Most likely, these observed adaptations are not long-lasting, as shown by a study in which healthy adults experienced 4 days of blurred vision (Haak et al., 2015a; Haak et al., 2015b).

We demonstrated that both controls experiencing temporary peripheral loss and RP patients with long-term peripheral loss showed a decrease in pRF size in V2 and V3. The difference in the responses between V1 and V2 and V3 might be attributed to the disruption of well-described electrophysiological feedback from higher extrastriate areas to V1 (Nurminen et al., 2018). Additionally, optogenetic inactivation of connections between V1 and V2 in the marmoset brain has been shown to result in increased RF sizes in V1 and reduced activation in V2 (Angelucci et al., 2003).

In patients with juvenile central loss (STGD), we observed an increase in pRF size in V1, V2 and V3, which is consistent with the previously described functional connectivity between these areas in MD patients (Haak et al., 2016). Previously, an increase in pRF size in V1was shown in eight MD and eight STDG patients (Baseler et al., 2011). Furthermore, studies in animal models of central loss, such as that caused by retinal lesions and induced scotomas, have also demonstrated an increase in RF size in V1 (Giannikopoulos et al., 2006; Pettet et al., 1992). We show here that this increase in pRF size predominantly occurs within the dorsal subdivision of the visual cortex, within the V1 and V2 areas and to some extent in V3. The dorsal visual cortex response to central loss in STDG patients provides functional validation of the dorsal cortical thinning in the STGD reported by our group (Sanda et al., 2018). Consistently, we previously reported specific activation of the dorsal cortex in an MD model (Burnat et al., 2017).

Here, we showed enlargement of the dorsal pRF size within the central 1–9º of eccentricity for STGD patients; this activation in the cortical representation of the central visual field likely demonstrates plastic reorganization, where central pRFs respond to peripheral stimulation (Gilbert and Li, 2012). Similarly, Baker and colleagues (2005, 2008) reported foveal V1 activation in response to peripheral stimuli in early-onset MD patients but only in patients with complete loss of vision in the central retina, similar to our STDG patient group.

We also show here that long-term peripheral loss in RP patients leads to a similar pattern of pRF size changes as that occurring after transient loss in controls: an increase in V1 and a decrease in V2 and V3. The results of Haak et al. (2012) show that such an assumption is also valid for central loss. Consistent with our results in STDG patients,

the removal of central stimulation in healthy participants resulted in an increase in pRF size and a shift toward peripheral locations in V1. Our findings show less significance for the measurements of the pRF eccentricity shift, which is generally in line with findings for V1 in eight STDG patients with peripheral eccentric pRF and more central pRFs in eight RP patients (Ritter et al., 2019).

In patients with long-term peripheral loss due to RP, we observed a general bilateral increase in pRF size in V1, a decrease in V2, and a decrease in the right V3. In the central representation of the visual field, we found that transient loss of peripheral vision altered the dorsal/ventral pRF sizes only in V1. Long-term central and long-term peripheral loss of vision resulted in an increase in pRF sizes in the right hemisphere; these changes were shown in dorsal regions of V1, V2, and V3 in STGD patients and ventral regions of V2 and V3 in RP patients. This unilateral response is consistent with the general understanding of right hemisphere dominance in attention deployment (Weintraub and Mesulam, 1987).

Visual stimulation of the lower peripheral hemifield has been described as the most powerful method for guiding attention or visual control of movements (Danckert and Goodale, 2001; He et al., 1996). Partial covering of the lower visual field impairs visually guided behaviors (Critelli et al., 2021; Weber et al., 2021). In STGD patients, the acquisition of peripheral features in dorsal RFs may reflect their role in exploring the lower visual field in everyday life, as shown here with eccentric shifts in pRF locations in V1, V2, and V3.

In V1, V2, and V3, the processing of the central upper visual field occurs in ventral cortical areas, whereas the peripheral lower visual field is processed in dorsal areas

(Wandell et al., 2007). This organization of lower and upper visual field cortical representations originates from the retina, where there is a higher density of retinal ganglion cells (~60%) in the lower quadrant of the visual field (Curcio and Allen, 1990). The projections from the superior hemiretina serve as inputs to the cortical representation of the lower visual field, resulting in the overrepresentation of the lower visual field (Schein and de Monasterio, 1987), which may explain the functional relevance of the dorsal cortical representation shown here.

In conclusion, our findings demonstrated that the response to visual field loss is dependent on dorsal-ventral cortical subdivisions and provides insights into the neural mechanisms underlying transient and long-term visual field loss, providing support for the previous finding (Burnat, 2015). We aimed to highlight the possibility of hemispheric differences in visual processing and hope to inspire future studies to test spatially directed visual field stimulation in rehabilitation procedures.

5. Behavioral and cortical assessment of motion-acuity task

5.1. Research goals and hypotheses

Considering the similar pRF responses from the pRF mapping study in the long-term and transient loss of peripheral vision, we aimed to simultaneously explore motion and shape perception at the central and peripheral vision in healthy cohorts and in RP patients using a motion-acuity task developed by us (Kozak et al., 2021; Ninghetto et al., 2024). With our novel approach we aimed to assess acuity thresholds using centrally located shapes in an active discrimination task and activating at the same time the peripheral vision with motion stimulation. The task was designed to differentiate the processing of dark and light stimuli, which reflects the natural luminance structure of most visual scenes, where details are predominantly carried by darker parts (Jin et al., 2022; Rahimi-Nasrabadi et al., 2021). So far, it is accepted that low acuity and sensitivity to the fast motion velocities clearly differentiates peripheral from central visual processing (Orban et al., 1986). The behavioral assessment of individual motion-acuity thresholds was followed by an fMRI session with the same stimuli at the individual threshold level, to check the cortical activations to a task engaging central and peripheral vision. Similarly to the first study, we modeled functions of the central and peripheral visual field in RP patients and in healthy controls with controlled peripheral stimulation of the retina by mechanically limiting the visual field with

goggles. We hypothesized that the cortical similarities between transient and long-term loss of peripheral vision obtained with the pRF mapping would be differentiated using the presented motion-acuity task, where an active engagement requires specific strategies that may emerge differently from a transient and long-term loss of part - in this case, periphery - of the visual field. We hypothesized that these strategies may depend on distinct networks of cortical activations showing patterns of plastic rearrangement based on newly adopted attentional behaviors and cortico-cortical connections.

5.2. Materials and Methods

5.2.1. Participants

As for the study one, we applied exclusion criteria, and we analyzed only data from participants who completed both behavioral and neuroimaging sessions. We tested thirty-seven RP patients After the data were collected, we matched the controls with the RP patients according to sex and age. The final analyses were conducted on 31 RP patients (13 males, 18 females; age 43.13 ± 9.75) and 31 controls (14 males, 17 females; age 41.77 ± 10.91). We initially tested also STGD patients but with some difficulties: 1) the majority of them reported to feel highly uncomfortable with the contrasts and the motion of the stimuli leading to the stop of the procedure, 2) some of the STGD patients were not able to see the centrally located target shapes making the tasks impossible to be

executed, 3) we were left with poor data for this group of patients and we were not able to perform statistical analysis due to the insufficient number of participants.

5.2.2. Motion-acuity task

Initially, thresholds were determined using stationary, solid gray shapes (Fig. 10C). Participants were tasked with identifying the circle among a surface-matched ellipse. The target stimuli (S+ and S-) were presented simultaneously in the center, within 10 degrees of the visual field. Participants were encouraged to provide immediate feedback if they were unable to perceive the shapes. Based on the position of S+ relative to the central fixation point, participants pressed either the left or right button on a response pad. Each trial began after a response was recorded or after 10 seconds if no response was given. The aspect ratio of the ellipse adjusted dynamically based on individual performance, gradually transforming from elongated to circular. Threshold estimation followed an adaptive staircase procedure, as described in earlier works (Kozak et al., 2021; Ninghetto et al., 2024). The task's complexity increased progressively until reaching the smallest perceptible difference between the shapes, defined as the acuity threshold. These thresholds, specific to stationary shape discrimination, established an individual baseline difficulty level for subsequent assessments, including motion-acuity testing and fMRI sessions (see Motion-acuity task protocol in Appendix for further insight into the task protocol). In Figure 11, these thresholds are shown as the minimal perceptible difference in visual degrees, where a smaller difference reflects better acuity. Enhanced acuity indicates that the subject can reliably discern the circle from an ellipse, even when the two shapes are nearly indistinguishable.

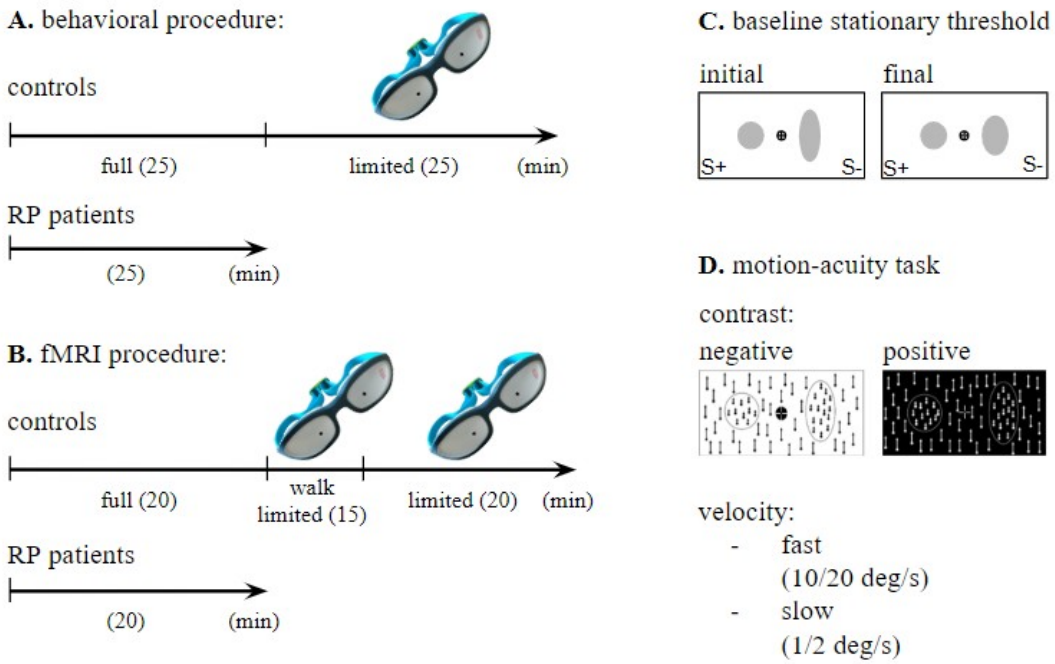

Figure 10. Procedure and motion-acuity task. (A) The behavioral assessment of motion-acuity threshold lasted 20-25 minutes with a staircase procedure for both controls and RP patients; next, the controls repeated the task wearing the narrowing goggles for 20-25 minutes. **(B)** The fMRI protocol lasted 20 minutes with constant threshold presentation of motion-acuity tasks for both groups. Afterwards, for 15 minutes before the second scanning in goggles, the controls walked freely wearing goggles, and the procedure was then repeated in limited vision. The RP patients underwent the fMRI session only once, without goggles. **(C)** Stationary stimuli used for defining the baseline threshold. Gray circle and ellipse were shown on a white background. Note the difference between the initial staircase level and the final staircase level: on the initial one, the two shapes are clearly different; the more correct responses the participants gave, the more similar the shapes became, reaching the final threshold. **(D)** The motion-acuity tasks in two contrasts, negative (black dots on a white background) and positive (white dots on a black background) at two velocities, fast (dots in shapes moving at 10 deg/s while dots on the background moving at 20 deg/s) and slow (dots in shapes moving at 1 deg/s while dots on the background moving at 2 deg/s).

A motion-acuity task was utilized (Kozak et al., 2021; Ninghetto et al., 2024), requiring participants to distinguish between a circle (S+) and a vertically oriented ellipse (S-). These stimuli involved a random dot kinematogram (RDK) segregated from the RDK background by differences in dot velocity. Both the target (S+ and S-) and the background consisted of dots moving coherently upward, with the dots in S+/- moving at a slower velocity than the background dots. The test was conducted under two velocity conditions: fast (10/20 deg/s) and slow (1/5 deg/s). Additionally, motion acuity

was assessed under two contrast conditions: positive (bright dots on a dark background) and negative (dark dots on a bright background).

During the subsequent fMRI sessions, participants completed the motion-acuity tasks at a constant level of difficulty determined by their individual baseline thresholds (Fig. 10C). Each fMRI motion-acuity task consisted of six blocks, each containing 10 trials (10 s of stimulation followed by a 20 s interstimulus interval). During stimulation, the dots moved coherently upward at either fast or slow velocities, in either positive or negative contrast. The interstimulus interval displayed a plain gray screen. Participants used a response pad to indicate the location of the circle (S+), while the ellipse length/width ratio remained fixed.

Individual motion-acuity thresholds were set for each participant based on the final results of the stationary baseline task. Consequently, the starting difficulty for the fMRI task varied between the control and RP groups, potentially resulting in different patterns of cortical activation.

5.2.3. fMRI preprocessing

Preprocessing of the imaging data was conducted using SPM12 (Wellcome Trust Centre for Neuroimaging, London, UK). The pipeline included distortion correction to address magnetic field inhomogeneities, motion correction via realignment of all functional images to the first acquired image, and coregistration of the anatomical image to the mean functional image. The structural image underwent segmentation based on default tissue probability maps and was subsequently normalized to MNI space, resampled to a voxel size of 2×2×2 mm. Movement-related artifacts were addressed by incorporating

motion regressors into the design matrix. The ART toolbox was used to detect and exclude volumes affected by excessive motion, defined by a translational threshold of 3 mm and a rotational threshold of 0.05 radians.

5.2.4. Statistical analysis

To explore differences in individual motion-acuity thresholds obtained from behavioral assessments, we conducted three separate full factorial GLM analyses comparing: (1) controls with full vision versus controls with limited vision, (2) RP patients versus controls with full vision, and (3) RP patients versus controls with limited vision. These analyses included two factors: task (4 levels: fast-negative contrast, slow-negative contrast, fast-positive contrast, slow-positive contrast) and group (control with full and limited vision, control with full vision and RP, control with limited vision and RP). Post hoc comparisons were evaluated using Bonferroni correction. Using the same GLM design, we also analyzed the percentage of correct responses during the constant motion-acuity task performed during fMRI.

To assess whole-brain cortical responses to motion-acuity tasks, we performed three independent t-tests using the SPM12 toolbox for the following comparisons: (1) controls with full vision versus controls with limited vision, (2) controls with full vision versus RP patients, and (3) controls with limited vision versus RP patients. Separate t-tests were then conducted for each motion-acuity condition (fast velocity in negative contrast, slow velocity in negative contrast, fast velocity in positive contrast, and slow velocity in positive contrast), using bidirectional t-contrasts.

For region-specific responses within the MT+/V5 motion-processing area, we utilized the MarsBaR toolbox (Bret et al., 2002) and the retinotopically-defined MT+/V5 ROI from Wang et al. (2015). Full factorial GLM analyses were performed for the same three comparisons, with factors including group (2 levels), hemisphere (2 levels), and task parameters (velocity: fast or slow; contrast: positive or negative). No significant differences in BOLD responses were observed across the groups. Statistical significance for all analyses was set at $p < 0.05$, with familywise error (FWE) correction applied to account for multiple comparisons.

Brain region identification was facilitated using the Julich Brain Atlas (Amunts et al., 2020) and the Wang et al. (2015) atlas.

5.3. Results

5.3.1. The baseline task as valid stimulus to assess individual threshold

The stationary baseline threshold (Fig. 10C) did not differ between the controls with full vision and the RP patients (Fig. 11A). For controls, the stationary baseline threshold did not differ from the final motion-acuity thresholds. In contrast, for the RP patients, the baseline threshold (mean ± standard deviation; 0.159 ± 0.09) was significantly lower than that in all tasks: under negative contrast at fast velocity ($p < 0.001$; 0.969 ± 0.47) and slow velocity ($p < 0.001$; 0.879 ± 0.53) and under positive contrast at fast velocity ($p = 0.001$; 0.600 ± 0.43) and slow velocity ($p = 0.002$; 0.582 ± 0.40).

The motion-acuity thresholds determined outside the scanner and the accuracy of the motion-acuity task performed during the fMRI procedure were analyzed using the same statistical approach. Figure 11B-C shows the significant main effects of the Bonferroni-corrected post hoc tests for separate motion-acuity tasks (Fig. 10D).

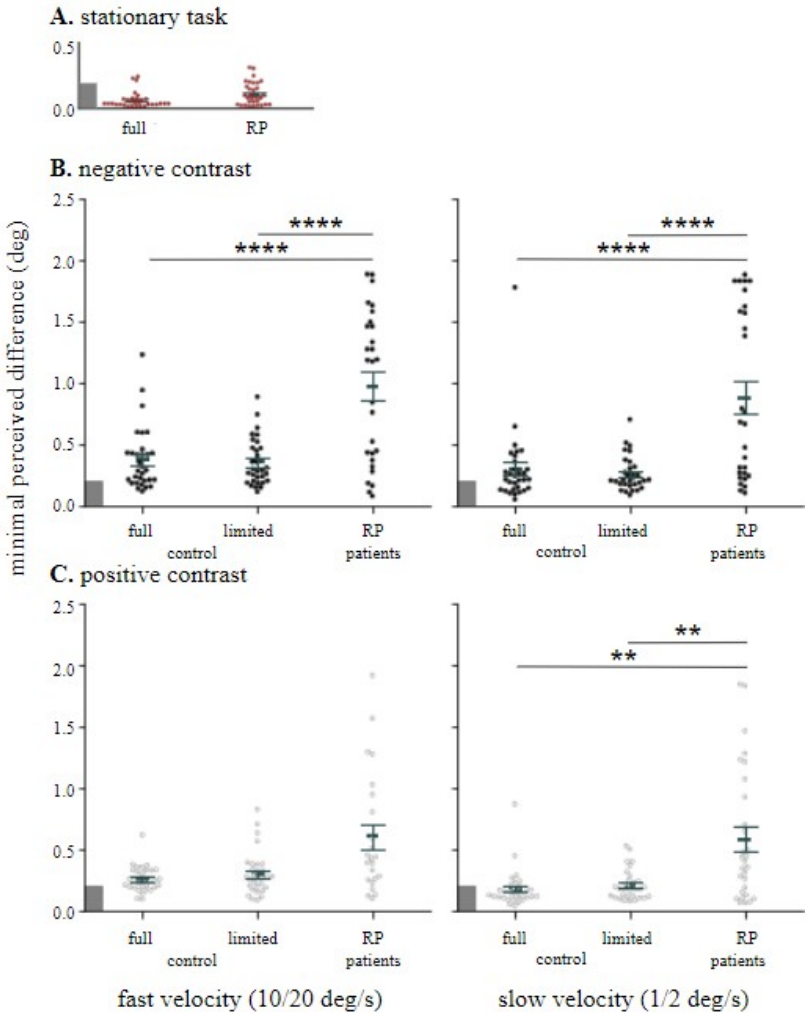

Figure 11. In the RP patients, positive contrast at slow velocity does not significantly impair motion acuity. Individual thresholds for minimal perceived differences between circle and ellipse dimensions in visual degrees for the **(A)** baseline stationary task for controls in full vision and RP patients. **(B)** negative contrast motion-acuity task. **(C)** positive contrast motion-acuity task: for the control group in full vision, in limited vision and for the RP patients. (B-C) left panels tasks in high velocity (10/20 degs), right panels tasks in slow velocity (1/2 deg/s). Note that the baseline threshold did not differ between control group and RP patients. Also, the thresholds in positive contrast tasks for the fast velocity do not differ between RP patients and controls. Circles represent the individual thresholds shown as a minimal perceived difference between circle and ellipse dimensions in visual degrees: red for stationary baseline task, black for motion-acuity task in negative contrast and white in positive contrast. The dark gray rectangles denote 0.15 degrees = 20/60, as measured by the Snellen letter chart. The significance compared with controls in full vision is indicated by **p<0.005, ****p<0.00005; means and standard errors are shown on each graph.

5.3.2. The individual motion-acuity threshold differentiated RP patients.

For the comparison between controls in full- versus limited-vision conditions, we found a main effect of the task ($F_{(3,239)} = 8.4032$, $p = 0.00002$) but not of the vision condition. Motion-acuity thresholds between tasks were significantly greater for the negative contrast at fast velocity (0.36 ± 0.22) than for the positive contrast at slow velocity (0.18 ± 0.13; $p = 0.00006$).

The comparison between controls with full vision and RP patients was significant for the task ($F_{(3,224)} = 5.8143$, $p = 0.0007$) and for the group ($F_{(1,224)} = 71.3216$, $p<0.001$). For the tasks, the motion-acuity thresholds were significantly higher for the RP patients under negative contrast (Fig. 11B) at fast velocity ($p = 0.00009$; controls 0.37 ± 0.25, RP 0.96 ± 0.61) and slow velocity ($p = 0.0001$; controls 0.30 ± 0.30, RP 0.88 ± 0.68). Motion-acuity thresholds were also significantly higher for the RP patients under positive contrast, but only for the slow velocity (Fig. 11C; $p = 0.009$, controls 0.17 ± 0.15, RP 0.58 ± 0.53).

The comparison between controls with limited vision and RP patients revealed significant differences for the task ($F_{(3,223)} = 4.7058$, $p = 0.003$) and the group ($F_{(1,223)} = 74.3877$, $p < 0.001$). Similar to the comparison between controls with full vision and RP patients the motion-acuity thresholds were significantly higher for the RP patients under negative contrast (Fig. 11B) at fast velocity ($p < 0.001$; limited 0.35 ± 0.19, RP 0.96 ± 0.61) and slow velocity ($p = 0.0001$; limited 0.25 ± 0.13, RP 0.87 ± 0.68) and under positive contrast at slow velocity (Fig. 11C; $p = 0.017$; limited 0.20 ± 0.12, RP 0.58 ± 0.53).

5.3.3. Behavior in fMRI session - decreased accuracy in RP patients.

The accuracy of the motion-acuity task performed at the constant stimulus level during the fMRI procedure, calculated as the percentage of correct responses, did not differ between controls with full and limited vision.

The comparison between controls with full vision and RP patients revealed significant differences for the task ($F_{(3,240)} = 2.918$, $p = 0.034$) and the group ($F_{(1,240)} = 111.388$, $p < 0.001$). The RP patients had a lower percentage of correct responses in all motion-acuity tasks: negative contrast at fast velocity ($p < 0.001$: controls 99.03% ± 3.96, RP 48.06% ± 46.50) and slow velocity ($p < 0.001$: controls 97.41% ± 5.14, RP 46.77% ± 43.15) and positive contrast at fast velocity ($p = 0.003$: controls 96.45% ± 6.60, RP 67.09% ± 39.42); and slow velocity ($p = 0.005$: controls 99.67% ± 1.79, RP 71.29% ± 37.39). Similarly, between the controls with limited vision and RP patients, we found significant differences for the task ($F_{(3,240)} = 3.009$, $p = 0.030$) and the group ($F_{(1,240)} = 104.905$, $p < 0.001$). The RP patients also had a lower percentage of correct responses in all motion-acuity tasks: negative contrast at fast velocity ($p < 0.001$: controls 98.06% ± 5.42; RP 48.06% ± 46.50) and slow velocity ($p < 0.001$: controls 96.12% ± 13.08; RP 46.77% ± 43.15) and positive contrast at fast velocity ($p = 0.003$: controls 96.77% ± 5.99; RP 67.09% ± 39.42) and slow velocity ($p = 0.011$: controls 98.70% ± 4.27; RP 71.29% ± 37.39).

5.3.4. Whole-brain neuroimaging results

First, analyses were computed for all tasks separately. The comparisons were performed using *t contrasts*, i.e., both directions were investigated for comparisons between 1. controls with full vision and controls with limited vision, 2. controls with full vision and RP patients and 3. controls with limited vision and RP patients. The results for the *t contrasts* for the separate motion-acuity tasks are presented in Figure 12, where A and B depict the Control full vision > RP and Control limited vision > RP t contrasts under negative contrast at fast and slow velocities, respectively. Figure 12C depicts the Control full vision > RP t contrast under positive contrast at fast and slow velocities.

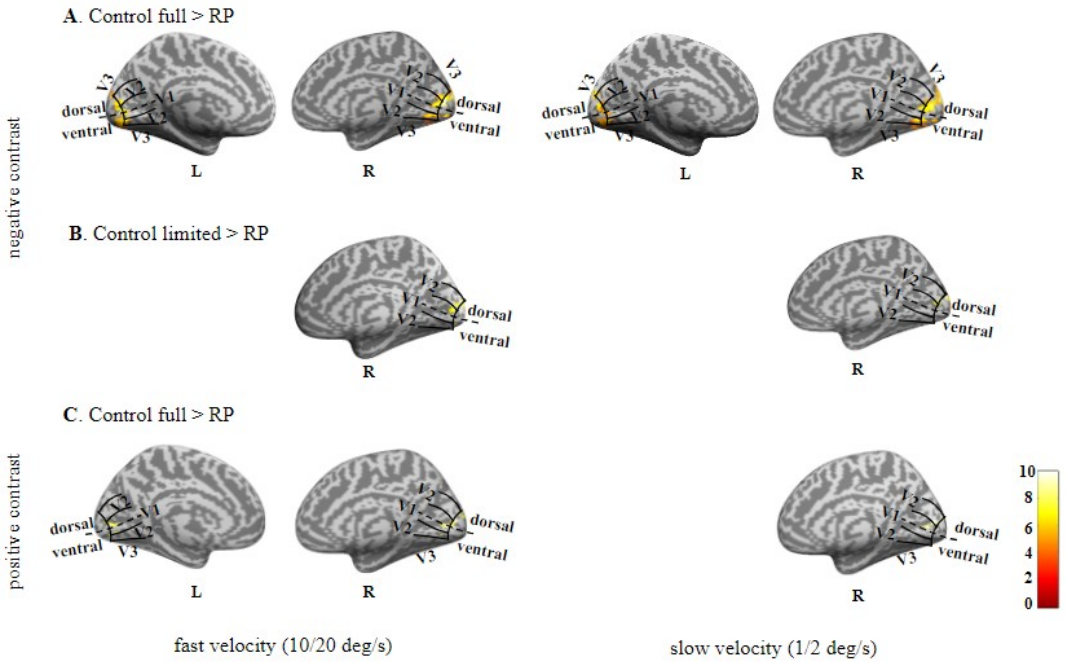

Figure 12. Reduced activations towards peripheral representation of the visual field in V1, V2, V3 areas in RP patients. The separate whole brain analysis for each motion-acuity task: Negative contrast: **(A)** Controls in full vision have stronger bilateral activations than RP patients **(B)**. Controls in limited vision have stronger activations than RP patients only in the right hemisphere. Note also the smaller extent of the activation than in A. **(C)** Positive contrast: Controls in full vision have stronger bilateral activations than RP patients. Note the biggest spatial extent of the activation in tasks in negative contrasts for comparison with controls in full vision. Left column tasks in fast velocity (10/20 deg/s) and right column tasks in slow velocity (1/2 deg/s). The dashed line depicts the position of the calcarine sulcus and divides dorsal and ventral visual areas V1-3 and black horizontal lines depict the border of the visual areas. The scale depicts the percent of BOLD change. The vertical curved line is used to visually delineate the border between the cortical representation of the central visual field in the occipital pole and the representation of the peripheral vision in the anterior portions of V1-3. The retinotopy-defined eccentricity map for controls and RP patients; thanks to these maps we might define the landmark separating central and peripheral cortical representation on the occipital pole and enter the anterior part of V1-3.

For easier interpretation of visual cortical activations, we show the cortical retinotopic map of the V1-3 areas in controls with full vision (Fig. 13A) and limited vision (Fig. 13B) and in RP patients (Fig. 13C).

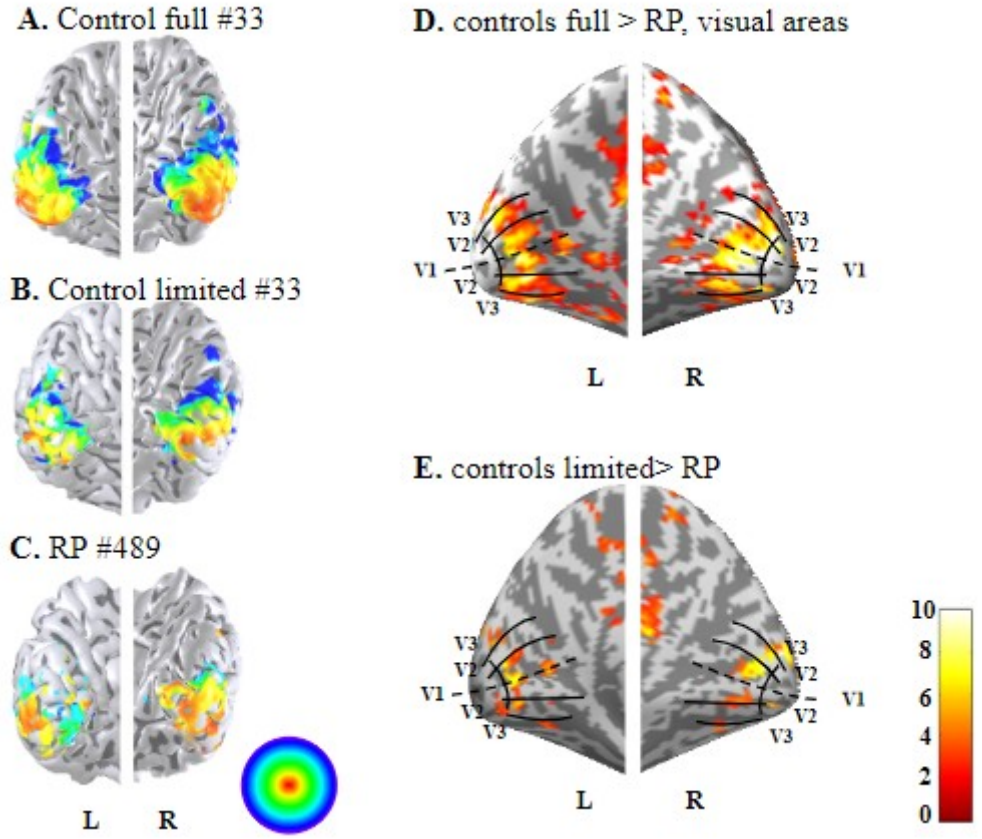

Figure 13. The difference between RP patients and the control group in full and limited vision in visual areas V1-3 as defined in the retinotopic maps. The retinotopic eccentricity map for V1-3 for a control in **(A)** full and **(B)** limited vision conditions (subject #33) and for **(C)** an RP patient (patient #489) for the left and right hemisphere. The eccentricity is color-coded from red, representing the foveal position, to blue, representing the peripheral position. Note the characteristic lack of blue color depicting the peripheral location within the visual field in RP patients, compared to the slight difference between controls in full and limited vision. Statistical maps for V1-3 visual areas for **(D)** full > RP and **(E)** limited > RP contrasts. Note how V1-3 activations differ only for the peripheral representation of the visual field, while the foveal representation (i.e., occipital pole) is not different. FWE cluster corrected at $p<0.05$. Medial and lateral views of the left (labeled as L) and right (labeled as R) hemispheres are shown. On (D) and (E) the dashed line depicts the position of the calcarine sulcus and divides dorsal and ventral visual areas V1-3, the curved vertical black line indicates the cortical representation of the central visual field which is not different between groups and black horizontal lines depict the border of the visual areas. The scale depicts the percent of BOLD change.

RP patients exhibited reduced cortical responses compared with controls with full vision, with significant differences for full vision controls > RP ($k = 139$, $p_{corr}= 0.003$); all the significant clusters are listed in Table 1.

Table 1. Local maxima for motion-acuity tasks for control full versus RP patients

				MNI coordinates		
Contrast	**Region**	**Cluster size**	**T**	**x**	**y**	**z**
Controls > RP (all tasks)	right V1	5729	10.28	12	-88	12
	right V1		9.89	10	-84	2
	left V1		9.50	-8	-80	0
	right superior frontal gyrus	139	7.68	32	56	24
	right anterior cingulate cortex		4.32	24	58	10
	left frontal operculum	992	7.46	-44	22	6
	left insular cortex		5.63	-34	30	6
	left insular cortex		5.45	-34	0	10
	left middle frontal gyrus	1424	7.07	-42	2	54
	left precentral gyrus		7.06	-36	-14	64
	left supplementary motor area		6.78	-10	18	68
	right superior frontal gyrus	532	6.43	16	26	62
	right superior frontal gyrus		5.65	16	14	62
	right middle frontal gyrus		5.40	30	28	54
	right anterior cingulate cortex	395	6.42	6	30	30
	right anterior cingulate cortex		5.40	14	28	28
	right anterior cingulate cortex		5.03	4	44	28
	left superior frontal gyrus	203	5.79	-22	52	30
	left middle frontal gyrus		4.91	-30	50	20
	left middle frontal gyrus		3.61	-28	44	12
	right superior temporal gyrus	467	5.64	66	-36	20
	right superior temporal gyrus		5.47	64	-46	20
	right superior temporal gyrus		5.13	54	-38	26
	right frontal operculum	397	5.55	54	24	14
	right insular cortex		5.40	34	12	-2
	right insular cortex		4.77	30	20	-12
	left posterior cingulate cortex	1263	5.45	-8	-44	20
	left posterior cingulate cortex		5.30	-10	-34	36
	left posterior cingulate cortex		5.07	-10	-46	40
	right precentral gyrus	398	5.43	54	2	42
	right precentral gyrus		5.06	40	0	48
	right precentral gyrus		5.02	42	0	40
	left middle temporal gyrus	148	5.33	-42	-54	14

	left middle temporal gyrus		5.11	-46	-58	8
	left middle temporal gyrus		3.76	-52	-56	2
	right precuneus	154	5.13	10	-54	58
	right precuneus		4.38	8	-54	66
	right precuneus		4.38	28	-56	44
	left middle temporal gyrus	148	4.96	-54	-12	-18
	left middle temporal gyrus		4.17	-60	-28	-8
	left middle temporal gyrus		3.85	-60	-24	-16
	left postcentral gyrus	172	4.58	-40	-34	44
	left postcentral gyrus		4.06	-36	-34	36
	left postcentral gyrus		3.94	-28	-44	42
	right supplementary motor cortex	153	4.53	4	12	52
	left supplementary motor cortex		3.99	-2	-2	58
	left supplementary motor cortex		3.81	-60	14	42

The V1-3 areas differed in the RP patients compared with the controls with full vision (Fig. 13D); however, the foveal representation in V1-3 remained unchanged. The significant clusters for full vision > RP (Fig. 14A) also included the bilateral posterior/dorsal anterior cingulate cortex (PCC and dACC) and precentral gyrus (preCG); the left mid-superior frontal gyrus (mid/supFG), MT, FO and aIC; and the right supTG.

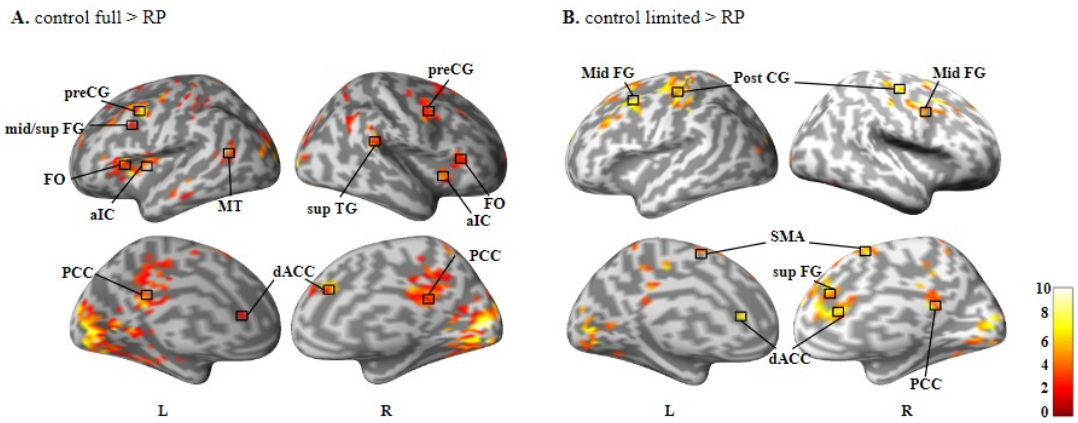

Figure 14. Whole-brain activations of RP patients show lower activations than controls in full and limited vision. (A) Statistical maps for full > RP contrast and **(B)** for limited > RP. Precentral Gyrus (preCG), middle-superior frontal gyrus (mid/supFG), Anterior Insular Cortex (aIC), Frontal Operculum (FO), Middle Temporal Gyrus (MT), Superior Temporal Gyrus (supTG), Posterior Cingulate Cortex (PCC), dorsal Anterior Cingulate Cortex (dACC), postcentral Gyrus (postCG), Supplementary Motor Area (SMA). Other denotations as in Figure 11. All significant clusters for the contrasts full > limited and full > RP are reported in Tables 1 and 2.

The t tests for separate motion-acuity tasks revealed significantly greater activations in the controls with full vision than in the RP patients for the negative contrast at fast velocity ($k = 1675$, $p_{corr} < 0.001$) and slow velocity ($k = 188$, $p_{corr} = 0.003$) and positive contrast at fast velocity ($k = 153$, $p_{corr} = 0.013$) and slow velocity ($k = 169$, $p_{corr} = 0.009$). Overall, these significantly greater activations with the controls with full vision were observed for all tasks within visual areas V1-3, outside the central visual field representation. Generally, tasks in negative contrast conditions resulted in larger clusters of activation than tasks in positive contrast conditions did (Supplementary Table 6).

The RP patients differed from the controls with limited vision in both directions, with significant differences for limited vision > RP ($k = 201$, $p_{corr} = 0.004$) and for RP > limited vision ($k = 295$, $p_{corr} = 0.001$). All the significant clusters are listed in Table 2. Similar to the comparison with controls with full vision, the peripheral parts of V1-3

differed bilaterally in RP patients; however, the cluster size for the limited vision > RP was smaller (Fig. 13E).

Table 2. Local maxima for motion-acuity tasks for control limited versus RP patients

				MNI coordinates		
Contrast	**Region**	**Cluster size**	**T**	**x**	**y**	**z**
Limited > RP (all tasks)	right V2	1374	8.16	8	-92	12
	left V1		6.45	-14	-88	4
	right V1		6.33	10	-84	4
	right superior frontal gyrus	3542	6.78	26	10	64
	right anterior cingulate cortex		6.44	4	26	18
	right superior frontal gyrus		5.97	6	52	36
	left precentral gyrus	1021	6.31	-34	-14	66
	left postcentral gyrus		5.65	-42	-26	64
	left postcentral gyrus		5.62	-46	-20	56
	left superior frontal gyrus	1009	5.80	-24	30	52
	left middle frontal gyrus		5.68	-34	4	60
	left middle frontal gyrus		5.65	-30	20	54
	left superior frontal gyrus	217	5.60	-16	26	62
	left supplementary motor area		5.20	-8	18	68
	left supplementary motor area		4.38	-18	8	58
	left V1	201	4.90	-26	-64	6
	left fusiform gyrus		4.29	-36	-64	-6
	left V1		4.23	-26	-66	-2
	lobule IV-V of vermis	252	4.55	0	-62	-12
	left lobule VI of cerebellum		4.25	-20	-68	-20
	right lobule of vermis		4.22	4	-54	-10
	right posterior cingulate gyrus	507	4.51	8	-44	18
	left middle cingulate gyrus		4.25	-12	-26	44
	left middle cingulate gyrus		4.20	-18	-40	44
RP > limited (all tasks)	left frontal operculum	330	6.19	-34	16	14
	left putamen		5.56	-26	4	10
	left putamen		5.21	-30	4	0
	right putamen	295	5.43	22	0	8

	right frontal operculum		5.12	46	12	6
	right putamen		4.98	22	8	2

Higher activations for the limited vision > RP (Fig. 16B) included bilateral clusters for the midFG, postCG, SMA and dACC and the right supFG and PCC. Separate t tests for each task (Supplementary Table 7) revealed greater activation in V1-2 for the control limited vision group only in motion acuity tasks under negative contrast at fast velocity ($k = 175$, $p_{corr} = 0.001$) and slow velocity ($k = 152$, $p_{corr} = 0.002$). These small V1-2 significant clusters outside the central visual field representation were found only in the right hemisphere (Fig. 12B).

Controls with limited vision differed from those with full vision in both directions, with significant differences for full vision > limited vision (Fig. 15A, $k = 127$, $p_{corr} = 0.003$) and limited vision > full vision (Fig. 15B, $k = 159$, $p_{corr} = 0.001$). All the significant clusters are listed in Table 3.

Table 3. Local maxima for motion-acuity tasks for control full versus control limited

				MNI coordinates		
Contrast	**Region**	**Cluster size**	**T**	**x**	**y**	**z**
Full > limited (all tasks)	left middle temporal gyrus	127	7.05	-46	-56	8
	left middle temporal gyrus		4.56	-38	-52	14
	left middle temporal gyrus		3.57	-36	-60	16
	left putamen	1394	7.05	-32	4	2
	left frontal operculum		6.52	-44	22	8
	left frontal operculum		6.38	-38	16	8
	right putamen	887	6.76	20	6	0
	right insular cortex		5.88	38	0	12

	right insular cortex		5.71	36	-2	4
	right precentral gyrus	135	5.56	52	4	18
	right frontal operculum		4.59	50	16	0
	left frontal operculum		4.32	50	10	8
	right middle occipital gyrus	161	5.41	36	-78	0
	right middle temporal gyrus		4.59	40	-70	10
	right middle temporal gyrus		4.17	48	-64	10
	left insular cortex	153	5.23	-30	-28	20
	left insular cortex		4.66	-32	-20	20
	left insular cortex		4.22	-38	-18	14
	right cuneus	234	5.03	18	-84	34
	right cuneus		4.84	26	-80	36
	right superior temporal gyrus	259	4.89	60	-12	10
	right middle temporal gyrus		4.82	50	-44	8
	right superior temporal gyrus		4.80	52	-36	20
	left hippocampus	464	4.82	-14	-26	-14
	left hippocampus		4.77	-14	-34	8
	left hippocampus		4.67	-22	-48	2
Limited > full (all tasks)	right anterior cingulate cortex	216	5.72	6	28	14
	right anterior cingulate cortex		5.13	14	38	12
	right anterior cingulate cortex		4.15	12	42	22
	right postcentral gyrus	159	4.36	50	-12	54
	right postcentral gyrus		4.27	44	-16	48
	right postcentral gyrus		3.65	42	-18	58

There were no significant differences established for the V1-3 areas. For the full vision > limited vision clusters are shown in Figure 15A, the significant clusters included the bilateral middle temporal gyrus (MT), putamen, anterior insular cortex (aIC), and frontal operculum (FO) and the right superior temporal gyrus (supTG). For the opposite comparison, limited vision > full vision, significant clusters were detected only in the right hemisphere (Fig. 15B), including the dorsal anterior cingulate cortex (dACC) and posterior central gyrus (postCG). Activations during the single tasks (fast negative

contrast, slow negative contrast, fast positive contrast, slow positive contrast) did not differ between controls with full and limited vision.

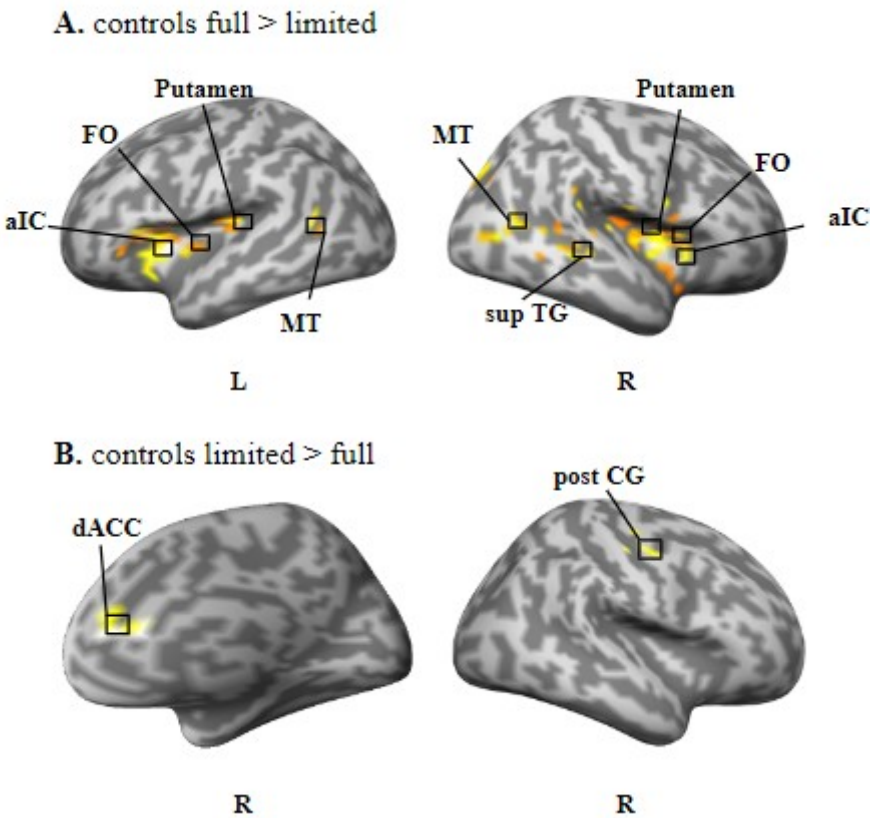

Figure 15. The difference between the control group in full and limited vision. Statistical maps show whole-brain activations for **(A)** controls: full > limited and for **(B)** controls: limited > full. Note the lack of differences in the V1-3 areas. Medial and lateral views of the left (labeled as L) and right (labeled as R) hemispheres are shown. Full > limited **(A)**: Anterior Insular Cortex (aIC), Frontal Operculum (FO), Putamen, Middle Temporal Gyrus (MT), Superior Temporal Gyrus (supTG); Limited > full **(B)**: dorsal Anterior Cingulate Cortex (dACC), Postcentral Gyrus (postCG). Other denotations as in figure 14.

Matching activations. Bilateral lower activations in the peripheral visual field representation in the V1-3 areas and in the dACC of RP patients were matched in both comparisons with controls in the full vision condition, marked in yellow, and controls in the limited vision condition, marked in pink, as shown in Figures 16 and 17.

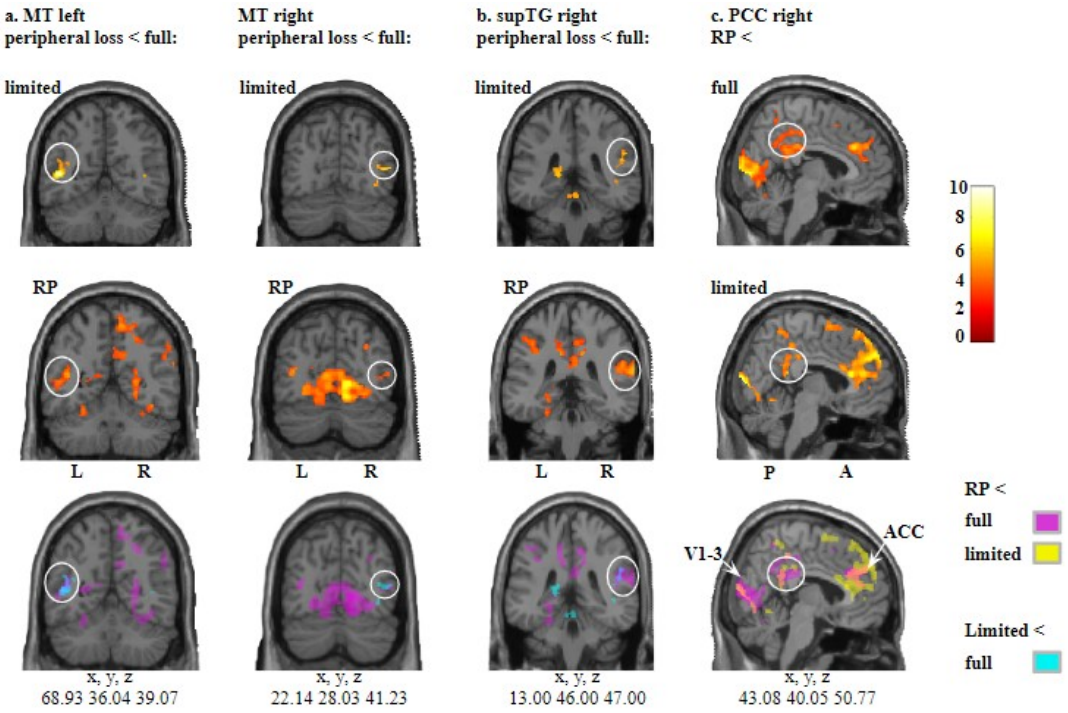

Figure 16. **Motion and spatial processing brain regions with matching activations to the loss of the peripheral visual field in RP patients and controls in limited vision. (A)** The peripheral loss in RP patients and controls in limited vision leads to similar lower activations in the medial temporal gyrus (MT) associated with motion processing and **(B)** in the right superior temporal gyrus (supTG), engaged in spatial processing. **(C)** The lower activations of the right posterior cingulate cortex (PCC) for RP compared to controls in full and limited vision. Note the overlay marked by white arrows for the right dorsal Anterior Cingulate Cortex (dACC) and for the V1-3 areas. The bottom sections show their overlays depicted by the white circles. The significant activations are marked for the contrasts: magenta for RP less than full, yellow for RP less than limited, and light blue for limited less than full.

Motion and spatial brain regions. Compared with controls with full vision, controls with limited vision and RP patients presented matched overlaid lower activations bilaterally in the motion-processing area MT (Fig. 16A, blue and pink, respectively), with a smaller cluster for the right MT in RP patients (k = 78, t-statistic = 4.35, pink; Fig. 16A) and in the spatial-processing right supTG (Fig. 16B). We found overlapping lower activation in the RP patients than in the controls in the full and limited vision conditions in the right PCC (Fig. 16C, yellow and pink).

Salience network brain regions. Surprisingly, compared with RP patients, controls with limited vision presented lower activation in the bilateral putamen (green, Fig. 17A),

which was consistent with the lower activation in the controls with full vision (larger cluster size, light blue, Fig. 17A). Matching lower activations in the RP patients than in the controls with full and limited vision were found in the bilateral dACC (Fig. 17B pink and yellow, respectively, compared with Fig. 16C). In contrast, the right dACC in controls with limited vision showed a significant increase in activation compared with that in controls with full vision and RP patients (insert in the lower row in Fig. 17B, dark blue and yellow, respectively). Matching lower activations in RP patients and in controls with limited vision than in controls with full vision were also found bilaterally in the aIC and FO (Fig. 17C, pink and blue, respectively). Compared with controls with full vision and RP patients, controls with limited vision had greater activation in the right postCG (Fig. 17D, dark blue and yellow, respectively).

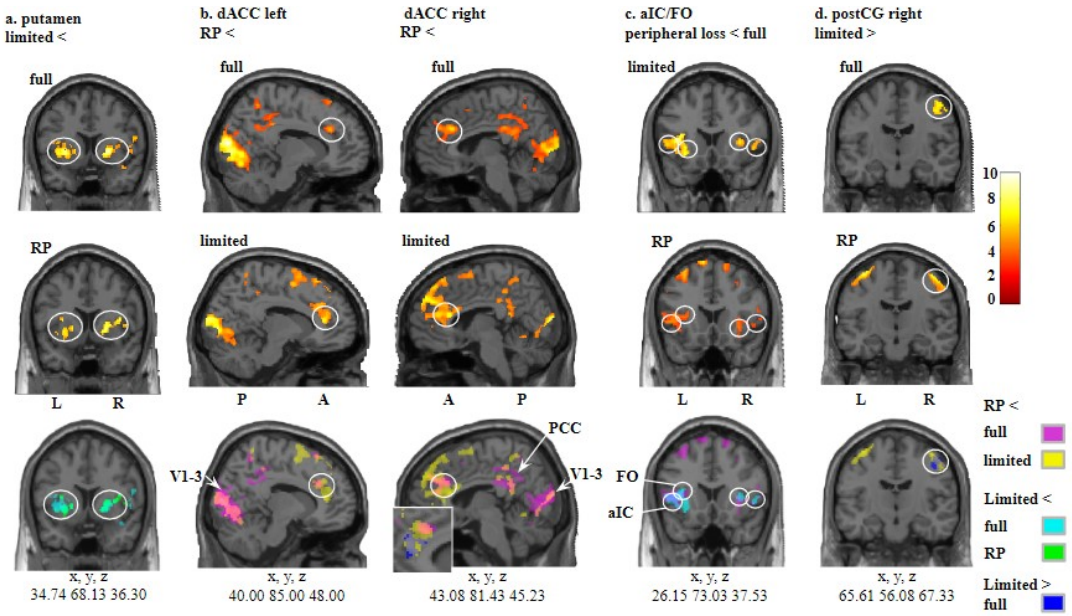

Figure 17. The salience network brain regions with matching activations in RP patients and controls in limited vision as compared to the controls in full vision. (A) The lower activations in the bilateral putamen in the controls in limited vision as compared to full vision and RP patients. **(B)** The RP patients exhibit lower activations in the left and right dorsal anterior cingulate cortex (dACC) as compared to the controls in full and limited vision. The zoomed-in rectangle insert on the bottom line for the right dACC shows the increased right dACC activation of controls in limited vision as compared to full. **(C)** The matched lower activation in bilateral anterior insular cortex (aIC) and frontal operculum (FO) in peripheral loss in controls in limited vision and RP patients. **(D)** Controls in limited vision had higher activation in the right postcentral gyrus (postCG) as compared to both controls in full vision and RP patients. Other denotations as in Figure 16.

5.4. Discussion

We aimed to investigate the impact of limited peripheral visual field input, which can result from the long-term progression of photoreceptor degeneration in RP or from a temporary restriction of peripheral vision in healthy controls. In healthy controls, the transient limitation of peripheral vision did not affect motion-acuity thresholds, but it did result in significant changes in brain activation, indicating a quick adoption of a perceptually successful strategy. Compared to controls with full vision, RP patients displayed impaired motion-acuity thresholds and different brain activation patterns, with significantly reduced responses in peripheral primary visual areas V1-3. Unexpectedly, both RP patients and controls with limited peripheral vision showed reduced activation in the bilateral motion-sensitive MT+ region when compared to controls with full vision (Tootell et al., 1995; Huk et al., 2002; Gao et al., 2020). This suppression of MT+ activation may be a result of central visual processing in both RP patients and controls with restricted peripheral vision. This interpretation is supported by previous fMRI results from RP patients using retinal prostheses to stimulate retinal ganglion cells. After the stimulation, the V1-3 areas showed an increase in BOLD signals, while MT+ did not (Castaldi et al., 2016).

In this study, we used a motion-acuity task performed under two contrast conditions, engaging both stationery and motion perception (Kozak et al., 2021; Ninghetto et al., 2024). Our results showed that the easiest task for healthy controls was the slow-velocity positive contrast motion-acuity task, regardless of whether they had full or limited peripheral vision, compared to the fast-velocity negative contrast motion-acuity

task. The processing of light and dark stimuli is segregated at the retina and is also maintained at the cortical level, where processing of dark stimuli typically dominates over light stimuli. These assumptions are supported by research on stationary stimuli and the representation of the central visual field within V1 (Jansen et al., 2019; Jimenez et al., 2018; Yeh et al., 2009; Zemon et al., 1988). However, less is known about contrast-dependent motion stimulation. Behavioral results from previous studies indicated the best accuracy was achieved for positive contrast slow-velocity bar detection (Luo-Li et al., 2018). The impaired processing of negative contrast motion in RP patients aligns with their retinal dysfunction. RP patients suffer from a dysregulation of both the central and peripheral retina due to photoreceptor degeneration, which affects the peripheral retina dominated by rod photoreceptors sensitive to contrast changes (Boyd and Tubert, 2023; Kolb, 2001) as well as the rods in the central retina (Sahel et al., 2014). Additionally, RP patients experience night blindness and deficits in dark adaptation (Herse, 2005). These factors contributed to the higher thresholds observed for negative contrast motion-acuity tasks in RP patients. The impact of peripheral stimulation on acuity in RP patients has also been demonstrated in tasks like high-contrast black letter discrimination (Oishi et al., 2012).

RP patients show reduced activation in the cortical representation of the peripheral visual field in V1-3, a finding also observed by Ferreira and colleagues (2016). The fast-velocity negative contrast motion-acuity task was particularly challenging for RP patients, likely reflecting the loss of peripheral vision. Sensitivity to fast velocity is a characteristic feature that differentiates peripheral from central visual processing (Orban et al., 1986). RP patients also exhibit impairments in exploratory motor behavior and saccadic movements (Gameiro et al., 2018; Guadron et al., 2023), which is reflected

in lower activation in the precentral gyrus (preCG) compared to controls with full vision. Healthy participants with more efficient antisaccade behavior tend to show higher preCG gray matter volume (Jin et al., 2022). Interestingly, RP patients and controls with full vision showed greater activation in the bilateral putamen than controls with limited vision. The basal ganglia, including the putamen, are involved in both motor and oculomotor functions (Lanciego et al., 2012; Rektor et al., 2001), and the increased activation in RP patients likely reflects the need for greater engagement to achieve sufficient exploratory control. A previous study in macaques showed that the putamen and dorsal anterior cingulate cortex (dACC) work together during learning behaviors in a visual task, with the dACC being activated initially and the putamen becoming involved after a series of successful trials (Cohen et al., 2021). In our study, we observed higher activation in the dACC and lower activation in the putamen in controls with limited vision compared to those with full vision, possibly reflecting the adjustment to new strategies and a lack of confidence in solving the task during peripheral vision loss. RP patients, in contrast, showed lower activation in the bilateral dACC compared to both controls with full and limited vision, which could indicate their adjustment to the cognitively demanding environment caused by progressive vision loss. The dACC is also activated in high-conflict tasks like the Stroop test (David et al., 2005) and tasks involving cognitive interference, such as identifying a target digit among a set of numbers (Sheth et al., 2013). The reduced activation in the dACC during demanding motion-acuity tasks in RP patients might resemble the decreased activity observed in procrastinating individuals under pressure, compared to the increase seen in low-procrastinating subjects (Wypych et al., 2019).

Furthermore, we found increased activation of the dACC and postcentral gyrus (postCG) in the right hemisphere in controls with limited vision, which could be associated with a general mobilization of the right hemisphere's attention network in response to a challenging visual task (Weintraub and Mesulam, 1987). We also observed greater cortical responses in the right V1-3 areas in controls compared to RP patients. In both RP patients and controls with limited vision, we found decreased activation in the right superior temporal gyrus (supTG) compared to controls with full vision. Lesions in the right supTG are known to affect spatial processing and awareness, as seen in patients with hemispatial neglect (Karnath et al., 2001; Gharabaghi et al., 2006), and transcranial magnetic stimulation of this area impairs spatial processing (Shah-Basak et al., 2018). The reduced activation in the right supTG in RP patients and controls with limited vision likely reflects impaired spatial processing due to the restricted visual field.

A similar pattern of decreased activation due to peripheral vision loss was observed in the frontal operculum (FO) and anterior insula cortex (aIC), regions involved in goal-directed tasks. Both the aIC and dACC play key roles in processing salient stimuli and are connected to limbic structures involved in reward and motivation (Menon and Uddin, 2010; Seeley et al., 2007; Uddin, 2015). The FO is thought to be involved in goal-directed tasks that overlap across modalities (Dosenbach et al., 2006; Quirmbach and Limanowski, 2022).

Introducing rehabilitation procedures for RP patients is challenging, as they typically become aware of their blind spots only in the later stages of the disease (Hamel, 2006). Current rehabilitation efforts have targeted unaffected areas of the retina, such as through diode micropulse laser treatment applied to the foveal region (Luttrull, 2018).

The V1 cortical representation of the peripheral retina is a key target for rehabilitation in blindness (Eckert et al., 2008; Striem-Amit et al., 2015; Sabbah et al., 2016). In RP patients, this multimodal response can hinder peripheral visual functions, so strengthening the healthy adaptive strategies seen in controls with limited vision may help halt maladaptive responses, leading to better functional compensation for visual impairments.

This part of the thesis covering the original study two, has been already published as an original article in the Scientific Reports journal (Ninghetto et al., 2024).

6. Summary and Conclusions

In this thesis, the neural and behavioral consequences of peripheral and central visual field loss have been investigated, exploring both transient and long-term conditions. Through two complementary studies, we aimed to understand how the visual system adapts to visual field restrictions in healthy individuals and patients with progressive retinal degenerative diseases such as retinitis pigmentosa (RP) and Stargardt disease (STGD).

Interestingly, central loss in STGD patients produced distinct responses, with pRF size increases predominantly in dorsal regions of V1, V2, and V3, as depicted in the figure 18.

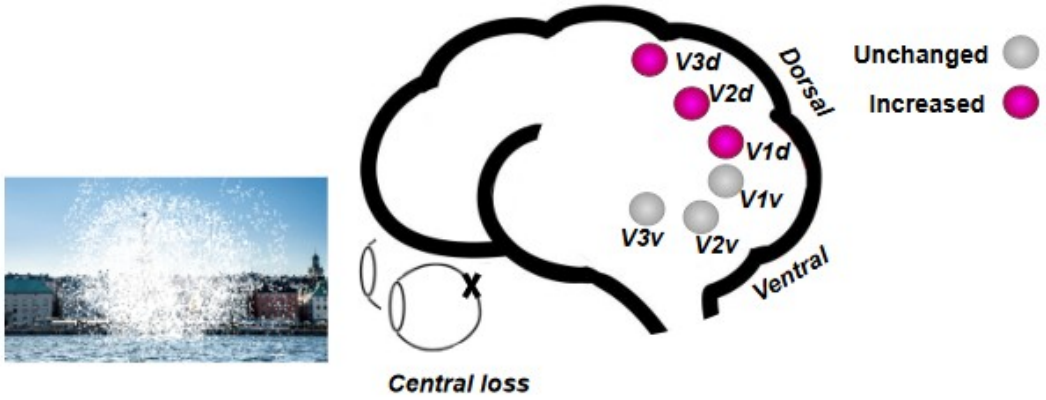

Figure 18. Summary of obtained results in STDG participants with central loss. Schematic representation of increased pRF size in dorsal V1-3 and decreased in ventral V1-3 in STGD patients with central vision loss. In a schematic view of the brain, results are summarized as a striking dissociation between dorsal and ventral subdivisions of V1-3. Showing increased pRF size in all dorsal ROIs and decreased in the ventral ones, as compared to the control group in full vision. The "X" on the edges of the eye denotes the affected foveal location. The picture on the left represents, with a white foggy effect, the loss of central vision. Gray denotes unchanged pRF size, magenta increased pRF size.

This finding provides functional validation of cortical thinning in the dorsal stream previously reported (Sanda et al., 2018), supporting the hypothesis that dorsal stream adaptations may compensate for lost central vision. Such dorsal preference is consistent with its role in spatial attention and motion processing, particularly for lower visual field representations critical for everyday navigation (Danckert and Goodale, 2001; Critelli et al., 2021).

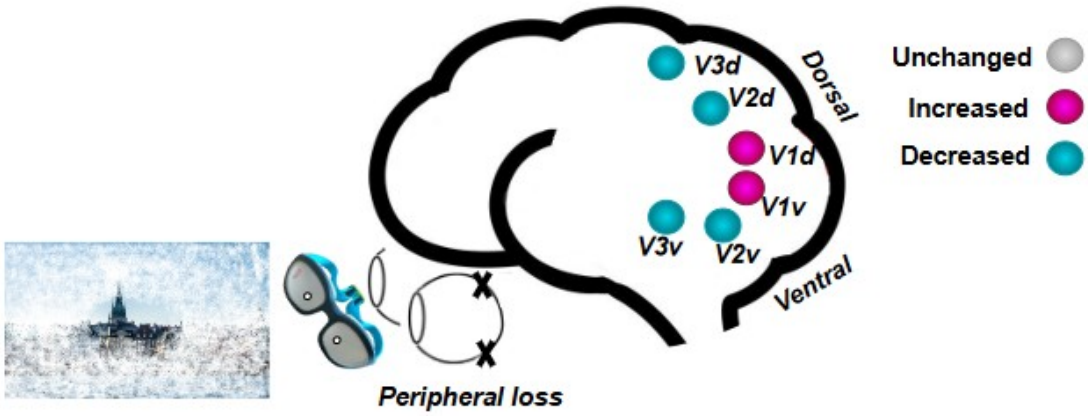

Figure 19. Summary of obtained similar results in participants with peripheral loss. RP patients and controls with transient limited vision by goggles. In a schematic view of the brain, results are summarized as increased pRF size in V1 and decreased in V2-3, as compared to the control group in full vision. Gray denotes unchanged pRF size, blue decreased pRF size, magenta increased pRF size. The "X" displayed on the edges of the eye denotes the affected retinal representation by the disease (RP patients) and by the narrowing goggles (controls). The picture on the left simulates the limited vision, using a white fog effect to represent the loss of the peripheral visual field. Note, since it is a schematic representation, the size and the location of the circles are not the real representations of pRF size and location or ROIs.

Transient peripheral loss in healthy individuals induced adaptations in pRF sizes within the 15-minute of wearing the goggles, with an increase in V1 and a decrease in V2 and V3 (Figure 19). With these findings, we want to stress the importance of short-term visual deprivation in altering cortical representations, consistent with studies showing rapid functional reorganization under transient occlusion (Jamal and Dilks, 2020; Haak et al., 2015). Long-term loss in RP patients revealed a similar pattern of pRF changes, highlighting that even chronic degeneration partially follows patterns observed in short-term adaptations. One of the central results emerging from this work is the different significant role of visual cortex plasticity in response to varying patterns of visual field loss depending on loss location as shown on Figures 18 and 19. These results align with evidence that neural networks in early visual areas retain a surprising degree of flexibility despite long-term degeneration (Baseler et al., 2011; Gilbert and Li, 2012).

The second study extended these findings to motion perception, revealing deficits in RP patients' motion-acuity thresholds, particularly for negative contrast and fast-motion stimuli. These impairments align with known rod photoreceptor degeneration, which disproportionately affects peripheral retinal regions responsible for high-velocity processing (Kolb, 2001). Moreover, RP patients exhibited lower activation in the motion-sensitive MT+ region and attenuated engagement of the dorsal anterior cingulate cortex (dACC) compared with controls. This reduced dACC activation may reflect chronic cognitive overload from adapting to progressive vision loss, contrasting with the heightened dACC activity observed during transient peripheral restriction in controls (Cohen et al., 2021; Wypych et al., 2019). Such differences in cortical engagement highlight the interplay between acute strategies and long-term compensatory mechanisms.

With the results I reported here, we were able to identify that the loss of central vision in STGD patients likely brings back the dorsal cortical representation of the lower visual field to an early developmental stage, when the dorsal areas were prone to more plastic rearrangements (Burnat et al., 2017; Himmelberg et al., 2023). Our data on pRF plasticity could provide a new insight in the development of more targeted interventions that take into consideration the distinct role discovered here of dorsal and ventral V1-V3 subdivisions in long-term loss of central and peripheral vision. However, as patients, particularly, RP patients often lack awareness of their visual deficits until late stages (Hamel, 2006), early detection and intervention remain critical challenges.

A notable implication of these findings is the potential to adopt observed strategies in controls for rehabilitation interventions in patients. For instance, enhancing dorsal stream activation and central-peripheral interactions could be explored as part of visual

training programs, drawing on successful strategies observed in transient deprivation models. Recent advances in neuroplasticity-based interventions, including visual field training and neuromodulation, could provide a foundation for targeted therapies (Sabbah et al., 2016; Striem-Amit et al., 2015). Moreover, advances in vision restoration approaches have been outlined and reviewed by Roska and Sahel (rev, 2018) as three main branches: gene therapy, optogenetic, cell therapy. Yet, as reported by Roska and Sahel, these techniques are not free of difficulties that make hard to define a definitive approach; they highlighted five key challenges: 1) in human there is an intrinsic regeneration limitation that, unlike some species such as fish, impede the natural repair process to slow down the disease progression, 2) the retina comprises approximately 100 distinct cell types with specific and diverse connections, making a challenge finding a cell-type-specific treatment, 3) commonly used invasive mouse models are not fully representative of human retinal conditions, 4) the inner membrane of the primate retina restricts the diffusion of gene therapy vectors especially in the peripheral retina, limiting the efficacy of intravitreal delivery methods, 5) differently from other species, the human retina has a vast surface area, which makes complex delivery of therapies across its entirety (Roska and Sahel, 2018).

The motion-acuity-test advances the capability of standard tests to reveal spare or even strengthened vision functions, that until now remained undetected, in patients with injured visual system. This research contributes to a broader understanding of visual system plasticity and its implications for visual disorders such as MD and RP, ultimately aiding in the development of more targeted therapeutic interventions. However, the differences in hemispheric involvement between transient and long-term conditions, with greater right-hemisphere activation observed in controls with limited

vision, underscore the need to examine hemispheric asymmetries in visual adaptation further (Weintraub and Mesulam, 1987).

In conclusion, this thesis highlights the adaptability of the visual system to peripheral and central visual field loss, demonstrating condition-specific mechanisms of cortical reorganization and similar patterns shared by long term and transient loss of visual field. By showing the neural correlates of short- and long-term visual deprivation, our findings lead the way for future studies aimed at refining rehabilitation techniques. These insights contribute to the broader understanding of sensory plasticity and its application in mitigating the functional consequences of visual impairments. Further exploration into hemispheric dynamics, dorsal-ventral stream interactions, and individual variability in plasticity responses could yield valuable directions for advancing both basic science and clinical practice.

7. References

1. Alexander, G. E., Crutcher, M. D., & DeLong, M. R. (1990). Basal ganglia-thalamocortical circuits: parallel substrates for motor, oculomotor, "prefrontal" and "limbic" functions. *Progress in Brain Research*, *85*, 119–146.
2. Amunts, K., Mohlberg, H., Bludau, S., & Zilles, K. (2020). Julich-Brain: A 3D probabilistic atlas of the human brain's cytoarchitecture. *Science*, *369*(6506), 988–992.
3. Angelucci, A., & Bullier, J. (2003). Reaching beyond the classical receptive field of V1 neurons: horizontal or feedback axons? *Journal of Physiology, 97*(2-3), 141–154.
4. Baizer, J. S., Ungerleider, L. G., & Desimone, R. (1991). Organization of visual inputs to the inferior temporal and posterior parietal cortex in macaques. *The Journal of Neuroscience, 11*(1), 168–190
5. Baker, C. I., Dilks, D. D., Peli, E., & Kanwisher, N. (2008). Reorganization of visual processing in macular degeneration: replication and clues about the role of foveal loss. *Vision Research*, *48*(18), 1910–1919.
6. Baker, C. I., Peli, E., Knouf, N., & Kanwisher, N. G. (2005). Reorganization of visual processing in macular degeneration. *Journal of Neuroscience*, *25*(3), 614–618.
7. Baseler, H. A., Brewer, A. A., Sharpe, L. T., Morland, A. B., Jägle, H., & Wandell, B. A. (2002). Reorganization of human cortical maps caused by inherited photoreceptor abnormalities. *Nature Neuroscience*, *5*(4), 364–370.
8. Baseler, H. A., Gouws, A., Haak, K. V., Racey, C., Crossland, M. D., Tufail, A., Rubin, G. S., Cornelissen, F. W., & Morland, A. B. (2011). Large-scale remapping of visual cortex is absent in adult humans with macular degeneration. *Nature Neuroscience*, *14*(5), 649–655.
9. Benson, N. C., Kupers, E. R., Barbot, A., Carrasco, M., & Winawer, J. (2021). Cortical magnification in human visual cortex parallels task performance around the visual field. *eLife, 10*, e67685.
10. Boyd, K., & Turbert, D. (2023). Eye Anatomy: Parts of the Eye and How We See. https://www.aao.org/eye-health/anatomy/parts-of-eye
11. Brett, M., Anton, J. L., Valabregue, R., & Poline, J. B. (2002, June). Region of interest analysis using an SPM toolbox. [abstract] *8th International Conference on Functional Mapping of the Human Brain, 16* (2), 497.
12. Brewer, A. A., & Barton, B. (2014). Visual cortex in aging and Alzheimer's disease: changes in visual field maps and population receptive fields. *Frontiers in Psychology*, *5*, 74.
13. Burnat, K., Hu, T. T., Kossut, M., Eysel, U. T., & Arckens, L. (2017). Plasticity Beyond V1: Reinforcement of Motion Perception upon

Binocular Central Retinal Lesions in Adulthood. *Journal of Neuroscience, 37*(37), 8989–8999.

14. Burnat K. (2015). Are visual peripheries forever young? *Neural Plasticity*, *2015*, 307929.

15. Castaldi, E., Cicchini, G. M., Cinelli, L., Biagi, L., Rizzo, S., & Morrone, M. C. (2016). Visual BOLD Response in Late Blind Subjects with Argus II Retinal Prosthesis. *PLoS Biology*, *14*(10), e1002569.

16. Castaldi, E., Cicchini, G. M., Falsini, B., Binda, P., & Morrone, M. C. (2019). Residual Visual Responses in Patients With Retinitis Pigmentosa Revealed by Functional Magnetic Resonance Imaging. *Translational Vision Science & Technology*, *8*(6), 44.

17. Cohen, Y., Schneidman, E., & Paz, R. (2021). The geometry of neuronal representations during rule learning reveals complementary roles of cingulate cortex and putamen. *Neuron*, *109*(5), 839–851.e9.

18. Cremers, F. P. M., Lee, W., Collin, R. W. J., & Allikmets, R. (2020). Clinical spectrum, genetic complexity and therapeutic approaches for retinal disease caused by ABCA4 mutations. *Progress in Retinal and Eye Research*, *79*, 100861.

19. Critelli, K., Demiris, V., Klatt, B. N., Crane, B., & Anson, E. R. (2021). Facemasks Block Lower Visual Field in Youth Ice Hockey. *Frontiers in Sports and Active Living*, *3*, 787182.

20. Cross, N., van Steen, C., Zegaoui, Y., Satherley, A., & Angelillo, L. (2022). Retinitis Pigmentosa: Burden of Disease and Current Unmet Needs. *Clinical Ophthalmology*, *16*, 1993–2010.

21. Curcio, C. A., & Allen, K. A. (1990). Topography of ganglion cells in human retina. *Journal of Comparative Neurology*, *300*(1), 5–25.

22. Daiger, S. P., Sullivan, L. S., & Bowne, S. J. (2013). Genes and mutations causing retinitis pigmentosa. *Clinical Genetics*, *84*(2), 132–141.

23. Danckert, J., & Goodale, M. A. (2001). Superior performance for visually guided pointing in the lower visual field. *Experimental Brain Research*, *137*(3-4), 303–308.

24. Davis, K. D., Taylor, K. S., Hutchison, W. D., Dostrovsky, J. O., McAndrews, M. P., Richter, E. O., & Lozano, A. M. (2005). Human anterior cingulate cortex neurons encode cognitive and emotional demands. *Journal of Neuroscience*, *25*(37), 8402–8406.

25. DeAngelis, G. C., Cumming, B. G., & Newsome, W. T. (1998). Cortical area MT and the perception of stereoscopic depth. *Nature*, *394*(6694), 677–680.

26. Dilks, D. D., Baker, C. I., Liu, Y., & Kanwisher, N. (2009). "Referred visual sensations": rapid perceptual elongation after visual cortical deprivation. *Journal of Neuroscience*, *29*(28), 8960–8964.

27. Dosenbach, N. U., Visscher, K. M., Palmer, E. D., Miezin, F. M., Wenger, K. K., Kang, H. C., Burgund, E. D., Grimes, A. L., Schlaggar, B. L., & Petersen, S. E. (2006). A core system for the implementation of task sets. *Neuron*, *50*(5), 799–812.

28. Dowling, J. E. (2012). *The retina: An approachable part of the brain*. Belknap Press of Harvard University Press.

29. Dumoulin, S. O., & Wandell, B. A. (2008). Population receptive field estimates in human visual cortex. *NeuroImage*, *39*(2), 647–660.
30. Duncan, R. O., Sample, P. A., Weinreb, R. N., Bowd, C., & Zangwill, L. M. (2007). Retinotopic organization of primary visual cortex in glaucoma: Comparing fMRI measurements of cortical function with visual field loss. *Progress in Retinal and Eye Research*, *26*(1), 38–56.
31. Eckert, M. A., Kamdar, N. V., Chang, C. E., Beckmann, C. F., Greicius, M. D., & Menon, V. (2008). A cross-modal system linking primary auditory and visual cortices: evidence from intrinsic fMRI connectivity analysis. *Human Brain Mapping*, *29*(7), 848–857.
32. Ferreira, S., Pereira, A. C., Quendera, B., Reis, A., Silva, E. D., & Castelo-Branco, M. (2016). Primary visual cortical remapping in patients with inherited peripheral retinal degeneration. *NeuroImage. Clinical*, *13*, 428–438.
33. Fujiwara, K., Ikeda, Y., Murakami, Y., Tachibana, T., Funatsu, J., Koyanagi, Y., Nakatake, S., Yoshida, N., Nakao, S., Hisatomi, T., Yoshida, S., Yoshitomi, T., Ishibashi, T., & Sonoda, K. H. (2018). Assessment of Central Visual Function in Patients with Retinitis Pigmentosa. *Scientific Reports*, *8*(1), 8070.
34. Gameiro, R. R., Jünemann, K., Herbik, A., Wolff, A., König, P., & Hoffmann, M. B. (2018). Natural visual behavior in individuals with peripheral visual-field loss. *Journal of Vision*, *18*(12), 10.
35. Gao, J., Zeng, M., Dai, X., Yang, X., Yu, H., Chen, K., Hu, Q., Xu, J., Cheng, B., & Wang, J. (2020). Functional Segregation of the Middle Temporal Visual Motion Area Revealed with Coactivation-Based Parcellation. *Frontiers in Neuroscience*, *14*, 427.
36. Gattass, R., Nascimento-Silva, S., Soares, J. G., Lima, B., Jansen, A. K., Diogo, A. C., Farias, M. F., Botelho, M. M., Mariani, O. S., Azzi, J., & Fiorani, M. (2005). Cortical visual areas in monkeys: location, topography, connections, columns, plasticity and cortical dynamics. *Biological Sciences*, *360*(1456), 709–731.
37. Gerth, C., Wright, T., Héon, E., & Westall, C. A. (2007). Assessment of central retinal function in patients with advanced retinitis pigmentosa. *Investigative Ophthalmology & Visual Science*, *48*(3), 1312–1318.
38. Gharabaghi, A., Fruhmann Berger, M., Tatagiba, M., & Karnath, H. O. (2006). The role of the right superior temporal gyrus in visual search-insights from intraoperative electrical stimulation. *Neuropsychologia*, *44*(12), 2578–2581.
39. Giannikopoulos, D. V., & Eysel, U. T. (2006). Dynamics and specificity of cortical map reorganization after retinal lesions. *PNAS*, *103*(28), 10805–10810.
40. Gilbert, C. D., & Li, W. (2012). Adult visual cortical plasticity. *Neuron*, *75*(2), 250–264.
41. Gilbert, C. D., & Wiesel, T. N. (1992). Receptive field dynamics in adult primary visual cortex. *Nature*, *356*(6365), 150–152.
42. Gomez, J., Zhen, Z., & Weiner, K. S. (2019). Human visual cortex is organized along two genetically opposed hierarchical gradients with unique developmental and evolutionary origins. *PLoS Biology*, *17*(7), e3000362.

43. Guadron, L., Titchener, S. A., Abbott, C. J., Ayton, L. N., van Opstal, J., Petoe, M. A., & Goossens, J. (2023). The saccade Main Sequence in Patients with Retinitis Pigmentosa and Advanced Age-Related Macular Degeneration. *Investigative Ophthalmology & Visual Science*, *64*(3), 1.

44. Haak, K. V., Cornelissen, F. W., & Morland, A. B. (2012). Population receptive field dynamics in human visual cortex. *PloS One*, *7*(5), e37686.

45. Haak, K. V., Fast, E., Bao, M., Lee, M., & Engel, S. A. (2014). Four days of visual contrast deprivation reveals limits of neuronal adaptation. *Current Biology, 24*(21), 2575–2579.

46. Haak, K. V., Morland, A. B., & Engel, S. A. (2015). Plasticity, and Its Limits, in Adult Human Primary Visual Cortex. *Multisensory Research*, *28*(3-4), 297–307.

47. Haak, K. V., Morland, A. B., Rubin, G. S., & Cornelissen, F. W. (2016). Preserved retinotopic brain connectivity in macular degeneration. *Journal of the British College of Ophthalmic Opticians (Optometrists)*, *36*(3), 335–343.

48. Hamel C. (2006). Retinitis pigmentosa. *Orphanet Journal of Rare Diseases*, *1*, 40.

49. Harting, J. K., & Updyke, B. V. (2006). Oculomotor-related pathways of the basal ganglia. *Progress in Brain Research*, *151*, 441–460.

50. Harvey, B. M., & Dumoulin, S. O. (2011). The relationship between cortical magnification factor and population receptive field size in human visual cortex: constancies in cortical architecture. *Journal of Neuroscience*, *31*(38), 13604–13612.

51. He, S., Cavanagh, P., & Intriligator, J. (1996). Attentional resolution and the locus of visual awareness. *Nature*, *383*(6598), 334–337.

52. Herse P. (2005). Retinitis pigmentosa: visual function and multidisciplinary management. *Clinical & Experimental Optometry*, *88*(5), 335–350.

53. Himmelberg, M. M., Tünçok, E., Gomez, J., Grill-Spector, K., Carrasco, M., & Winawer, J. (2023). Comparing retinotopic maps of children and adults reveals a late-stage change in how V1 samples the visual field. *Nature Communications*, *14*(1), 1561.

54. Huang, C. W., Yang, J. J., Yang, C. H., Yang, C. M., Hu, F. R., Ho, T. C., & Chen, T. C. (2021). The structure-function correlation analysed by OCT and full field ERG in typical and pericentral subtypes of retinitis pigmentosa. *Scientific Reports*, *11*(1), 16883.

55. Hubel, D. H., & Wiesel, T. N. (1959). Receptive fields of single neurones in the cat's striate cortex. *Journal of Physiology*, *148*(3), 574-591.

56. Hubel, D. H., & Wiesel, T. N. (1968). Receptive fields and functional architecture of monkey striate cortex. *The Journal of physiology, 195*(1), 215–243. https://doi.org/10.1113/jphysiol.1968.sp008455

57. Hubel, D. H., & Wiesel, T. N. (1977). Ferrier lecture. Functional architecture of macaque monkey visual cortex. *Biological Sciences*, *198*(1130), 1–59.

58. Huk, A. C., Dougherty, R. F., & Heeger, D. J. (2002). Retinotopy and functional subdivision of human areas MT and MST. *Journal of Neuroscience, 22*(16), 7195–7205.

59. Jamal, Y. A., & Dilks, D. D. (2020). Rapid topographic reorganization in adult human primary visual cortex (V1) during noninvasive and reversible deprivation. *PNAS*, *117*(20), 11059–11067.

60. Jansen, M., Jin, J., Li, X., Lashgari, R., Kremkow, J., Bereshpolova, Y., Swadlow, H. A., Zaidi, Q., & Alonso, J. M. (2019). Cortical Balance Between ON and OFF Visual Responses Is Modulated by the Spatial Properties of the Visual Stimulus. *Cerebral Cortex, 29*(1), 336–355.

61. Jimenez, L. O., Tring, E., Trachtenberg, J. T., & Ringach, D. L. (2018). Local tuning biases in mouse primary visual cortex. *Journal of Neurophysiology*, *120*(1), 274–280.

62. Jin, Z., Jin, D. G., Xiao, M., Ding, A., Tian, J., Zhang, J., & Li, L. (2022). Structural and functional MRI evidence for significant contribution of precentral gyrus to flexible oculomotor control: evidence from the antisaccade task. *Brain Structure & Function*, *227*(8), 2623–2632.

63. Kandel, E. R., Schwartz, J. H., Jessell, T. M., Siegelbaum, S., Hudspeth, A. J., & Mack, S. (Eds.). (2000). *Principles of Neural Science, 4*, 1227-1246. New York: McGraw-hill.

64. Karnath, H. O., Ferber, S., & Himmelbach, M. (2001). Spatial awareness is a function of the temporal not the posterior parietal lobe. *Nature*, *411*(6840), 950–953.

65. Kaas, J. H., Krubitzer, L. A., Chino, Y. M., Langston, A. L., Polley, E. H., & Blair, N. (1990). Reorganization of retinotopic cortical maps in adult mammals after lesions of the retina. *Science*, *248*(4952), 229–231.

66. Kay, K. N., Winawer, J., Rokem, A., Mezer, A., & Wandell, B. A. (2013). A two-stage cascade model of BOLD responses in human visual cortex. *PLoS Computational Biology*, *9*(5), e1003079.

67. Kolb, H. (2001). Circuitry for Rod Signals through the Retina. In H. Kolb (Eds.) et. al., Webvision: The Organization of the Retina and Visual System. University of Utah Health Sciences Center.

68. Kozak, A., Wieteska, M., Ninghetto, M., Szulborski, K., Gałecki, T., Szaflik, J., & Burnat, K. (2021). Motion-Based Acuity Task: Full Visual Field Measurement of Shape and Motion Perception. *Translational Vision Science & Technology*, *10*(1), 9.

69. Kremkow, J., Jin, J., Wang, Y., & Alonso, J. M. (2016). Principles underlying sensory map topography in primary visual cortex. *Nature*, *533*(7601), 52–57.

70. Kunimatsu, J., Maeda, K., & Hikosaka, O. (2019). The Caudal Part of Putamen Represents the Historical Object Value Information. *Journal of Neuroscience*, *39*(9), 1709–1719.

71. Lanciego, J. L., Luquin, N., & Obeso, J. A. (2012). Functional neuroanatomy of the basal ganglia. *Cold Spring Harbor Perspectives in Medicine*, *2*(12), a009621.

72. Laskowska-Macios, K., Nys, J., Hu, T. T., Zapasnik, M., Van der Perren, A., Kossut, M., Burnat, K., & Arckens, L. (2015). Binocular pattern deprivation interferes with the expression of proteins involved in primary visual cortex maturation in the cat. *Molecular Brain*, *8*, 48.

73. Laskowska-Macios, K., Zapasnik, M., Hu, T. T., Kossut, M., Arckens, L., & Burnat, K. (2015). Zif268 mRNA Expression Patterns Reveal a Distinct Impact of Early Pattern Vision Deprivation on the Development of Primary Visual Cortical Areas in the Cat. *Cerebral Cortex*, *25*(10), 3515–3526.

74. Li, H., Hu, D., Tanigawa, H., & Takahata, T. (2024). Topographic organization across foveal visual areas in macaques. *Frontiers in neuroanatomy, 18*, 1389067.

75. Luo-Li, G., Mazade, R., Zaidi, Q., Alonso, J. M., & Freeman, A. W. (2018). Motion changes response balance between ON and OFF visual pathways. *Communications Biology*, *1*, 60.

76. Luttrull J. K. (2018). Improved retinal and visual function following panmacular subthreshold diode micropulse laser for retinitis pigmentosa. *Eye*, *32*(6), 1099–1110.

77. Masuda, Y., Dumoulin, S. O., Nakadomari, S., & Wandell, B. A. (2008). V1 projection zone signals in human macular degeneration depend on task, not stimulus. *Cerebral Cortex*, *18*(11), 2483–2493.

78. Masuda, Y., Horiguchi, H., Dumoulin, S. O., Furuta, A., Miyauchi, S., Nakadomari, S., & Wandell, B. A. (2010). Task-dependent V1 responses in human retinitis pigmentosa. *Investigative Ophthalmology & Visual Science*, *51*(10), 5356–5364.

79. Masuda, Y., Dumoulin, S. O., Nakadomari, S., & Wandell, B. A. (2008). V1 projection zone signals in human macular degeneration depend on task, not stimulus. *Cerebral Cortex*, *18*(11), 2483–2493.

80. Masuda, Y., Horiguchi, H., Dumoulin, S. O., Furuta, A., Miyauchi, S., Nakadomari, S., & Wandell, B. A. (2010). Task-dependent V1 responses in human retinitis pigmentosa. *Investigative Ophthalmology & Visual Science*, *51*(10), 5356–5364.

81. Mazade, R., Jin, J., Pons, C., & Alonso, J. M. (2019). Functional Specialization of ON and OFF Cortical Pathways for Global-Slow and Local-Fast Vision. *Cell Reports*, *27*(10), 2881–2894.e5.

82. Menon, V., & Uddin, L. Q. (2010). Saliency, switching, attention and control: a network model of insula function. *Brain Structure & Function*, *214*(5-6), 655–667.

83. Nguyen, X. T., Moekotte, L., Plomp, A. S., Bergen, A. A., van Genderen, M. M., & Boon, C. J. F. (2023). Retinitis Pigmentosa: Current Clinical Management and Emerging Therapies. *International Journal of Molecular Sciences*, *24*(8), 7481.

84. Ninghetto, M., Wieteska, M., Kozak, A., Szulborski, K., Gałecki, T., Szaflik, J., & Burnat, K. (2024). Motion-Acuity Test for Visual Field Acuity Measurement with Motion-Defined Shapes. *Journal of Visualized Experiments*, (204), 10.3791/66272.

85. Ninghetto, M., Kozak, A., Gałecki, T., Szulborski, K., Szaflik, J. P., Ołdak, M., Marchewka, A., & Burnat, K. (2024). Good vision without peripheries: behavioral and fMRI evidence. *Scientific Reports*, *14*(1), 26264.

86. Nurminen, L., Merlin, S., Bijanzadeh, M., Federer, F., & Angelucci, A. (2018). Top-down feedback controls spatial summation and response amplitude in primate visual cortex. *Nature Communications*, *9*(1), 2281.

87. Oishi, M., Nakamura, H., Hangai, M., Oishi, A., Otani, A., & Yoshimura, N. (2012). Contrast visual acuity in patients with retinitis pigmentosa assessed by a contrast sensitivity tester. *Indian Journal of Ophthalmology*, *60*(6), 545–549.

88. Orban, G. A., Kennedy, H., & Bullier, J. (1986). Velocity sensitivity and direction selectivity of neurons in areas V1 and V2 of the monkey: influence of eccentricity. *Journal of Neurophysiology*, *56*(2), 462–480.

89. Panneman, D. M., Hitti-Malin, R. J., Holtes, L. K., de Bruijn, S. E., Reurink, J., Boonen, E. G. M., Khan, M. I., Ali, M., Andréasson, S., De Baere, E., Banfi, S., Bauwens, M., Ben-Yosef, T., Bocquet, B., De Bruyne, M., de la Cerda, B., Coppieters, F., Farinelli, P., Guignard, T., Inglehearn, C. F., … Roosing, S. (2023). Cost-effective sequence analysis of 113 genes in 1,192 probands with retinitis pigmentosa and Leber congenital amaurosis. *Frontiers in Cell and Developmental Biology*, *11*, 1112270.

90. Papanikolaou, A., Keliris, G. A., Papageorgiou, T. D., Shao, Y., Krapp, E., Papageorgiou, E., Stingl, K., Bruckmann, A., Schiefer, U., Logothetis, N. K., & Smirnakis, S. M. (2014). Population receptive field analysis of the primary visual cortex complements perimetry in patients with homonymous visual field defects. *PNAS*, *111*(16), E1656–E1665.

91. Papanikolaou, A., Keliris, G. A., Papageorgiou, T. D., Schiefer, U., Logothetis, N. K., & Smirnakis, S. M. (2019). Organization of area hV5/MT+ in subjects with homonymous visual field defects. *NeuroImage*, *190*, 254–268.

92. Pawloff, M., Linhardt, D., Woletz, M., Hummer, A., Sacu, S., Vasileiadi, M., Garikoitz, L. U., Holder, G., Schmidt-Erfurth, U. M., Windischberger, C., & Ritter, M. (2023). Comparison of Stimulus Types for Retinotopic Cortical Mapping of Macular Disease. *Translational Vision Science & Technology*, *12*(3), 6.

93. Pettet, M. W., & Gilbert, C. D. (1992). Dynamic changes in receptive-field size in cat primary visual cortex. *PNAS*, *89*(17), 8366–8370.

94. Phillips, J. M., & Everling, S. (2012). Neural activity in the macaque putamen associated with saccades and behavioral outcome. *PloS One*, *7*(12), e51596.

95. Polyak, S.L. (1941). The retina: the anatomy and the histology of the retina in man, ape, and monkey, including the consideration of visual functions, the history of physiological optics, and the histological laboratory technique. *University of Chicago Press: Chicago*.

96. Prabhakaran, G. T., Al-Nosairy, K. O., Tempelmann, C., Thieme, H., & Hoffmann, M. B. (2021). Mapping Visual Field Defects With fMRI - Impact of Approach and Experimental Conditions. *Frontiers in Neuroscience*, *15*, 745886.

97. Prabhakaran, G. T., Carvalho, J., Invernizzi, A., Kanowski, M., Renken, R. J., Cornelissen, F. W., & Hoffmann, M. B. (2020). Foveal pRF properties in the visual cortex depend on the extent of stimulated visual field. *NeuroImage*, *222*, 117250.

98. Provis, J. M., Dubis, A. M., Maddess, T., & Carroll, J. (2013). Adaptation of the central retina for high acuity vision: cones, the fovea and the avascular zone. *Progress in retinal and eye research, 35*, 63–81.

99. Purves, D., Augustine, G. J., Fitzpatrick, D., Hall, W. C., LaManita, A.-S., & White, L. E. (Eds.). Vision: The Eye. (2012). *Neuroscience* (5th ed.). Sinauer Associates.
100. Quirmbach, F., & Limanowski, J. (2022). A Crucial Role of the Frontal Operculum in Task-Set Dependent Visuomotor Performance Monitoring. *eNeuro*, *9*(2), ENEURO.0524-21.2021.
101. Rabin, J. C. (2015). The new visual neurosciences. In J. S. Werner & L. M. Chalupa (Eds.), The new visual neurosciences. MIT Press.
102. Rahimi-Nasrabadi, H., Jin, J., Mazade, R., Pons, C., Najafian, S., & Alonso, J. M. (2021). Image luminance changes contrast sensitivity in visual cortex. *Cell Reports*, *34*(5), 108692.
103. Rektor, I., Bares, M., Kanovský, P., & Kukleta, M. (2001). Intracerebral recording of readiness potential induced by a complex motor task. *Movement Disorders, 16*(4), 698–704.
104. Ritter, M., Hummer, A., Ledolter, A. A., Holder, G. E., Windischberger, C., & Schmidt-Erfurth, U. M. (2019). Correspondence between retinotopic cortical mapping and conventional functional and morphological assessment of retinal disease. *The British Journal of Ophthalmology*, *103*(2), 208–215.
105. Rodieck, R. W. (1998). The first steps in seeing. Sinauer Associates.
106. Roska, B., & Sahel, J. A. (2018). Restoring vision. *Nature*, *557*(7705), 359–367.
107. Rossit, S., McAdam, T., Mclean, A., Goodale, M., & Culham, J. (2011). fMRI reveals a lower visual field preference in dorsal visual stream regions during hand actions. *Journal of Vision, 11*(11), 952-952.
108. Sabbah, N., Authié, C. N., Sanda, N., Mohand-Saïd, S., Sahel, J. A., Safran, A. B., Habas, C., & Amedi, A. (2016). Increased functional connectivity between language and visually deprived areas in late and partial blindness. *NeuroImage*, *136*, 162–173.
109. Sahel, J. A., Marazova, K., & Audo, I. (2014). Clinical characteristics and current therapies for inherited retinal degenerations. *Cold Spring Harbor Perspectives in Medicine*, *5*(2), a017111.
110. Sanda, N., Cerliani, L., Authié, C. N., Sabbah, N., Sahel, J. A., Habas, C., Safran, A. B., & Thiebaut de Schotten, M. (2018). Visual brain plasticity induced by central and peripheral visual field loss. *Brain Structure & Function*, *223*(7), 3473–3485.
111. Sandberg, M. A., Brockhurst, R. J., Gaudio, A. R., & Berson, E. L. (2005). The association between visual acuity and central retinal thickness in retinitis pigmentosa. *Investigative Ophthalmology & Visual Science*, *46*(9), 3349–3354.
112. Schein, S. J., & de Monasterio, F. M. (1987). Mapping of retinal and geniculate neurons onto striate cortex of macaque. *Journal Of Neuroscience*, *7*(4), 996–1009.
113. Ścieżyńska, A., Oziębło, D., Ambroziak, A. M., Korwin, M., Szulborski, K., Krawczyński, M., Stawiński, P., Szaflik, J., Szaflik, J. P., Płoski, R., & Ołdak, M. (2016). Next-generation sequencing of ABCA4: High frequency of complex alleles and novel mutations in patients with retinal dystrophies from Central Europe. *Experimental Eye Research*, *145*, 93–99.

114. Seeley, W. W., Menon, V., Schatzberg, A. F., Keller, J., Glover, G. H., Kenna, H., Reiss, A. L., & Greicius, M. D. (2007). Dissociable intrinsic connectivity networks for salience processing and executive control. *Journal of Neuroscience*, *27*(9), 2349–2356.

115. Sereno, M. I., McDonald, C. T., & Allman, J. M. (1994). Analysis of retinotopic maps in extrastriate cortex. *Cerebral Cortex, 4*(6), 601–620.

116. Sereno, M. I., Dale, A. M., Reppas, J. B., Kwong, K. K., Belliveau, J. W., Brady, T. J., Rosen, B. R., & Tootell, R. B. (1995). Borders of multiple visual areas in humans revealed by functional magnetic resonance imaging. *Science*, *268*(5212), 889–893.

117. Shah-Basak, P. P., Chen, P., Caulfield, K., Medina, J., & Hamilton, R. H. (2018). The role of the right superior temporal gyrus in stimulus-centered spatial processing. *Neuropsychologia*, *113*, 6–13.

118. Sheth, S. A., Mian, M. K., Patel, S. R., Asaad, W. F., Williams, Z. M., Dougherty, D. D., Bush, G., & Eskandar, E. N. (2012). Human dorsal anterior cingulate cortex neurons mediate ongoing behavioural adaptation. *Nature*, *488*(7410), 218–221.

119. Silson, E. H., Aleman, T. S., Willett, A., Serrano, L. W., Pearson, D. J., Rauschecker, A. M., Maguire, A. M., Baker, C. I., Bennett, J., & Ashtari, M. (2018). Comparing Clinical Perimetry and Population Receptive Field Measures in Patients with Choroideremia. *Investigative Ophthalmology & Visual Science*, *59*(8), 3249–3258.

120. Silva, M. F., Harvey, B. M., Jorge, L., Canário, N., Machado, F., Soares, M., d'Almeida, O. C., & Castelo-Branco, M. (2021). Simultaneous changes in visual acuity, cortical population receptive field size, visual field map size, and retinal thickness in healthy human aging. *Brain Structure & Function*, *226*(9), 2839–2853.

121. Striem-Amit, E., Ovadia-Caro, S., Caramazza, A., Margulies, D. S., Villringer, A., & Amedi, A. (2015). Functional connectivity of visual cortex in the blind follows retinotopic organization principles. *Brain*, *138*(Pt 6), 1679–1695.

122. Thompson, A., Gribizis, A., Chen, C., & Crair, M. C. (2017). Activity-dependent development of visual receptive fields. *Current Opinion in Neurobiology*, *42*, 136–143.

123. Tootell, R. B., Reppas, J. B., Kwong, K. K., Malach, R., Born, R. T., Brady, T. J., Rosen, B. R., & Belliveau, J. W. (1995). Functional analysis of human MT and related visual cortical areas using magnetic resonance imaging. *Journal of Neuroscience*, *15*(4), 3215–3230.

124. Tootell, R. B., Hadjikhani, N., Hall, E. K., Marrett, S., Vanduffel, W., Vaughan, J. T., & Dale, A. M. (1998). The retinotopy of visual spatial attention. *Neuron*, *21*(6), 1409–1422.

125. Uddin L. Q. (2015). Salience processing and insular cortical function and dysfunction. *Nature Reviews. Neuroscience*, *16*(1), 55–61.

126. Walker, H. K., Hall, W. D., & Hurst, J. W. (Eds.). (1990). Clinical methods: The history, physical, and laboratory examinations (3rd ed.). Butterworths.

127. Wandell, B. A., Dumoulin, S. O., & Brewer, A. A. (2007). Visual field maps in human cortex. *Neuron*, *56*(2), 366–383.

128. Wandell, B. A., & Winawer, J. (2015). Computational neuroimaging and population receptive fields. *Trends in Cognitive Sciences*, *19*(6), 349–357.

129. Wang, L., Mruczek, R. E., Arcaro, M. J., & Kastner, S. (2015). Probabilistic Maps of Visual Topography in Human Cortex. *Cerebral Cortex*, *25*(10), 3911–3931.

130. Wang, H., Ouyang, W., Liu, Y., Zhang, M., Zhao, H., Wang, J., & Yin, Z. (2022). Visual task-related functional and structural magnetic resonance imaging for the objective quantitation of visual function in patients with advanced retinitis pigmentosa. *Frontiers in Aging Neuroscience*, *14*, 825204.

131. Wässle H. (2004). Parallel processing in the mammalian retina. *Nature Reviews. Neuroscience*, *5*(10), 747–757.

132. Weber, A., Hohberger, B., & Bergua, A. (2021). Mouth-nose masks impair the visual field of healthy eyes. *PloS One*, *16*(5), e0251201.

133. Weintraub, S., & Mesulam, M. M. (1987). Right cerebral dominance in spatial attention. Further evidence based on ipsilateral neglect. *Archives of Neurology*, *44*(6), 621–625.

134. Wypych, M., Michałowski, J. M., Droździel, D., Borczykowska, M., Szczepanik, M., & Marchewka, A. (2019). Attenuated brain activity during error processing and punishment anticipation in procrastination - a monetary Go/No-go fMRI study. *Scientific Reports*, *9*(1), 11492.

135. Yeh, C. I., Xing, D., & Shapley, R. M. (2009). "Black" responses dominate macaque primary visual cortex v1. *Journal of Neuroscience*, *29*(38), 11753–11760.

136. Zapasnik, M., & Burnat, K. (2013). Binocular pattern deprivation with delayed onset has impact on motion perception in adulthood. *Neuroscience*, *255*, 99–109.

137. Zemon, V., Gordon, J., & Welch, J. (1988). Asymmetries in ON and OFF visual pathways of humans revealed using contrast-evoked cortical potentials. *Visual Neuroscience*, *1*(1), 145–150.

8. Appendix

9.1. pRF exclusion criteria

Despite the size of the patient groups for the pRF mapping procedure counted twenty-three RP and twenty-one STGD patients, the original number of recruited patients was higher (forty-five for RP patients and twenty-four for STGD patients). A first screening was performed by cutting off from the analyses patients that were not able to see the stimuli on the monitor or that needed a caregiver to orient in the space or that did not meet the inclusion criteria for the MRI procedure (e.g., someone who had metallic implants in their body). From the RP patients group, we removed for these reasons, patient 2 (totally blind), 15, 17, 18, 21, 22, 24 and 43 (totally blind), reducing the group size to thirty-seven patients. In the same way, we removed from the initial STGD patients group, patient 2, 13 and 15, reducing the group size to twenty-one patients.

Moreover, since the RP patients were tested in both unrestricted and limited vision conditions, we included in the analysis only the RP patients that were able to see the stimuli in both procedures; for this reason, patient 1, 5, 6, 9, 12, 14, 20, 30, 31, 37, 38, 39, 40 and 45 were not included, reducing the group size to twenty-three. On the other hand, STGD patients were not tested with the narrowing goggles as they already suffer from loss of central vision and removing peripheral vision would have made it impossible for them to see clearly.

9.2. Fixation maps during pRF session

During the scanning session, we asked the participants to press a button on a response pad every time the fixation point would change its color at random intervals, alternating between red and green; unfortunately, we were not able to use this measure for most of the patients, since most of them, together with other symptoms due to their eye disease, were not able to detect changes in colors. Yet, since we performed eye tracker recording during the fMRI protocol, we were able to merge fixations for each group, resulting in a fixation heatmap to visualize the average eye fixations across the entire scanning session.

The fixation heatmaps show on a black background, a green “blob” with darker area representing the point where fixations lasted longer. Lighter areas, instead, are where fixations felt for a shorter period. The location of the fixation point is depicted by the central crossed gray circle.

The center of the image represents the center of the screen where the fixation point was located. Despite all the effort to set and calibrate the camera as its best, we noticed that for controls and RP patients some of the subjects' recordings shifted the real center of the screen to a higher location. During the generation of the fixation maps this resulted in a heatmap with two centers of mass: 1 in the real center of the screen (exact calibration reproducing the real center), 2 a higher center of mass due to shifting in calibration. Nevertheless, by looking at these heatmaps, we can deduce that controls and patients' fixations were kept relatively stable at the center of the screen.

Mean Fixations heatmap for control group:

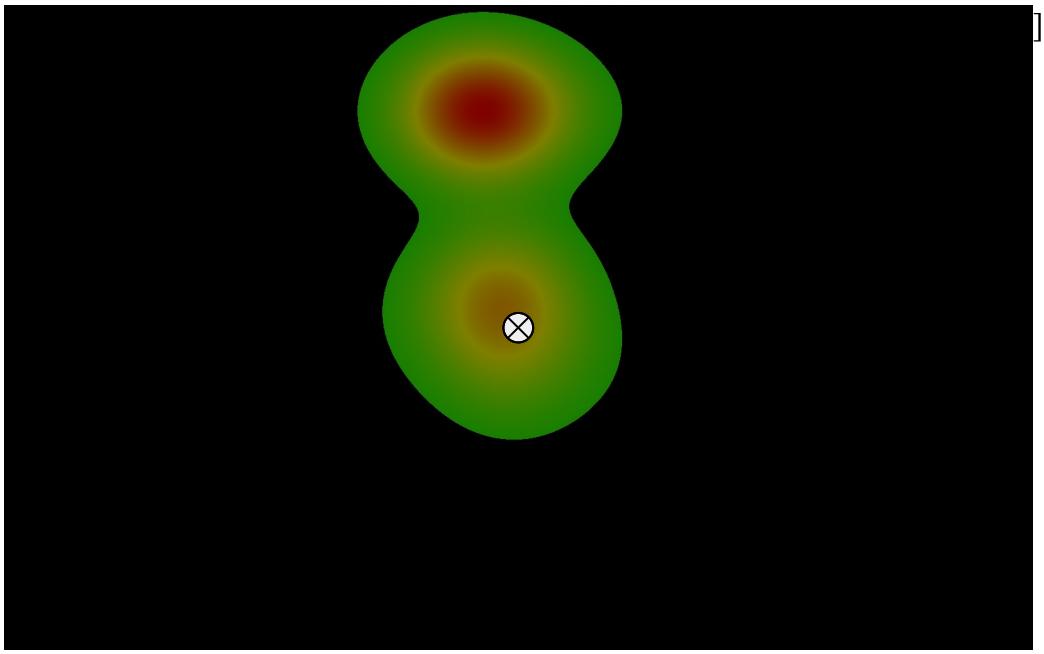

Mean Fixations heatmap for RP patients group

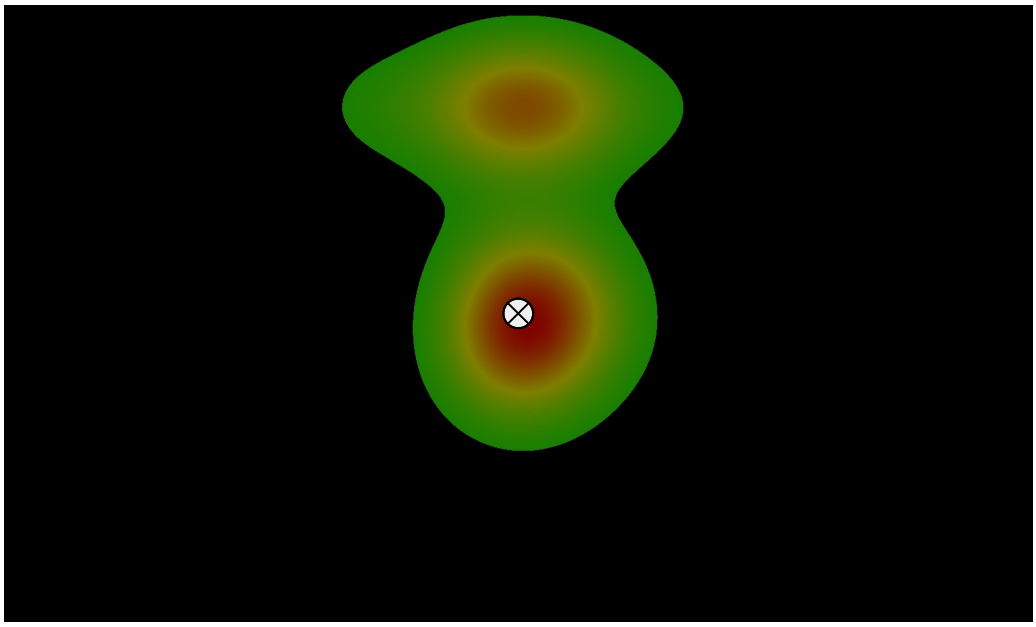

Mean Fixations heatmap for STGD patients group

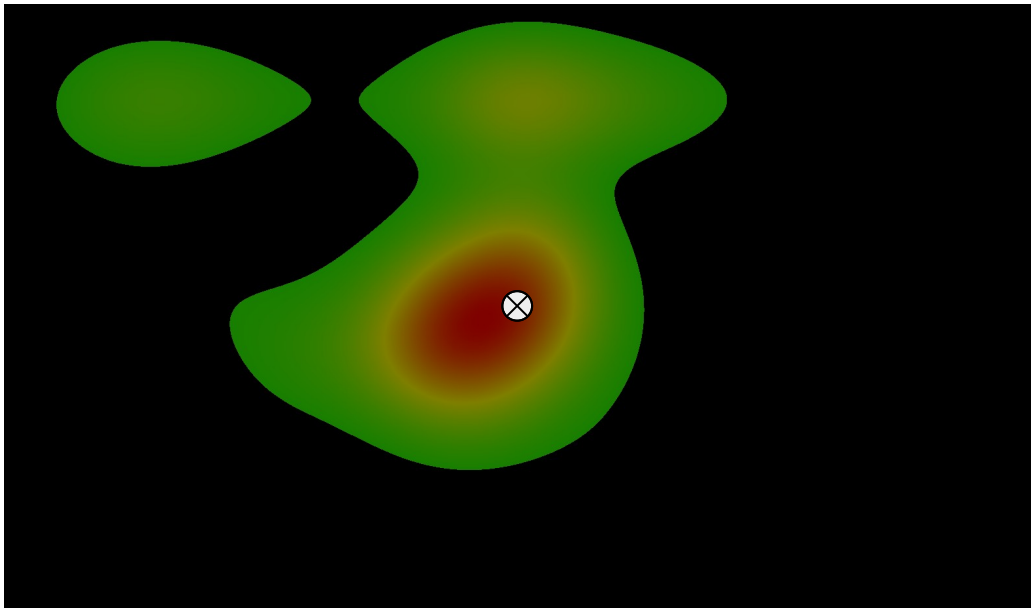

9.3. Individual pRF responses

To investigate individual pRF responses, we first performed Pearson correlation between individual mean pRF size in V1, V2, and V3 areas and the individual extents of patients' visual field in RP and STGD patients: to our surprise, we did not find any significant correlation. Results are shown in the below table:

Table 5 Pearson correlation between pRF size and Humphrey test

RP		**right V1**	**right V2**	**right V3**	**left V1**	**left V2**	**left V3**
center left eye	r	0.2436	0.0081	0.2001			
		p=.301	p=.973	p=.398			
center right eye	r				0.3203	0.2802	0.2131
					p=.169	p=.231	p=.367
fullfield left eye	r	0.1707	-0.0834	0.1362			
		p=.459	p=.719	p=.556			
fullfield right eye	r				0.2617	0.1194	0.1615
					p=.252	p=.606	p=.484
STGD							
center left eye	r	0.3526	0.3548	0.4174			
		p=.117	p=.115	p=.060			
center right eye	r				-0.1051	-0.4185	-0.3865
					p=.650	p=.059	p=.083
fullfield left eye	r	0.314	0.296	0.395			
		p=.164	p=.192	p=.076			
fullfield right eye	r				-0.206	-0.368	-0.246
					p=.370	p=.100	p=.282

Yet, we tried to visualize individual pRF responses by using a series of three-heatmaps for each group for eccentricities: 1-3 deg, 3-6 deg, 6-9 deg. Note that these heatmaps were generated during the collection of data; for this reason, the quantity of participants in each group may not match exactly the final numbers reported in our final manuscript. They helped us to estimate the quality of our data: for instance, we decided to remove V3a, MT+/V5 and V4 from our analysis. Importantly, we included all participants in our analysis, even participants showing low number of voxel and we treated them as a random factor in our GLM design; with this approach by treating individual as random factors, we improved the generalizability of the results ensuring that our analysis reflected the variability in the population while controlling for individual differences in the model. Each heatmap shows individuals (columns) and ROIs (rows) with dorsal ROIs on top and ventral ROIs at the bottom. The color of each heatmap is referred to a horizontal colorbar which indicates the pRF size, where white indicates pRF size equal to 0, the more the color goes to red the bigger the pRF size. Inside each cell, we reported the number of voxels.

Together with the described ROIs from our manuscript, these heatmaps also show responses for V3a and MT+/V5 and for V3v and V4.

First, we present heatmaps for the left hemisphere, followed by the right hemisphere.

Control group (n of voxels reported in cell)

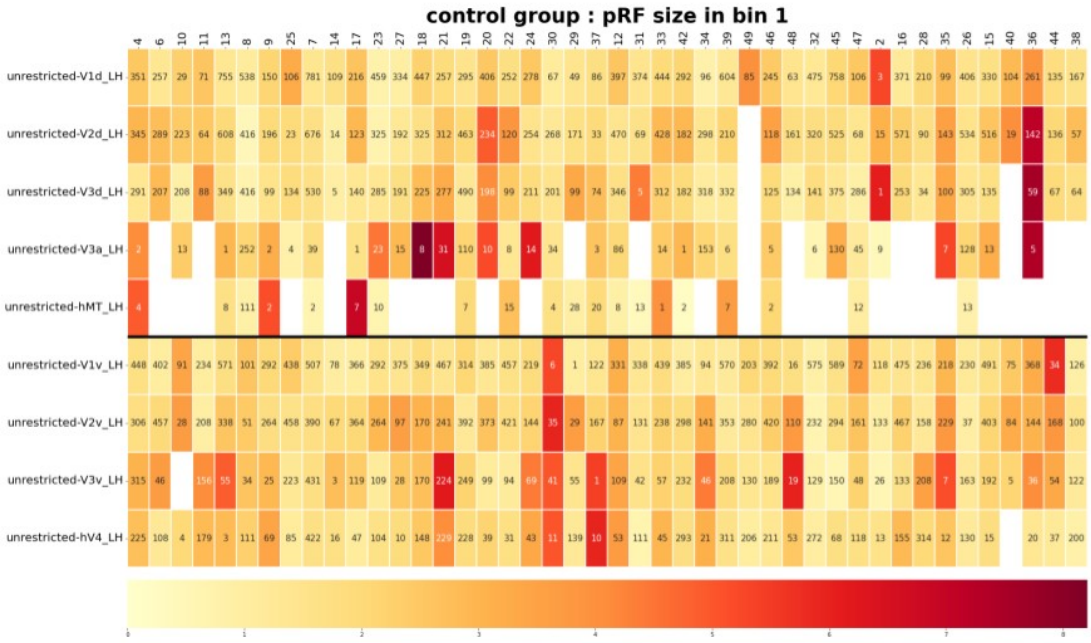

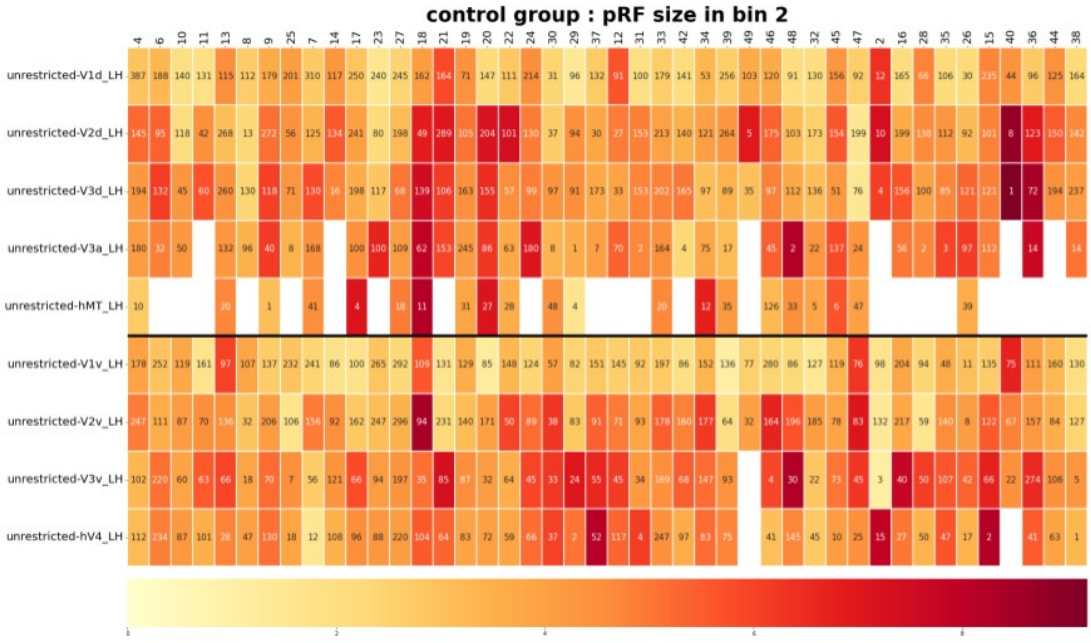

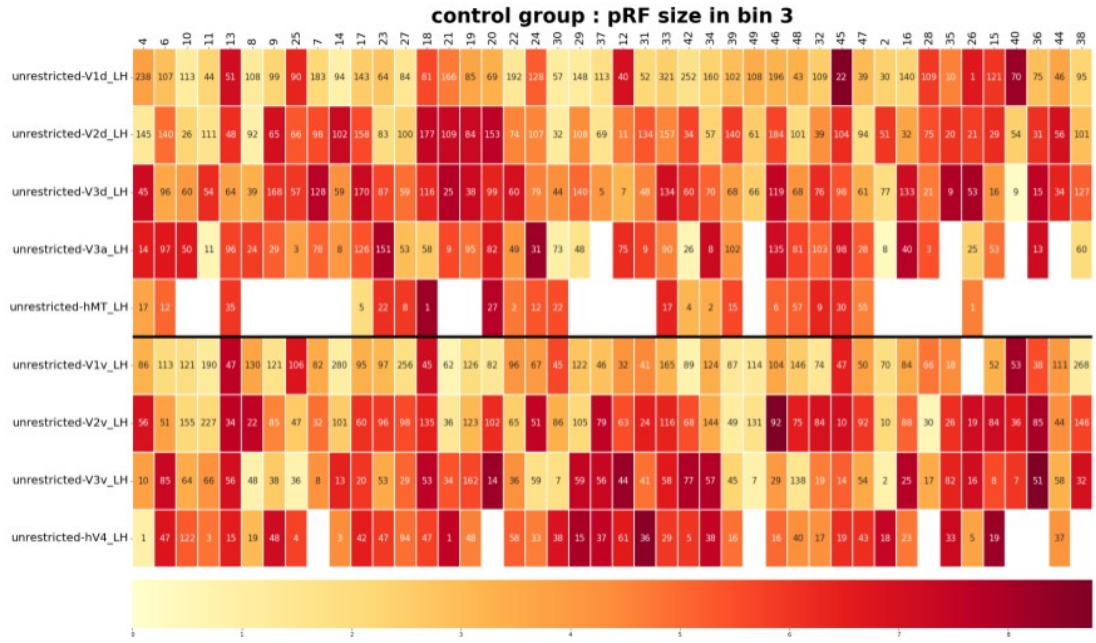

RP patients group (n of voxels reported in cell)

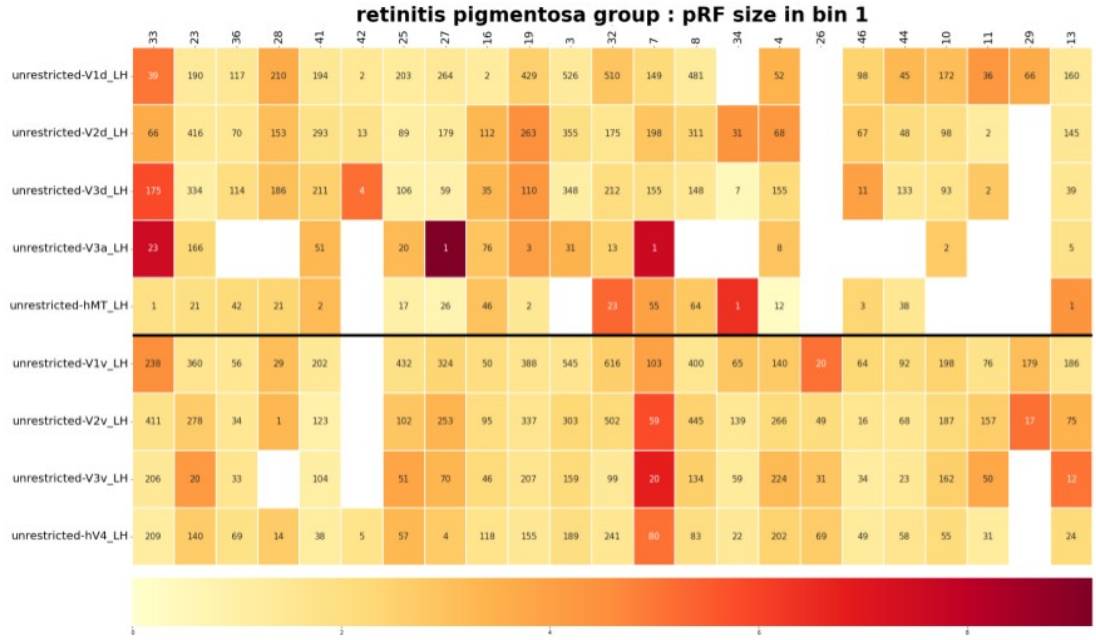

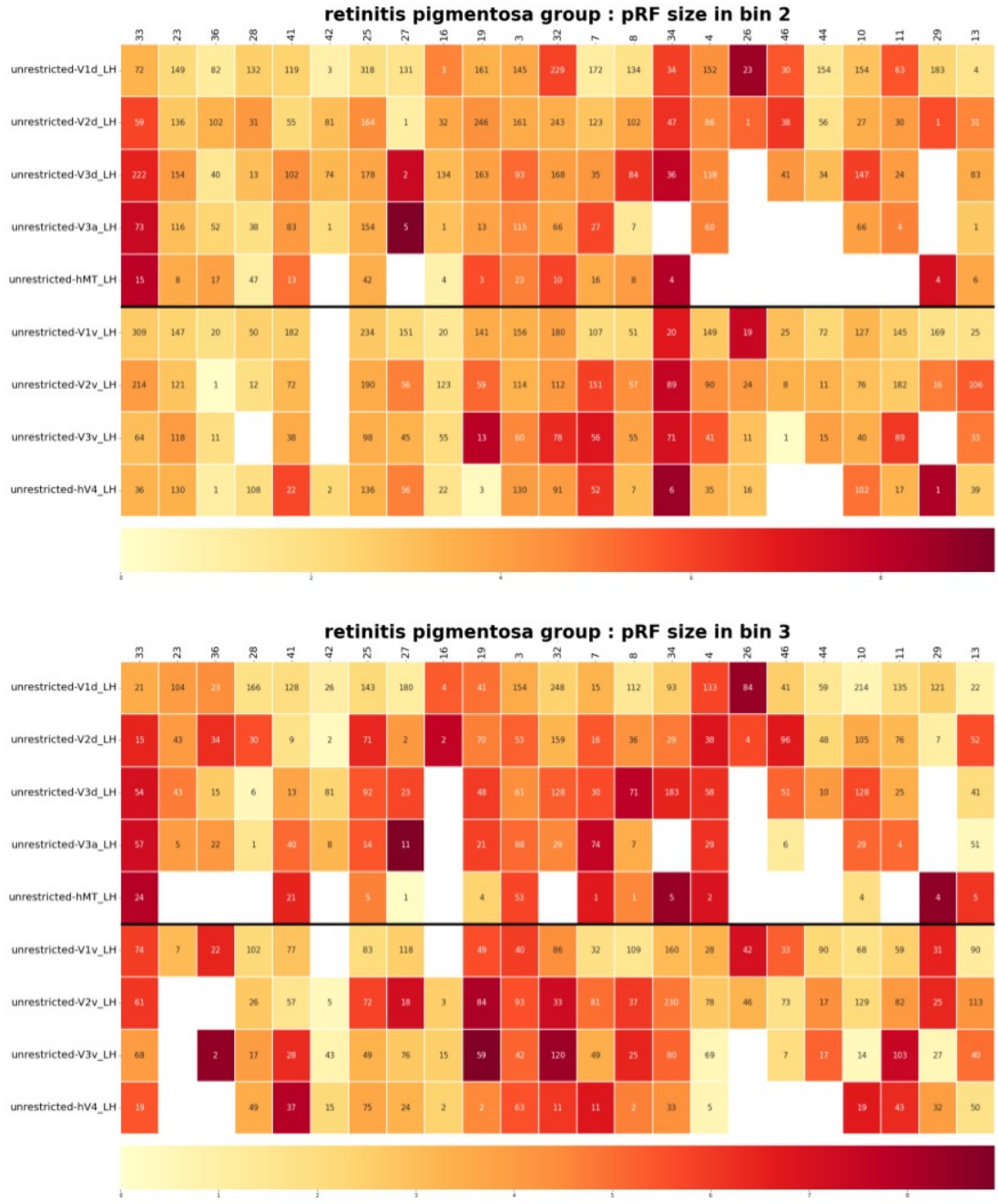

STGD patients group (n of voxels reported in cell)

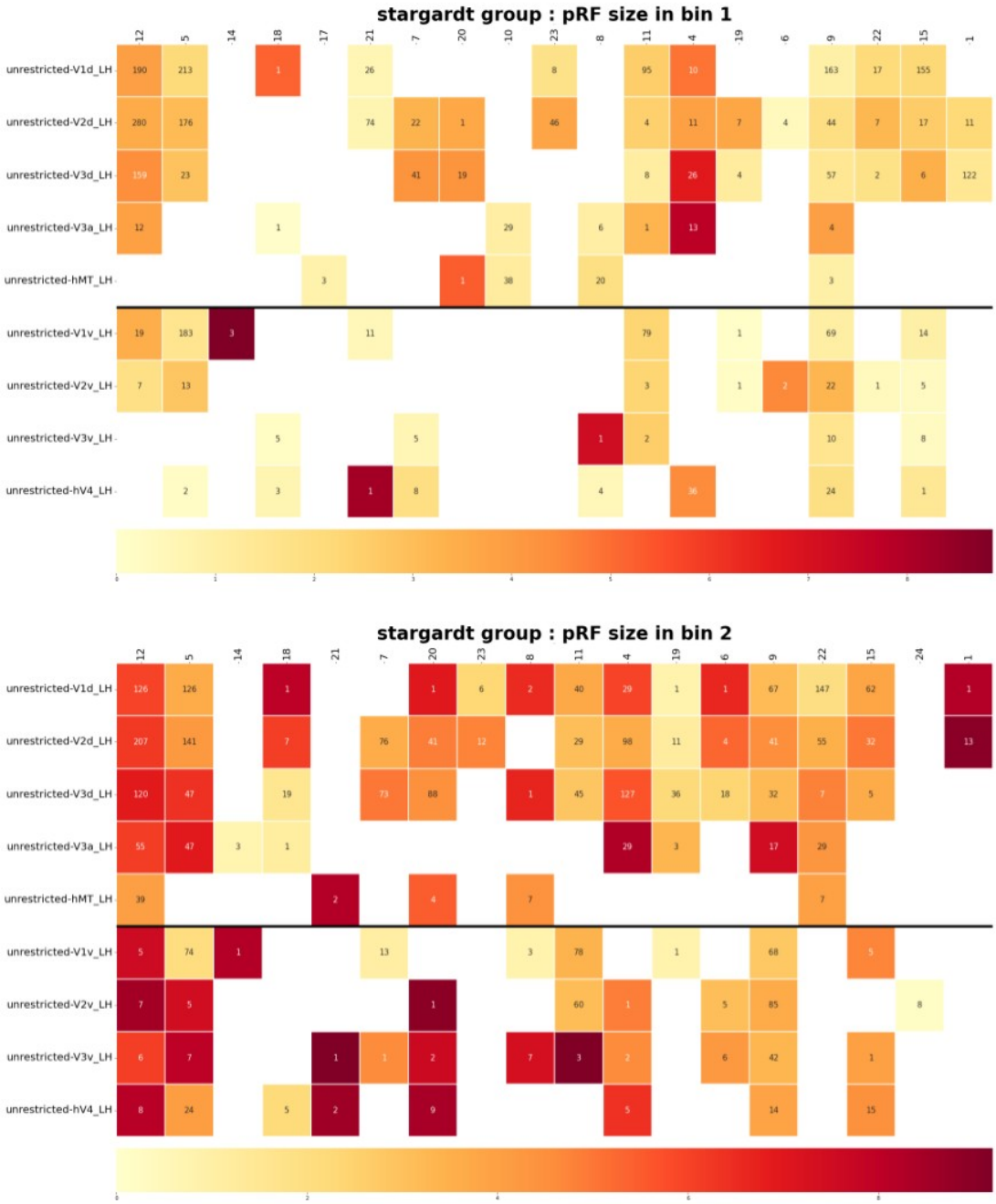

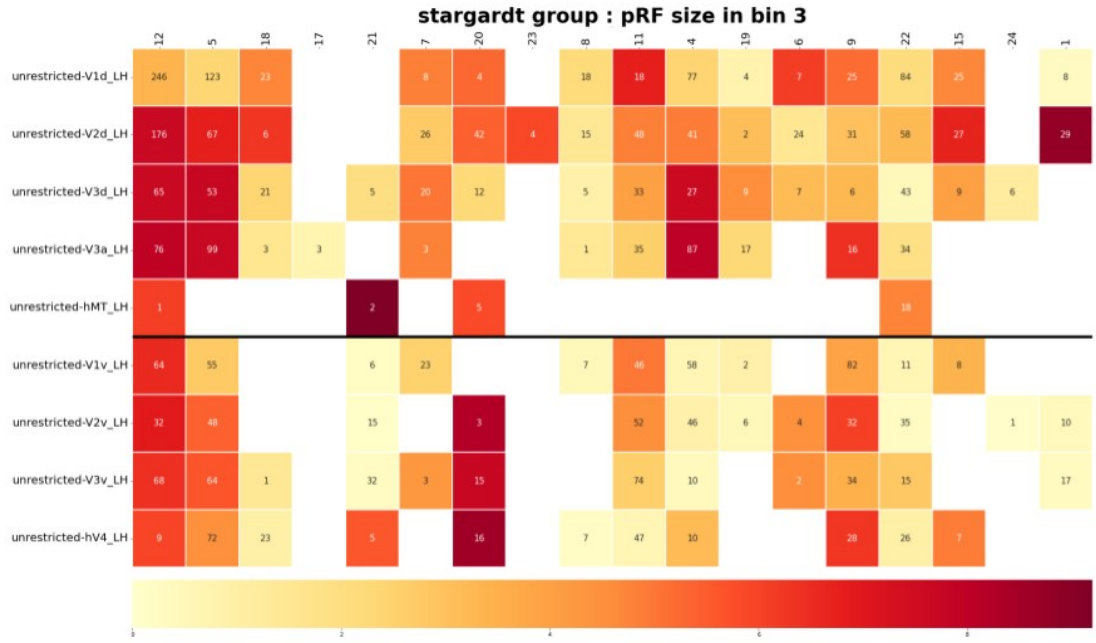

Heatmaps: individual number of voxel - Right hemisphere

Control group (n of voxels reported in cell)

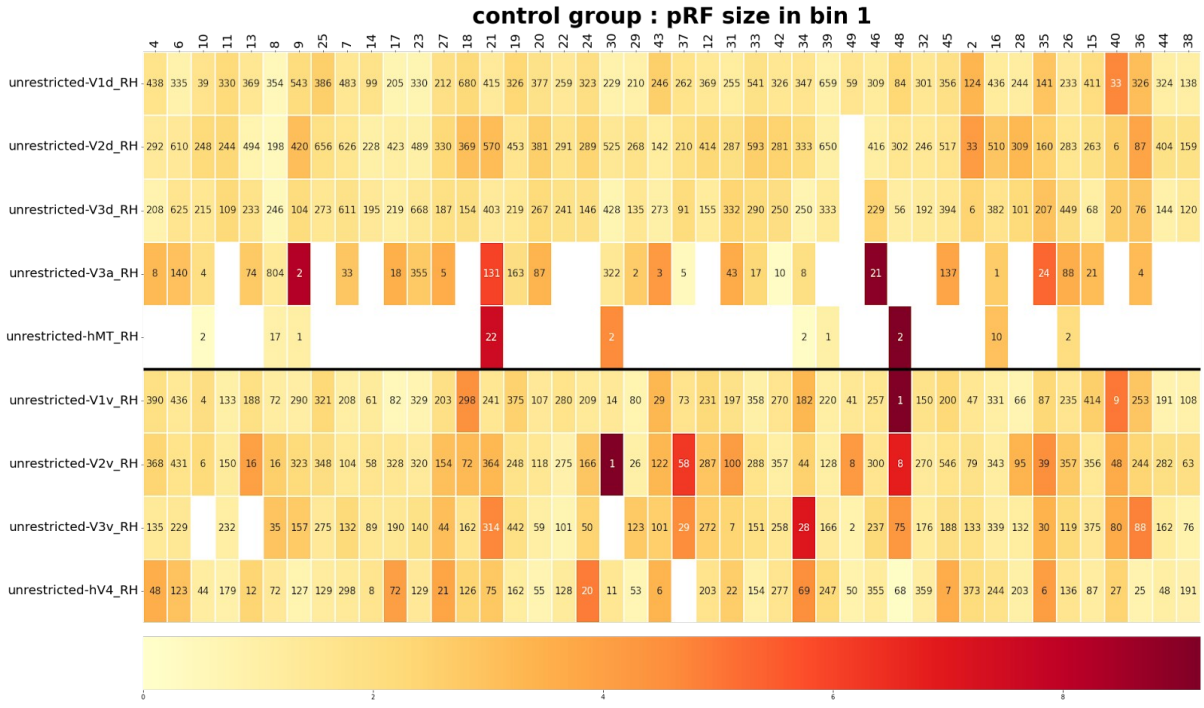

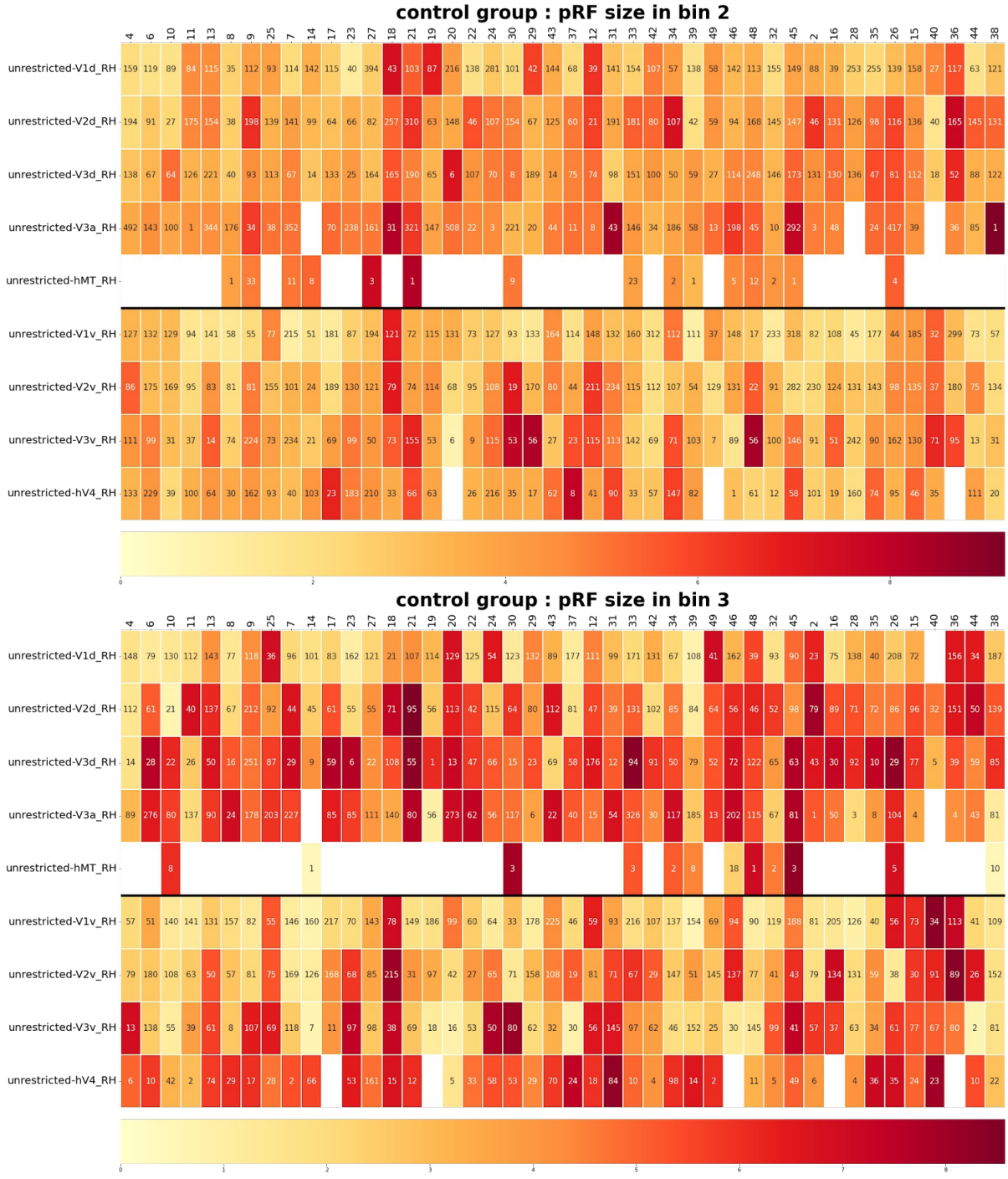

RP patients group (n of voxels reported in cell)

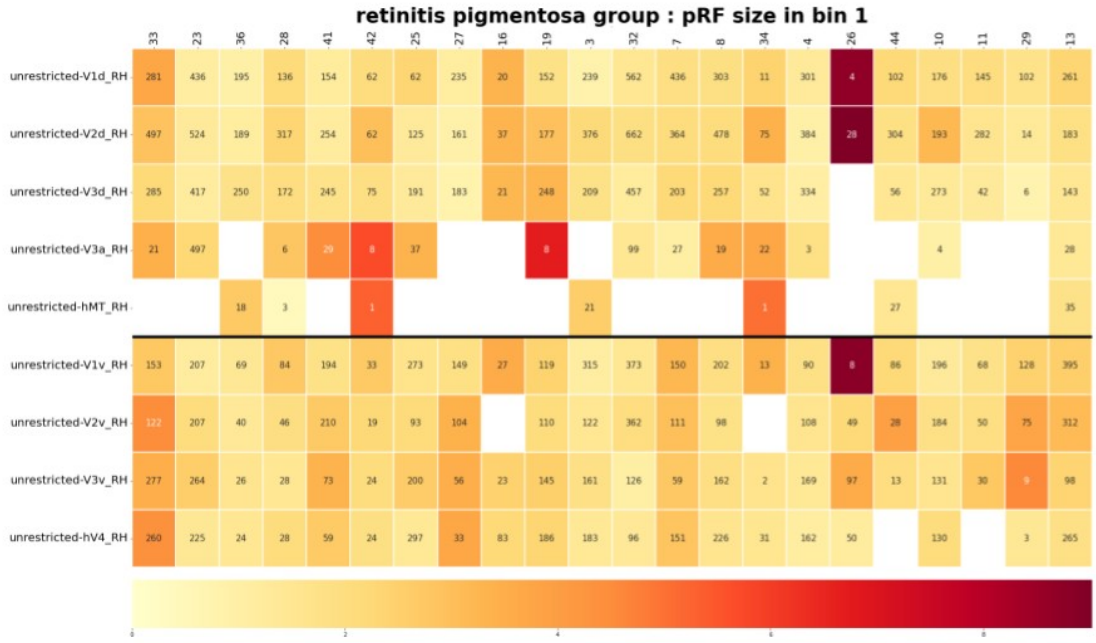

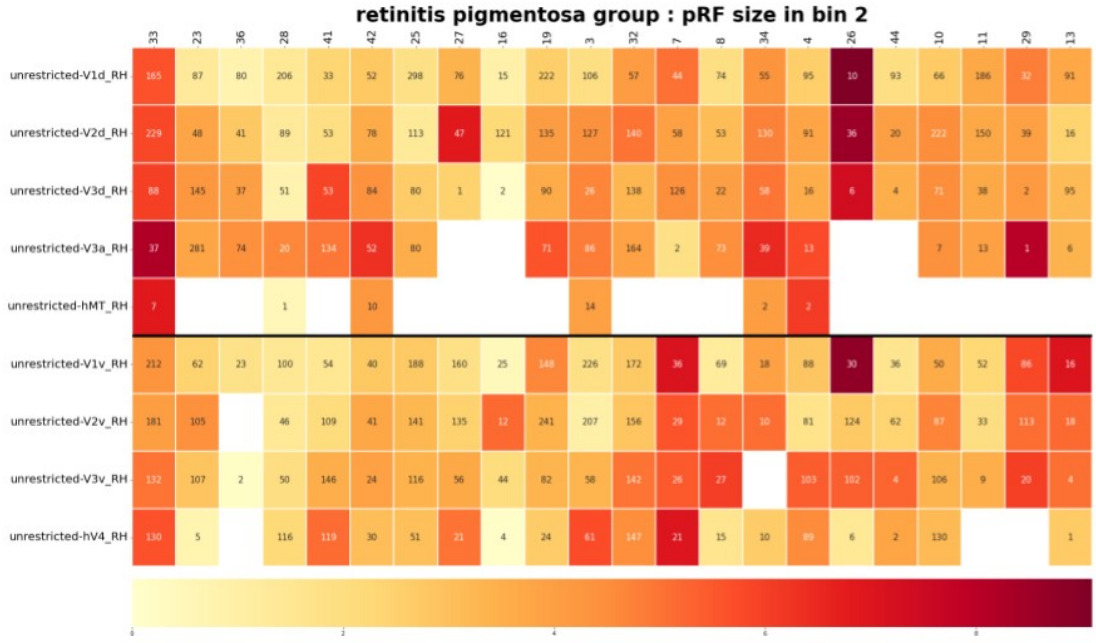

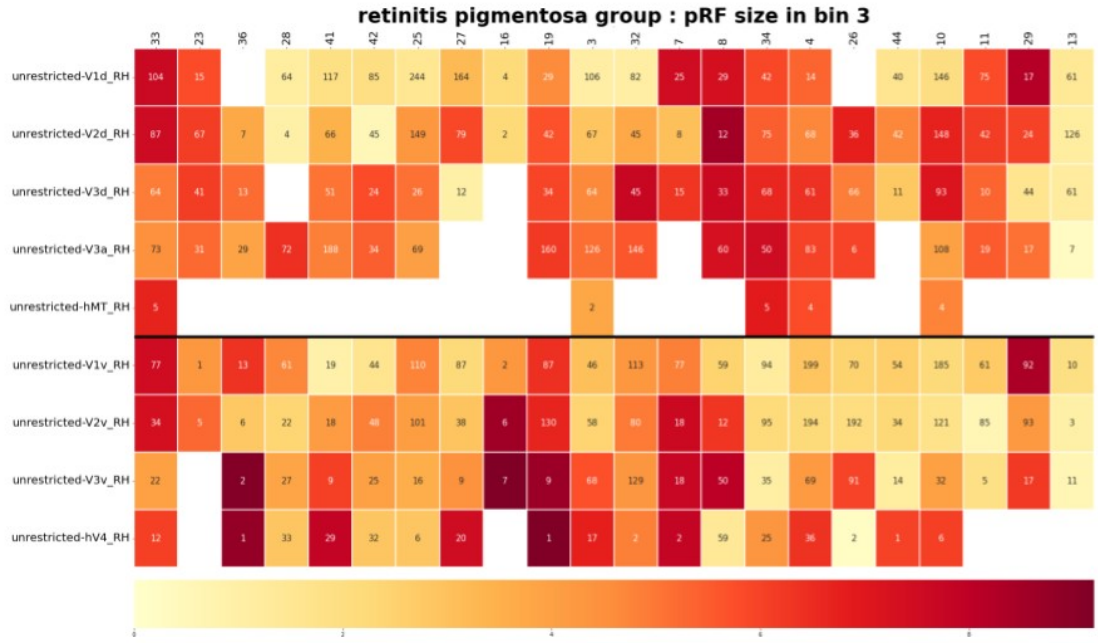

STGD patients group (n of voxels reported in cell)

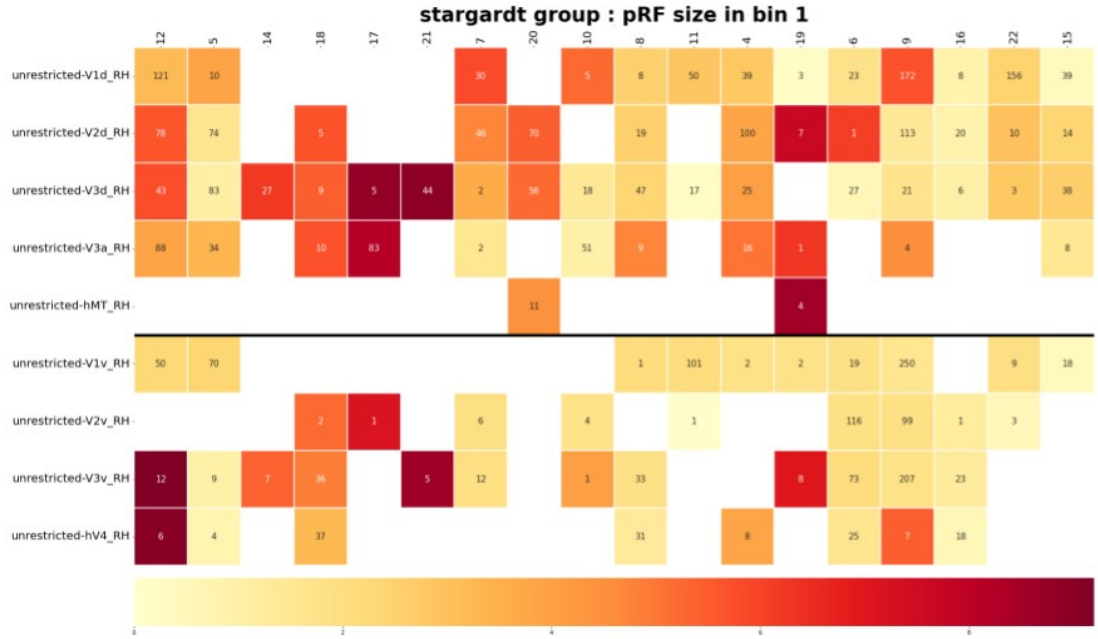

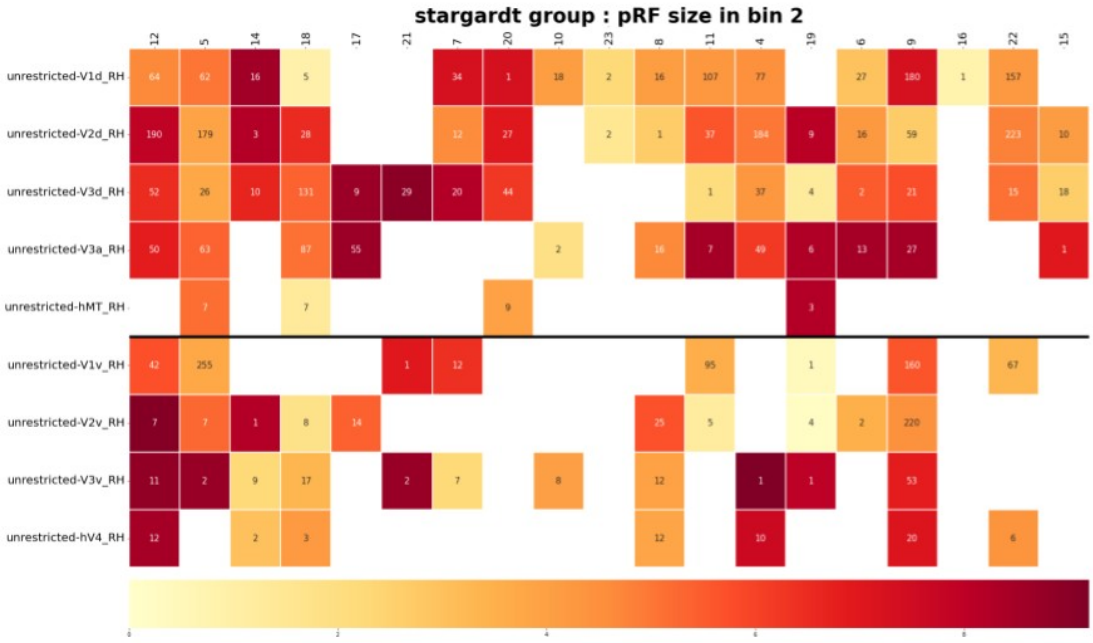

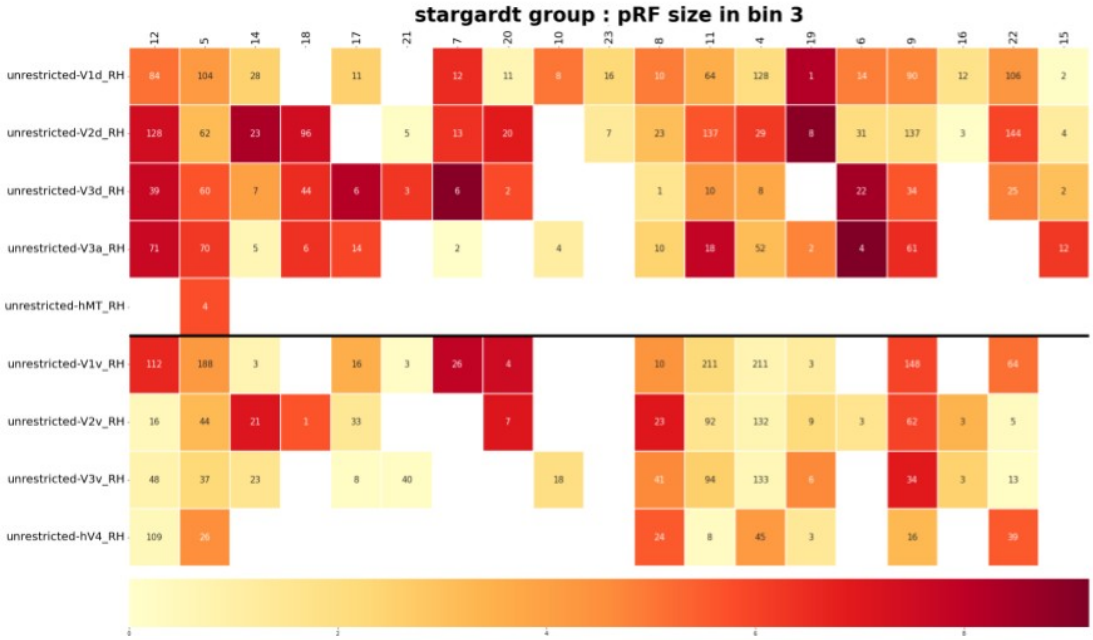

9.4. Hemispherical differences

During the analyses of our results, we found out that differences in pRF size between cohorts is often smaller than the difference between hemispheres within a cohort. Puzzled by this result, we checked significances of the pRF size within cohorts and we report results as follows:

LEFT VS RIGHT	V1	V2	V3
controls full	ns	p<0.001 left bigger	p<0.001 left bigger
controls limited	ns	p<0.001 left bigger	p<0.001 left bigger
RP	ns	p<0.001 left bigger	p<0.001 left bigger
STGD	p<0.001 right bigger	ns	ns

Note how the comparison within STGD patients group is outstandingly different from the results within the other cohorts, showing significantly bigger pRF size on the right hemisphere for V1.

We also performed analysis in most meaningful to our question central eccentricity bin. Separation of mean pRF data for only central eccentricity 1-3 visual degrees, as shown in the figure below lead to similar responses in left/right hemisphere dominance in RP and STDG patients, however different responses in ventral/dorsal subdivisions of analysed areas. Below we show the significant differences between dorsal and ventral pRF size in the 1-3 deg bin separately for each tested group and hemisphere. In the control group in full vision (A) we found increased pRF bilaterally in V3v compared to

V3d (left: p<0.001; right: p=0.000056), but no differences in dorsal and ventral V1 and V2. A similar pattern was found in controls with transient limited visual field (C), where pRF size increased bilaterally in V1v (left: p=0.000059; right: p<0.001) and in V3v (left: p<0.001; right: p=0.001539). Interestingly, in RP patients (D), we found a similar pattern as for the control group, with increased pRF size for right V2v and right V3v (p<0.001). Contrary to the other three groups, we found that in STGD patients (fB), pRF were increased in the right hemisphere for all the dorsal ROIs (all p<0.001).

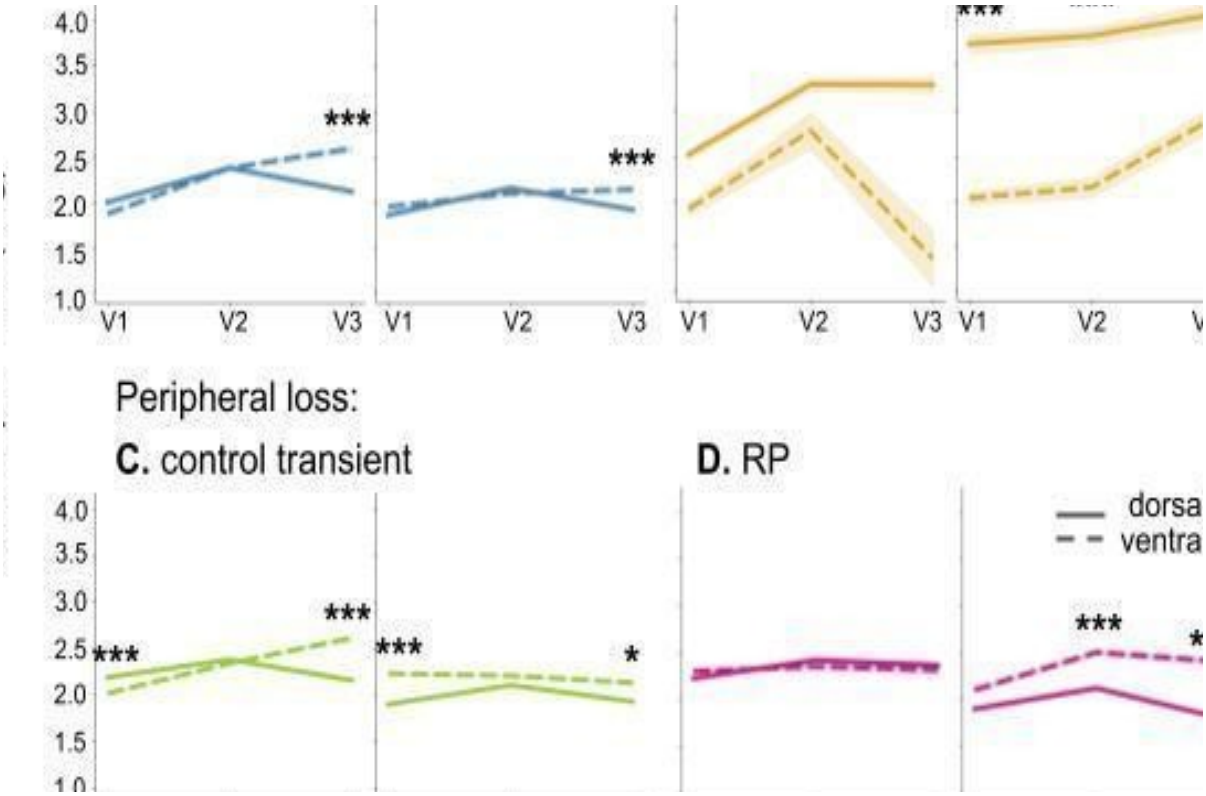

Dorsal-ventral pRF size differences for left and right hemispheres within central 1-3 deg eccentricity for V1, V2, V3 areas. (**A**) Controls; (**B**) Stargardt patients with central photoreceptor degeneration; (**C**) and (**D**) after peripheral loss: (C) transient in controls after mechanical removal by goggles and (D) Retinitis Pigmentosa patients with peripheral photoreceptor degeneration. Note the dorsal-ventral difference in pRF size after central loss in STGD patients where dorsal pRF were significantly larger than in ventral ROIs. In RP patients with peripheral loss, the central pRFs were increased. pRF size in dorsal ROIs (solid line), in ventral (dashed line). The vertical axis denotes the pRF

size in mean deg at central position (i.e., bin 1-3 deg). Means and standard errors (the width of the colored bands).

9.5. Motion-acuity task protocol

From a methodological point of view, while the pRF mapping procedure may have broader literature and an easier access to documentation, the proposed motion-acuity task is a novel technique that would require a more in detail explanation. For this reason, we recently published in the Journal of Visual Experiment (https://www.jove.com/; Ninghetto et al., 2024) a detailed methodological manuscript that illustrated step by step how to set up and run the novel protocol to investigate the visual acuity for centrally located shapes during peripheral stimulation.

The *setup* section explains how the environment should be organised to run the experiment in an ideal setting. It is also advised to use an eye tracker to keep track of eye movements during the entire duration of the task. In this section, moreover, the reader is informed where and how to download the software The software can be downloaded at (https://github.com/grimwj/Viscacha2). In the successive sections, it is explained how to run the actual test, with a particular stress on the stimuli definition. Tasks are explained for shapes defined by coherence of motion, direction of motion and velocity of motion of the RDK. Namely, in the coherence task, the circle and the ellipse consist of dots moving randomly with a velocity of 10°/s. The background is built of dots moving coherently upward with the same velocity as in the circle and ellipse. Similarly, in the direction task, the circle and the ellipse and the background are built of dots

moving at 10°/s, with the difference that here the dots in the background move all towards one direction. The velocity task involves three conditions. The circle and ellipse and the background consist of dots moving coherently upward, and dots within the circle and the ellipse always move slower than the background dots: i) 10°/s versus 20°/s; ii) 5°/s versus 10°/s; and iii) 1°/s versus 2°/s.

All the three tasks can be adjusted based on the specific aim of the protocol; all settings can be edited in the configuration file allowing the experimenters to modify velocity of the RDK, to use different colours or different target shapes and positions. A dedicated section illustrates how this motion-acuity test can be performed with the in-goggle condition and gives advice to maximize the outcome of the investigation with transient narrowing of the visual field.

To gain further insight on the data collected by this novel test in the manuscript we investigated whether the behavioral outcome from the motion-acuity task might be linked with the structural changes in the cortical structure of patient brains. We correlated motion-acuity tasks of RP and STGD patients with their individual fiber cross sections (FC), fiber density (FD) and their combined measure as fiber density cross section (FDC); in fixel-based analysis, FC quantifies the density and integrity of specific fiber tracts, while FD measures the number of fibers within a voxel, reflecting the compactness or concentration of fibers in that specific area. The FDC measure provides a combination of information about both the density of fibers within a voxel and the cross-sectional area of the fiber bundle. These parameters have been measured

as percentage of change from the control group, where the higher percentage meant the higher structural change.

Paired Pearson r correlations have been performed between each fixel based analysis measure (i.e., FC, FD, FDC) and percent of seen points in the Humphrey perimeter test.

The Humphrey full-field test values were deducted from both eyes, where each eye was shown with 120 points covering 60 degrees of visual field. The number of "seen points" was taken from the left and the right eye and summed together (max 240); the resulting value was calculated as a percentage from the 100%, representing the value when all 240 points were seen.

Similarly, we correlated the central Humphrey, taking into account only points seen within 10 degrees of visual field, for a maximum number of points equal to 32 (16 per eye; 100%).

We found a positive correlation for RP patients for FD and FDC with the full-field Humphrey ($r=0.5432$, $p=0.006$; $r=0.4555$, $p=0.025$) and only for FD with the central Humphrey ($r=0.4579$, $p=0.024$). We found a positive correlation for STGD patients for FDC with the full-field Humphrey ($r=0.5933$, $p=0.004$). Surprisingly, the results indicate that the higher percent of structural changes is linked with better performance in visual field examination and by this, we may hypothesize the existence of a dissociation between structural changes and behavioral visual performance. This hypothesis is supported by the found correlation with FD and central Humphrey only for RP patients, who lack peripheral vision. To validate our hypothesis, we performed a similar correlation but using the peripheral Humphrey, which takes all the seen points outside the 10 degrees landmark that we set for central, for the STGD patients, who

contrary from RP patients, did not show significance with central Humphrey; as expected, we found a significant correlation between peripheral Humphrey and FDC (r=0.6088, p=0.002). It is likely that there is a clear interplay between the structural changes and the visual field exploration as we reported significant correlations between structural parameters and central Humphrey for RP patients and peripheral Humphrey for STGD patients.

9.6. Structural changes in peripheral or central visual loss

Pearson r correlations were performed also for FD, FC and FDC compared to the motion-acuity threshold for RP and STGD patients. Some patients did not have enough data for a specific task of the motion-acuity test, for those cases we used pairwise deletion of missing data, by which the model did not include a patient when it had a missing value for one of the two compared variables, but it used the case when analyzing other variables with non-missing values.

Interestingly, for RP patients we found a negative significant correlation with the tasks in negative contrast for FC (mid velocity: r=-0.428, p=0.026; fast velocity: r=-0.4598, p=0.016), for FD (mid velocity: r=-0.3889, p=0.045), for FDC (mid velocity: r=-0.5505, p=0.003; fast velocity: r=-0.4538, p=0.017). The only exception was found for the easiest task - positive contrast at slow velocity - correlating with FC (r=-0.4523, p=0.014) and with FDC (r=-0.4506, p=0.014).

Contrary, for STGD, we found a negative significant correlation with the tasks in positive contrast for FC (fast velocity: r=-0.6916, p=0.013) and for FDC (slow velocity: r=-0.5921, p=0.016; mid velocity: r=-0.8092, p<0.001; fast velocity: r=-0.8498, p<0.001).

9.7. Supplementary Tables

9.7.1. Supplementary Table 1 Ophthalmological results and genetic findings of RP patients

ID	Sex	Age	Visual acuity (LogMAR)1	Humphrey 120 (points not seen)1	Average retinal thickness (□m)1	Status	NM accession	Gene**	Inheritance	Genomic notation allele 1 (hg19)	Allele 1 cDNA	Allele 1 protein	Allele 1 gnomAD-ALL AF	Allele 1 Franklin ACMG classification	Genomic notation allele 2 (hg19)	Allele 2 cDNA	Allele 2 protein	Allele 2 gnomAD-ALL AF	Allele 2 Franklin ACMG classification
79	F	43	0.0 / 0.0	3 / 6	125 / 288	Very likely solved	NM_000539.3	*RHO*	*AD*	chr3:129247845G>A	c.269G>A	p.(Gly90Asp)	0%	Pathogenic		=	=		

151	F	28	0.3 / 0.3	0% / 33% 2	291 / 379	Very likely solved	NM_000539.3	*RHO*	*AD*	chr3:129249760C>T	c.403C>T	p.(Arg135Trp)	0%	Pathogenic		=	=		
291	M	45	0.1 / 0.1	36 / 35	193 / 199	Possibly solved	NM_000283.4	*PDE6B*	*AR*	chr4:65008 4A>G	c.1107+3A>G	p.(?)	0.0042%	Likely pathogenic	chr4:661679T>C	c.2387T>C	p.(Met796Thr)	0.0020%	VUS
368	M	37	0.7 / 0.3	120 / 119	184 / 165	Possibly solved	NM_016247.4	*IMPG2*	*AR*	chr3:100988356T>C	c.887+3A>G	p.(?)	0%	VUS	chr3:100988356T>C	c.887+3A>G	p.(?)	0%	VUS
372	F	36	0.22 / 0.4	80 / 90	303 / 299	Very likely solved	NM_206933.4	*USH2A*	*AR*	chr1:216420126G>T	c.2610C>A	p.(Cys870*)	0.0014%	Pathogenic	chr1-215955392T>G	c.10732A>C	p.(Ser3578Arg)	0%	VUS
419	M	48	0.3 / 0.3	103 / 112	269 / 246	Very likely solved	NM_000390.4	*CHM*	*XL*	chrX:85212923G>A	c.877C>T	p.(Arg293*)	0%	Pathogenic		Y	Y		
427	M	44	1.7 / 1.52	111 / 120	202 / 261	Very likel	NM_001	*RPGR*	*XL*	chrX:381	c.2236_2	p.(Glu	0%	Pathogen		Y	Y		

						y solved	034853.2			460188_38146019del	237del	746 Argfs*23)		ic				
479	M	32	0.3 / 0.3	110 / 112	152 / 181	Possibly solved	NM_206933.4	*USH2A*	*AR*	chr1:216595380A>C	c.299T>G	p.(Leu100Arg)	0%	VUS	chr1:216390902A>C	c.2994-10T>G	p.(?)	0.00040%	VUS
489	F	62	0.4 / 0.4	117 / 99	188 / 272	Very likely solved	NM_000322.5	*PRPH2*	*AR*	chr6:42666246C>T	c.829-1G>A	p.(?)	0%	Likely pathogenic		=	=		
615	F	38	0.5 / 0.6	102 / 106	422 / 269	Very likely solved	NM_206933.4	*USH2A*	*AR*	chr1:216420126G>T	c.2610C>A	p.(Cys870*)	0.0014%	Pathogenic	chr1-215955392T>G	c.10732A>C	p.(Ser3578Arg)	0%	VUS
1031	F	38	0.0 / 0.0	55 / 34	218 / 226	Very likely solved	NM_206933.4	*USH2A*	*AR*	chr1:216465543C>T	c.1814G>A	p.(Cys605Tyr)	0%	VUS	chr1:215933187T>C	c.11048-2A>G	p.(?)	0.00040%	Pathogenic
1066	M	57	0.15	77 /	395 /	Very likel	NM_014	*NR2*	*AR*	chr15:72	c.227G>	p.(Arg	0.02	Likely	chr15:72	c.227G>	p.(Arg	0.02	Likely

			/ 0.1	76	315	y solved	249.4	*E3*		103931G>A	A	76Gln)	1%	pathogenic	103931G>A	A	76Gln)	1%	pathogenic
1439	F	35	0.22 / 0.3	65 / 83	211 / 159	Very likely solved	NM_015629.4	*PRPF31*	*AD*	chr19:54625900del/chr19-54625899GA>G	c.347del	p.(Asp116Valfs*82)	0%	Likely pathogenic		=	=		
131	F	43	0.6 / 0.3	33% / 0%2	255 / 319	Unsolved													
292	F	41	0.8 / 0.1	111 / 109	149 / 197	Unsolved													
518	F	53	0.1 / 0.0	50 / 45	253 / 235	Unsolved													
732	F	53	0.3 / 0.22	112 / 111	228 / 237	Unsolved													

1360	F	46	0.9 / 1.0	23 / 87	298 / 286	Unsolved												
1408	F	49	0.22 / 0.3	- / -	302 / 298	Unsolved												
1423	F	45	0.3 / 0.5	105 / 96	184 / 180	Unsolved												
1426	F	52	0.8 / 0.8	109 / 114	141 / 135	Unsolved												
1438	M	42	0.7 / 0.3	113 / 114	215 / 355	Unsolved												
1478	M	46	1.3 / 1.3	77 / 68	320 / 261	Unsolved												

*The final diagnosis was established after typical ophthalmological examination and after accessory investigations, as OCT (optical coherence tomography), FA (fluorescein angiography) and electrophysiological testing (flash electroretinography, FERG)

**Data analysis was performed using the guidelines described in methods, after which probands obtained a label of “very likely” or “possibly solved” (Panneman et al., 2023)

1 Results are shown for left and right eyes, respectively

2 Results from Central 24-2 Threshold Test

AR: autosomal recessive, AD: autosomal dominant, XL: X-linked, AF: allele frequency, Y: Y chromosome, “=”: Allele 2 not changed

9.7.2. Supplementary Table 2 Ophthalmological results and genetic findings of STGD patients

ID	Sex	Age	Visual acuity (LogMAR)1	Humphrey 120 (points not seen) 1	Average retinal thickness (□m)1	Status	NM accession	Gene**	Inheritance	Genomic notation allele 1 (hg19)	Allele 1 cDNA	Allele 1 protein	Allele 1 gnomAD-ALL AF	Allele 1 Franklin ACMG classification	Genomic notation allele 2 (hg19)	Allele 2 cDNA	Allele 2 protein	Allele 2 gnomAD-ALL AF	Allele 2 Franklin ACMG classification

													on					
20	F	32	1.3 / 1.3	52 / 522	57 / 52	Solved	NM_000350.3	*ABCA4*	*AR*	chr1:94528806A>G, chr1:94508969G>A	c.[1622T>C;3113C>T]	p.[(Leu541Pro;Ala1038Val)]	0.0163%, 0.17555%	Pathogenic	chr1-94517254C>G, chr1-94476467T>A	c.2588G>C(;)5603A>T	p.[Gly863Ala,Gly863del](;)(Asn1868Ile)	0.4295%, 4.2191%	Pathogenic
47	F	41	0.5 / 0.5	13 / 15	72 / 90	Solved	NM_000350.3	*ABCA4*	*AR*	chr1:94473807C>T	c.5882G>A	p.(Gly1961Glu)	0.4564%	Pathogenic	chr1-94476951A>G, chr1-94476467T>A	c.[5461-10T>C;5603A>T]	p.[Thr1821Aspfs*6,Thr1821Valfs*13;(Asn18	0.022%, 4.2191%	Pathogenic

																68Ile)]		
146	F	39	0.7 / 0.7	7 / 10	214 / 177	Solved	NM_000350.3	*ABCA4*	*AR*	chr1:94568687G>A	c.4544C>T	p.(Arg1512*)	0.0016%	Pathogenic	chr1-94466425C>A	c.6446G>T	p.(Arg2149Leu)	0.0032%	Pathogenic
214	F	48	1.0 / 1.0	48 / 70	195 / 210	Solved	NM_000350.3	*ABCA4*	*AR*	chr1:94528806A>G,chr1:94508969G>A	c.[1622T>C;3113C>T]	p.[(Leu541Pro;Ala1038Val)]	0.0163%,0.1755%	Pathogenic	chr1-94473856G>T	c.5836-3C>A	p.(Lys1945_Ile1946Phelns10)	0%	Likely pathogenic
252	F	64	1.0 / 0.4	18 /	193 / 209	So	N	*A*	*A*	ch	c.5	p.	0.4	Pa	chr1-	c.28	p.	0.0032	Pathogenic

				13		lved	M_000350.3	*BCA4*	*R*	r1:94473807C>T	882G>A	(Gly1961Glu)	564%	thogenic	94512518T>C	75A>G	(Thr959Ala)	%	
401	M	30	0.9 / 1.0	32 / 87	194 / 215	Solved	NM_000350.3	*ABCA4*	*AR*	chr1:94528068A>G, chr1:94508969G>A	c.[1622T>C;3113C>T]	p.[(Leu541Pro;Ala1038Val)]	0.0163%, 0.1755%	Pathogenic	chr1-94528680T>A	c.1748A>T	p.(Lys583Met)	0%	Likely pathogenic
414	M	42	1.3 / 1.3	66 / 57	183 / 167	Solved	NM_000350.3	*ABCA4*	*AR*	chr1:94496571	c.4234C>T	p.(Gln1412*)	0.0007%	Pathogenic	chr1:94564484G>A	c.634C>T	p.(Arg212Cys)	0.0107%	Pathogenic

										G > A								
444	M	40	1.0 / 0.9	7 / 3	96 / 183	Solved	NM_000350.3	*ABCA4*	*AR*	chr1:94528806A>G, chr1:94508969G>A	c.[1622T>C;3113C>T]	p.[(Leu541Pro;Ala1038Val)]	0.0163 %, 0.1755 %	Pathogenic	chr1:94473807C>T	c.5882G>A	p.(Gly1961Glu)	0.4564 %	Pathogenic
449	F	24	1.0 / 1.0	60 / 79	289 / 175	Solved	NM_000350.3	*ABCA4*	*AR*	chr1:94528806A>G, chr1:94508969G>A	c.[1622T>C;3113C>T]	p.[(Leu541Pro;Ala1038Val)]	0.0163 %, 0.1755 %	Pathogenic	chr1:94528806A>G, chr1:94508969G>A	c.[1622T>C;3113C>T]	p.[(Leu541Pro;Ala1038Val)]	0.0163 %, 0.1755 %	Pathogenic

										:94508969G>A		al)]						
455	F	40	1.3 / 1.3	56 / 56	182 / 220	Solved	NM_000350.3	*ABCA4*	*AR*	chr1:94485137C>T	c.5196+1G>A	p.(?)	0.002%	Pathogenic	chr1-94520793A>G	c.2461T>C	p.(Trp821Arg)	0%	Pathogenic
476	F	45	1.0 / 1.0	14 / 11	197 / 191	Solved	NM_000350.3	*ABCA4*	*AR*	chr1:94528806A>G,chr1:94508969G	c.[1622T>C;3113C>T]	p.[(Leu541Pro;Ala1038Val)]	0.0163%,0.1755%	Pathogenic	chr1-94517254C>G,chr1-94476467T>A	c.2588G>C(;)5603A>T	p.[Gly863Ala,Gly863del](;)(Asn1868Ile)	0.4295%,4.2191%	Pathogenic

										> A								
576	F	20	1.3 / 1.7	87 / 37	145 / 207	Solved	NM_000350.3	*ABCA4*	*AR*	chr1:94481294C>T	c.5312+1G>A	p.(?)	0.0004%	Pathogenic	chr1-94486942 C>T	c.4872 G>A	p.(Trp1624*)	0%	Pathogenic
638	F	19	0.5 / 0.5	4 / 2	275 / 250	Solved	NM_000350.3	*ABCA4*	*AR*	chr1:94568687 G>A	c.454 C>T	p.(Arg152*)	0.0016%	Pathogenic	chr1-94476351 C>T	c.5714+5G>A	p.[=,Glu1863Leufs*33]	0.0297%	Pathogenic
666	F	60	1.7 / 0.0	0% / 0%3	361 / 138	Solved	NM_000350.3	*ABCA4*	*AR*	chr1:94564484 G>A	c.634 C>T	p.(Arg212Cys)	0.0107%	Pathogenic	chr1-94490606 T>C	c.4540-2A>G	p.(?)	0.0004%	Pathogenic
669	F	34	1.3 / 1.3	48 /	221 / 188	So	N	*A*	*A*	ch	c.6	p.	0.0	Pa	chr1-	c.88	p.	0%	Likely

										r1:94564484G>A	34C>T	(Arg212Cys)	107%		94546243AG>A	9del	(Leu297Cysfs*3)		pathogenic
				60		lved	M_000350.3	*BCA4*	*R*					thogenic				
710	F	25	1.3 / 1.3	63 / 59	245 / 293	Solved	NM_000350.3	*ABCA4*	*AR*	chr1:94528806A>G, chr1:94508969G>A	c.[1622T>C;3113C>T]	p.[(Leu541Pro;Ala1038Val)]	0.0163%, 0.17555%	Pathogenic				
804	F	27	1.3 / 1.3	54 / 58	173 / 149	Solved	NM_000350.3	*ABCA4*	*AR*	chr1:94578524C>G	c.160+5G>C	p.(?)	0%	Likely pathogenic				

										4C>G	>C			enic					
1202a	M	45	0.6 / 0.1	23 / 21	299 / 197	Solved	NM_000322.5	*PRPH2*	*AD*	chr6:42689558C>T	c.515G>A	p.(Arg172Gln)	0.0004 %	Pathogenic		=	=		
1260b	F	48	0.8 / 0.8	65 / 48	270 / 270	Solved	NM_000350.3	*ABCA4*	*AR*	chr1:94544199CT>C	c.1302del	p.(Gln437Argfs*12)	0.0004 %	Pathogenic	chr1:94473807C>T	c.5882G>A	p.(Gly1961Glu)	0.4564 %	Pathogenic
1395c	M	20	0.4 / 0.4	9 / 5	138 / 139	Solved	NM_000350.3	*ABCA4*	*AR*	chr1:94568687G>A	c.454C>T	p.(Arg152*)	0.0016 %	Pathogenic	chr1-94517254C>G, chr1-94476467T>A	c.2588G>C(;)5603A>T	p.[Gly863Ala,Gly863del](;)(Asn1868Il	0.4295 %, 4.2191 %	Pathogenic

																e)		
186	**M**	**54**	**1.3 / 1.0**	**27 / 34**	**208 / 200**	**Unsolved**												

*The final diagnosis was established after typical ophthalmological examination and after accessory investigations, as OCT (optical coherence tomography), FA (fluorescein angiography) and electrophysiological testing (flash electroretinography, FERG)

**Data analysis was performed using the guidelines described in methods, after which probands obtained a label of “very likely” or “possibly solved” (Panneman et al., 2023)

1 Results are shown for left and right eyes, respectively

2 Results from Central 24-2 Threshold Test

3 Results from N-30-5 FDT Perimetry Screening; reported here is the percent of fixation errors

a Corradi et al., unpublished data

b Khan et al., 2020 PMID: 32307445

c Hitti-Malin et al., 2022 PMID: 36259723; Hitti-Malin et al., unpublished data

AR: autosomal recessive, AD: autosomal dominant, XL: X-linked, AF: allele frequency, Y: Y chromosome, "=": Allele 2 not changed

9.7.3. Supplementary Table 3 Descriptive Statistics for pRF size

bin	vision condition	group	ROI	hemisphere	stream	N	Mean	Std.Dev.	Std.Err	-95.00%	+95.00%
1-3	unrestricted	controls	V1	left	ventral	10727	1.86843553	1.29981418	0.0125499538	1.8438353	1.89303576
1-3	unrestricted	controls	V1	right	dorsal	10985	1.85773937	1.3175416	0.0125708402	1.83309826	1.88238048
1-3	unrestricted	controls	V1	right	ventral	7122	1.95030926	1.532454	0.0181587714	1.91471267	1.98590585
1-3	unrestricted	controls	V2	left	dorsal	8994	2.37770129	1.58725856	0.0167367542	2.34489344	2.41050914
1-3	unrestricted	controls	V2	left	ventral	8251	2.3759442	1.63936001	0.0180476659	2.34056624	2.41132217
1-3	unrestricted	controls	V2	right	dorsal	12219	2.15644609	1.49028036	0.0134818703	2.1300195	2.18287269

1-3	unrestricted	controls	V2	right	ventral	7577	2.09472915	1.57504361	0.0180943896	2.05925913	2.13019917
1-3	unrestricted	controls	V3	left	dorsal	6404	2.11632325	1.52773095	0.0190906719	2.07889914	2.15374735
1-3	unrestricted	controls	V3	left	ventral	4135	2.59419039	1.77232174	0.0275616243	2.54015478	2.648226
1-3	unrestricted	controls	V3	right	dorsal	7651	1.91435801	1.18231267	0.01351678	1.88786141	1.9408546
1-3	unrestricted	controls	V3	right	ventral	5353	2.14196069	1.78189217	0.0243547007	2.09421556	2.18970582
1-3	unrestricted	rp	V3	left	dorsal	2152	2.36113891	1.61502567	0.0348143503	2.29286562	2.4294122
1-3	unrestricted	rp	V3	right	dorsal	3381	1.79722268	0.964453402	0.0165866494	1.7647018	1.82974356
1-3	unrestricted	rp	V3	left	ventral	1662	2.31114218	1.5626215	0.0383299528	2.23596207	2.38632229
1-3	unrestricted	rp	V3	right	ventral	2018	2.40116248	1.41875143	0.0315824437	2.33922486	2.4631001
1-3	unrestricted	rp	V2	left	dorsal	2843	2.41602181	1.37083046	0.0257095998	2.36561045	2.46643317
1-3	unrestricted	rp	V2	right	dorsal	4858	2.11453445	1.33218986	0.0191133745	2.0770635	2.15200532

										9	
1-3	unrestricted	rp	V2	left	ventral	3553	2.34767404	1.51541252	0.0254233787	2.29782815	2.39751993
1-3	unrestricted	rp	V2	right	ventral	2296	2.50077321	1.49128035	0.0311224195	2.4397422	2.56180422
1-3	unrestricted	rp	V1	left	dorsal	3453	2.22160121	1.44472528	0.0245859494	2.17339673	2.26980568
1-3	unrestricted	rp	V1	right	dorsal	3699	1.8909943	1.17972256	0.0193971409	1.85296416	1.92902444
1-3	unrestricted	rp	V1	left	ventral	4229	2.2962625	1.45551976	0.0223820192	2.25238198	2.34014301
1-3	unrestricted	rp	V1	right	ventral	2841	2.0955768	1.47579104	0.0276878512	2.04128647	2.14986713
1-3	unrestricted	stgd	V1	left	dorsal	721	2.50780997	1.48453353	0.0552869178	2.39926714	2.6163528
1-3	unrestricted	stgd	V1	right	dorsal	558	3.73245148	2.7045692	0.114493544	3.50755959	3.95734338
1-3	unrestricted	stgd	V1	left	ventral	299	1.9044505	1.27933636	0.0739859322	1.7588494	2.05005159
1-3	unrestricted	stgd	V1	right	ventral	436	2.02900827	1.57242205	0.0753053586	1.88100067	2.17701586

1-3	unrestricted	stgd	V2	left	dorsal	504	3.28510856	1.61015076	0.0717218152	3.14419733	3.4260198
1-3	unrestricted	stgd	V2	right	dorsal	473	3.82304353	2.07268057	0.095301954	3.63577493	4.01031212
1-3	unrestricted	stgd	V2	left	ventral	48	2.77431034	1.41747295	0.204594598	2.3627191	3.18590158
1-3	unrestricted	stgd	V2	right	ventral	188	2.14646257	1.52053663	0.110896531	1.92769354	2.3652316
1-3	unrestricted	stgd	V3	left	dorsal	418	3.27944777	1.84583079	0.0902825351	3.10198217	3.45691336
1-3	unrestricted	stgd	V3	right	dorsal	388	4.05639594	2.76660333	0.140453004	3.78024949	4.33254238
1-3	unrestricted	stgd	V3	left	ventral	24	1.3594526	1.48569339	0.303265894	0.7320993	1.9868059
1-3	unrestricted	stgd	V3	right	ventral	307	2.91495186	2.37578168	0.135593023	2.64813913	3.18176458
3-6	unrestricted	controls	V1	left	dorsal	6298	3.12699445	2.25981254	0.0284754821	3.0711728	3.18281609
3-6	unrestricted	controls	V1	left	ventral	5922	2.88592487	2.21163984	0.0287395658	2.82958484	2.9422649
3-6	unrestricted	contro	V1	right	dorsal	5347	3.24263383	2.38539452	0.03262159	3.1786822	3.30658545

		ls								1	
3-6	unrestricted	controls	V1	right	ventral	5514	2.76557299	2.27557063	0.0306448105	2.70549707	2.8256489
3-6	unrestricted	controls	V2	left	dorsal	5628	4.4966149	2.41282591	0.0321624366	4.43356412	4.55966568
3-6	unrestricted	controls	V2	left	ventral	5529	4.21066222	2.53245133	0.0340578958	4.14389536	4.27742909
3-6	unrestricted	controls	V2	right	dorsal	5174	4.66914799	2.30771844	0.0320826038	4.60625253	4.73204345
3-6	unrestricted	controls	V2	right	ventral	5116	3.50501062	2.37844668	0.0332527947	3.43982091	3.57020032
3-6	unrestricted	controls	V3	left	dorsal	4956	4.62601287	2.01750882	0.0286582583	4.56982999	4.68219574
3-6	unrestricted	controls	V3	left	ventral	3045	5.17917617	1.96234866	0.0355617009	5.10944879	5.24890355
3-6	unrestricted	controls	V3	right	dorsal	4311	4.21060368	1.67330888	0.0254851447	4.16063968	4.26056768
3-6	unrestricted	controls	V3	right	ventral	3693	4.40238334	2.38512489	0.039248356	4.32543275	4.47933394
3-6	unrestricted	rp	V3	left	dorsal	1965	4.62493991	1.96355198	0.0442956547	4.5380684	4.71181133

										8	
3-6	unrestricted	rp	V3	right	dorsal	1233	4.01949087	1.81667553	0.0517363551	3.91798976	4.12099197
3-6	unrestricted	rp	V3	left	ventral	992	4.71967728	2.38754673	0.0758046845	4.57092115	4.86843341
3-6	unrestricted	rp	V3	right	ventral	1360	4.04418035	2.41428303	0.0654664403	3.91575411	4.17260659
3-6	unrestricted	rp	V2	left	dorsal	1853	3.85972447	2.1981408	0.0510643488	3.75957474	3.95987421
3-6	unrestricted	rp	V2	right	dorsal	2036	4.01086533	2.39261844	0.0530254739	3.90687546	4.1148552
3-6	unrestricted	rp	V2	left	ventral	1884	4.09153867	2.71301692	0.0625046104	3.96895309	4.21412425
3-6	unrestricted	rp	V2	right	ventral	1943	3.08626065	2.4028953	0.0545127947	2.97935091	3.1931704
3-6	unrestricted	rp	V1	left	dorsal	2647	2.93846709	2.45797167	0.0477749127	2.84478713	3.03214705
3-6	unrestricted	rp	V1	right	dorsal	2143	2.76101203	2.32762139	0.050280693	2.66240796	2.85961609
3-6	unrestricted	rp	V1	left	ventral	2499	2.81729304	2.18036417	0.0436160075	2.7317657	2.90282028

										9	
3-6	unrestricted	rp	V1	right	ventral	1891	3.02627368	2.59022541	0.0595650891	2.90945344	3.14309392
3-6	unrestricted	stgd	V1	left	dorsal	610	3.84098264	1.96924679	0.0797324721	3.68439867	3.99756661
3-6	unrestricted	stgd	V1	right	dorsal	767	5.21667289	2.54866603	0.0920269965	5.03601784	5.39732794
3-6	unrestricted	stgd	V1	left	ventral	248	2.78784886	1.58202603	0.100458753	2.58998382	2.9857139
3-6	unrestricted	stgd	V1	right	ventral	633	4.3236466	2.22639095	0.0884910957	4.14987445	4.49741875
3-6	unrestricted	stgd	V2	left	dorsal	767	4.6825566	2.03053082	0.0733182183	4.53862812	4.82648509
3-6	unrestricted	stgd	V2	right	dorsal	980	5.29487063	2.08660471	0.0666541425	5.1640692	5.42567206
3-6	unrestricted	stgd	V2	left	ventral	172	3.66156051	1.77558729	0.135387262	3.39431499	3.92880602
3-6	unrestricted	stgd	V2	right	ventral	293	4.53548863	3.11124377	0.181760802	4.17776131	4.89321596
3-6	unrestricted	stgd	V3	left	dorsal	618	4.92091673	2.1918495	0.0881691172	4.7477687	5.09406468

										9	
3-6	unrestricted	stgd	V3	right	dorsal	419	5.73690242	1.99370387	0.0973988077	5.54544992	5.92835492
3-6	unrestricted	stgd	V3	left	ventral	78	4.86044522	2.20891583	0.250110467	4.36241166	5.35847879
3-6	unrestricted	stgd	V3	right	ventral	123	5.56169109	2.76975611	0.249740498	5.06730483	6.05607734
6-9	unrestricted	controls	V1	left	dorsal	4598	3.0494293	3.13932979	0.0462969582	2.95866503	3.14019357
6-9	unrestricted	controls	V1	left	ventral	4248	2.77628757	3.10753415	0.0476786177	2.68281255	2.86976258
6-9	unrestricted	controls	V1	right	dorsal	4522	2.98692517	3.24904026	0.048315871	2.89220244	3.08164789
6-9	unrestricted	controls	V1	right	ventral	4872	2.57891647	3.03493671	0.0434806471	2.49367478	2.66415815
6-9	unrestricted	controls	V2	left	dorsal	3733	4.67371555	3.56197936	0.0582991742	4.5594142	4.7880169
6-9	unrestricted	controls	V2	left	ventral	3362	4.76238937	3.54351869	0.0611133194	4.64256632	4.88221243
6-9	unrestricted	contro	V2	right	dorsal	3500	4.85731777	3.47582195	0.0587521141	4.7421259	4.97250965

		ls									
6-9	unrestricted	controls	V2	right	ventral	3860	3.84264616	3.38792521	0.0545305857	3.73573464	3.94955767
6-9	unrestricted	controls	V3	left	dorsal	3061	5.63293703	3.07862886	0.0556449391	5.5238318	5.74204226
6-9	unrestricted	controls	V3	left	ventral	1887	5.10871626	3.29534026	0.0758602578	4.95993741	5.25749512
6-9	unrestricted	controls	V3	right	dorsal	2419	5.75221406	2.46500905	0.0501187907	5.65393384	5.85049428
6-9	unrestricted	controls	V3	right	ventral	2726	4.13840728	3.2951365	0.063111788	4.01465548	4.26215908
6-9	unrestricted	rp	V3	left	dorsal	1161	5.32872158	2.75203615	0.0807677574	5.17025434	5.48718882
6-9	unrestricted	rp	V3	right	dorsal	836	5.28452411	3.02201376	0.104518531	5.07937419	5.48967404
6-9	unrestricted	rp	V3	left	ventral	950	4.82348667	3.56545708	0.115678703	4.59647105	5.05050229
6-9	unrestricted	rp	V3	right	ventral	665	4.85970036	3.19678322	0.123965936	4.6162879	5.10311282
6-9	unrestricted	rp	V2	left	dorsal	997	4.59283283	3.1186245	0.0987678289	4.3990159	4.78664974

										2	
6-9	unrestricted	rp	V2	right	dorsal	1241	4.76031944	3.21594819	0.0912899885	4.58121954	4.93941935
6-9	unrestricted	rp	V2	left	ventral	1363	4.44951628	3.77804645	0.102333862	4.2487672	4.65026537
6-9	unrestricted	rp	V2	right	ventral	1393	3.30672238	3.30568466	0.0885698408	3.13297761	3.48046715
6-9	unrestricted	rp	V1	left	dorsal	2267	2.57409326	2.91005473	0.0611188814	2.45423843	2.69394808
6-9	unrestricted	rp	V1	right	dorsal	1463	2.96008785	3.12941343	0.0818164778	2.79959764	3.12057807
6-9	unrestricted	rp	V1	left	ventral	1400	3.1735171	3.14190686	0.083970993	3.00879447	3.33823974
6-9	unrestricted	rp	V1	right	ventral	1561	3.73258934	3.51419299	0.088945536	3.55812393	3.90705475
6-9	unrestricted	stgd	V1	left	dorsal	670	3.14850749	3.39169278	0.131032524	2.89122299	3.40579198
6-9	unrestricted	stgd	V1	right	dorsal	701	3.77092835	3.26188956	0.123199868	3.52904282	4.01281389
6-9	unrestricted	stgd	V1	left	ventral	362	3.45806728	2.77777148	0.145996428	3.1709569	3.74517759

										7	
6-9	unrestricted	stgd	V1	right	ventral	999	3.70747613	3.43971751	0.108827846	3.49391848	3.92103378
6-9	unrestricted	stgd	V2	left	dorsal	596	5.65692998	3.10747216	0.127287019	5.4069435	5.90691647
6-9	unrestricted	stgd	V2	right	dorsal	870	5.25729231	3.23176298	0.109567026	5.04224537	5.47233925
6-9	unrestricted	stgd	V2	left	ventral	284	3.54622353	3.52304576	0.209054304	3.13472481	3.95772224
6-9	unrestricted	stgd	V2	right	ventral	451	2.68390183	3.15979472	0.148788922	2.39149445	2.97630921
6-9	unrestricted	stgd	V3	left	dorsal	321	4.91981332	3.4071539	0.190168786	4.5456743	5.29395234
6-9	unrestricted	stgd	V3	right	dorsal	269	6.19114539	2.53596475	0.1546205	5.88672002	6.49557076
6-9	unrestricted	stgd	V3	left	ventral	335	3.89715877	3.49142946	0.190757169	3.52192187	4.27239566
6-9	unrestricted	stgd	V3	right	ventral	498	1.97565357	2.75445102	0.123429902	1.73314484	2.2181623
1-3	limited	controls	V3	left	dorsal	6498	2.15834373	1.42455498	0.0176721489	2.1237005	2.19298696

1-3	limited	controls	V3	left	ventral	4782	2.61464552	1.81948752	0.0263114204	2.56306302	2.66622801
1-3	limited	controls	V3	right	dorsal	7278	1.92806132	1.19081545	0.0139584899	1.90069863	1.955424
1-3	limited	controls	V3	right	ventral	5597	2.13175504	1.64663896	0.022010035	2.08860683	2.17490325
1-3	limited	controls	V2	left	dorsal	8937	2.38093448	1.48346262	0.0156920878	2.35017439	2.41169457
1-3	limited	controls	V2	left	ventral	8900	2.34053707	1.67934657	0.017801038	2.30564293	2.37543121
1-3	limited	controls	V2	right	dorsal	11994	2.10471607	1.33064559	0.0121501147	2.08089988	2.12853226
1-3	limited	controls	V2	right	ventral	7427	2.20794326	1.65196611	0.0191687777	2.17036702	2.2455195
1-3	limited	controls	V1	left	dorsal	10670	2.1894171	1.55460457	0.0150500426	2.15991621	2.21891799
1-3	limited	controls	V1	left	ventral	10955	2.0159779	1.55567537	0.0148632159	1.98684332	2.04511249
1-3	limited	controls	V1	right	dorsal	10864	1.89913481	1.35704232	0.0130196261	1.87361397	1.92465565

1-3	limited	controls	V1	right	ventral	7632	2.23145276	1.80472969	0.0206582239	2.19095696	2.27194855
3-6	limited	controls	V3	left	dorsal	4808	4.38301796	2.04218689	0.0294518958	4.32527876	4.44075715
3-6	limited	controls	V3	left	ventral	2713	4.87548662	2.34638292	0.045047842	4.78715505	4.96381819
3-6	limited	controls	V3	right	dorsal	3743	4.26676755	1.76514499	0.0288516377	4.21020108	4.32333401
3-6	limited	controls	V3	right	ventral	3234	4.58467247	2.63095131	0.04626396	4.49396281	4.67538212
3-6	limited	controls	V2	left	dorsal	5467	4.02333473	2.27878085	0.0308196729	3.9629159	4.08375356
3-6	limited	controls	V2	left	ventral	5487	4.07197256	2.75363889	0.0371740182	3.99909674	4.14484837
3-6	limited	controls	V2	right	dorsal	5238	4.21472855	2.20132629	0.0304159702	4.15510056	4.27435653
3-6	limited	controls	V2	right	ventral	4726	3.68356457	2.72130328	0.0395849487	3.60595962	3.76116953
3-6	limited	controls	V1	left	dorsal	6593	3.42322866	2.30186393	0.0283490239	3.36765539	3.47880193

3-6	limited	controls	V1	left	ventral	5945	3.29837637	2.69634839	0.0349703578	3.22982176	3.36693097
3-6	limited	controls	V1	right	dorsal	5239	3.47026085	2.51131365	0.0346957881	3.40224264	3.53827906
3-6	limited	controls	V1	right	ventral	5525	3.39997219	2.8458893	0.0382870461	3.32491451	3.47502987
6-9	limited	controls	V3	left	dorsal	2811	4.69517815	3.11932905	0.0588343239	4.5798153	4.81054099
6-9	limited	controls	V3	left	ventral	1973	4.17085779	3.29299048	0.0741356215	4.02546541	4.31625018
6-9	limited	controls	V3	right	dorsal	2013	5.2467156	2.74130185	0.0610991223	5.12689144	5.36653976
6-9	limited	controls	V3	right	ventral	2638	4.45914151	3.44917668	0.0671549523	4.32745978	4.59082324
6-9	limited	controls	V2	left	dorsal	3655	4.36760849	3.51357968	0.0581173918	4.25366275	4.48155423
6-9	limited	controls	V2	left	ventral	3160	3.88542978	3.58531006	0.0637798037	3.76037575	4.01048381
6-9	limited	controls	V2	right	dorsal	3852	4.18386896	3.44780812	0.0555520319	4.07495474	4.29278317

6-9	limited	controls	V2	right	ventral	3743	3.32253194	3.44401675	0.0562931229	3.21216375	3.43290013
6-9	limited	controls	V1	left	dorsal	3583	3.89267805	3.3431827	0.0558517398	3.78317365	4.00218245
6-9	limited	controls	V1	left	ventral	3813	2.88169298	3.23571549	0.0524006803	2.77895692	2.98442905
6-9	limited	controls	V1	right	dorsal	4032	3.23564922	3.38361378	0.0532869082	3.13117743	3.34012101
6-9	limited	controls	V1	right	ventral	4078	2.84719329	3.28992024	0.0515183279	2.74618924	2.94819734

9.7.4. Supplementary Table 4 Descriptive Statistics for pRF eccentricity

bin	vision condition	group	ROI	hemisphere	stream	N	Mean	Std.Dev.	Std.Err	-95.00%	+95.00%
1-3	unrestricted	controls	V1	left	dorsal	9984	1.909696	0.534531	0.00535	1.89921	1.920183
1-3	unrestricted	controls	V1	left	ventral	10727	1.879599	0.534605	0.005162	1.869481	1.889716
1-3	unrestricted	controls	V1	right	dorsal	10985	1.883608	0.52992	0.005056	1.873697	1.893518
1-3	unrestricted	controls	V1	right	ventral	7122	1.976232	0.547644	0.006489	1.963511	1.988953
1-3	unrestricted	rp	V1	left	dorsal	3453	1.906228	0.528883	0.009	1.888582	1.923875
1-3	unrestricted	rp	V1	left	ventral	4229	1.988433	0.529328	0.00814	1.972475	2.004391
1-3	unrestricted	rp	V1	right	dorsal	3699	1.83177	0.521245	0.00857	1.814967	1.848574
1-3	unrestricted	rp	V1	right	ventral	2841	1.871909	0.543239	0.010192	1.851925	1.891893
1-3	unrestricted	stgd	V1	left	dorsal	721	2.061041	0.526978	0.019626	2.022511	2.099572
1-3	unrestricted	stgd	V1	left	ventral	299	1.854908	0.554838	0.032087	1.791762	1.918054
1-3	unrestricted	stgd	V1	right	dorsal	558	2.140042	0.539003	0.022818	2.095222	2.184861

1-3	unrestricted	stgd	V1	right	ventral	436	1.949255	0.583405	0.02794	1.894341	2.00417
3-6	unrestricted	controls	V1	left	dorsal	6298	4.325812	0.862405	0.010867	4.304509	4.347115
3-6	unrestricted	controls	V1	left	ventral	5922	4.291624	0.870238	0.011308	4.269456	4.313793
3-6	unrestricted	controls	V1	right	dorsal	5347	4.268817	0.868551	0.011878	4.245531	4.292102
3-6	unrestricted	controls	V1	right	ventral	5514	4.347512	0.84102	0.011326	4.325308	4.369715
3-6	unrestricted	rp	V1	left	dorsal	2647	4.337221	0.885053	0.017203	4.303489	4.370953
3-6	unrestricted	rp	V1	left	ventral	2499	4.189516	0.821234	0.016428	4.157303	4.22173
3-6	unrestricted	rp	V1	right	dorsal	2143	4.262708	0.838323	0.018109	4.227195	4.298222
3-6	unrestricted	rp	V1	right	ventral	1891	4.302947	0.867564	0.019951	4.26382	4.342075
3-6	unrestricted	stgd	V1	left	dorsal	610	4.231974	0.833888	0.033763	4.165667	4.29828
3-6	unrestricted	stgd	V1	left	ventral	248	4.433196	0.919042	0.058359	4.31825	4.548141
3-6	unrestricted	stgd	V1	right	dorsal	767	4.368508	0.881222	0.031819	4.306045	4.430971
3-6	unrestricted	stgd	V1	right	ventral	633	4.503591	0.841801	0.033459	4.437887	4.569294
6-9	unrestricted	controls	V1	left	dorsal	4598	7.542853	0.809446	0.011937	7.519451	7.566256

6-9	unrestricted	controls	V1	left	ventral	4248	7.532046	0.78894	0.012105	7.508314	7.555777
6-9	unrestricted	controls	V1	right	dorsal	4522	7.575044	0.776983	0.011554	7.552392	7.597696
6-9	unrestricted	controls	V1	right	ventral	4872	7.492509	0.784422	0.011238	7.470477	7.514541
6-9	unrestricted	rp	V1	left	dorsal	2267	7.542068	0.799047	0.016782	7.509158	7.574978
6-9	unrestricted	rp	V1	left	ventral	1400	7.458397	0.800611	0.021397	7.416423	7.500371
6-9	unrestricted	rp	V1	right	dorsal	1463	7.510781	0.779622	0.020383	7.470798	7.550763
6-9	unrestricted	rp	V1	right	ventral	1561	7.572278	0.798929	0.020221	7.532615	7.611942
6-9	unrestricted	stgd	V1	left	dorsal	670	7.746364	0.736122	0.028439	7.690523	7.802204
6-9	unrestricted	stgd	V1	left	ventral	362	7.531526	0.941779	0.049499	7.434184	7.628869
6-9	unrestricted	stgd	V1	right	dorsal	701	7.568723	0.80569	0.03043	7.508977	7.628469
6-9	unrestricted	stgd	V1	right	ventral	999	7.674541	0.780677	0.0247	7.626072	7.72301
1-3	unrestricted	controls	V2	left	dorsal	8994	1.964409	0.531993	0.00561	1.953413	1.975405
1-3	unrestricted	controls	V2	left	ventral	8251	1.943869	0.541745	0.005964	1.932178	1.95556
1-3	unrestricted	controls	V2	right	dorsal	12219	1.912086	0.527211	0.004769	1.902738	1.921435

1-3	unrestricted	controls	V2	right	ventral	7577	2.011065	0.541692	0.006223	1.998866	2.023264
1-3	unrestricted	rp	V2	left	dorsal	2843	2.085192	0.50828	0.009533	2.0665	2.103884
1-3	unrestricted	rp	V2	left	ventral	3553	1.979919	0.530274	0.008896	1.962477	1.997361
1-3	unrestricted	rp	V2	right	dorsal	4858	1.810339	0.522226	0.007493	1.795651	1.825028
1-3	unrestricted	rp	V2	right	ventral	2296	1.981109	0.534469	0.011154	1.959236	2.002982
1-3	unrestricted	stgd	V2	left	dorsal	504	2.109024	0.576821	0.025694	2.058544	2.159504
1-3	unrestricted	stgd	V2	left	ventral	48	2.189172	0.471262	0.068021	2.052332	2.326013
1-3	unrestricted	stgd	V2	right	dorsal	473	2.114084	0.537195	0.0247	2.065548	2.16262
1-3	unrestricted	stgd	V2	right	ventral	188	1.83427	0.441885	0.032228	1.770693	1.897847
3-6	unrestricted	controls	V2	left	dorsal	5628	4.242794	0.833346	0.011108	4.221018	4.264571
3-6	unrestricted	controls	V2	left	ventral	5529	4.321173	0.859196	0.011555	4.298521	4.343825
3-6	unrestricted	controls	V2	right	dorsal	5174	4.21732	0.853103	0.01186	4.19407	4.240571
3-6	unrestricted	controls	V2	right	ventral	5116	4.297058	0.866651	0.012117	4.273305	4.320812
3-6	unrestricted	rp	V2	left	dorsal	1853	4.266023	0.880373	0.020452	4.225912	4.306134

3-6	unrestricted	rp	V2	left	ventral	1884	4.308715	0.895506	0.020631	4.268253	4.349178
3-6	unrestricted	rp	V2	right	dorsal	2036	4.242449	0.875188	0.019396	4.204411	4.280487
3-6	unrestricted	rp	V2	right	ventral	1943	4.305495	0.800828	0.018168	4.269864	4.341125
3-6	unrestricted	stgd	V2	left	dorsal	767	4.420938	0.855444	0.030888	4.360302	4.481573
3-6	unrestricted	stgd	V2	left	ventral	172	4.746704	0.875494	0.066756	4.614932	4.878475
3-6	unrestricted	stgd	V2	right	dorsal	980	4.458826	0.867114	0.027699	4.40447	4.513182
3-6	unrestricted	stgd	V2	right	ventral	293	4.483449	0.80078	0.046782	4.391376	4.575522
6-9	unrestricted	controls	V2	left	dorsal	3733	7.601487	0.828418	0.013559	7.574903	7.62807
6-9	unrestricted	controls	V2	left	ventral	3362	7.463232	0.814526	0.014048	7.435689	7.490775
6-9	unrestricted	controls	V2	right	dorsal	3500	7.585342	0.834712	0.014109	7.557679	7.613005
6-9	unrestricted	controls	V2	right	ventral	3860	7.518972	0.789211	0.012703	7.494067	7.543877
6-9	unrestricted	rp	V2	left	dorsal	997	7.494986	0.869607	0.027541	7.440942	7.549031
6-9	unrestricted	rp	V2	left	ventral	1363	7.536666	0.835376	0.022627	7.492278	7.581055
6-9	unrestricted	rp	V2	right	dorsal	1241	7.425964	0.798323	0.022662	7.381505	7.470424

6-9	unrestricted	rp	V2	right	ventral	1393	7.557492	0.80016	0.021439	7.515436	7.599548
6-9	unrestricted	stgd	V2	left	dorsal	596	7.354157	0.845108	0.034617	7.286171	7.422143
6-9	unrestricted	stgd	V2	left	ventral	284	7.798984	0.806882	0.04788	7.704738	7.893229
6-9	unrestricted	stgd	V2	right	dorsal	870	7.464806	0.797205	0.027028	7.411759	7.517853
6-9	unrestricted	stgd	V2	right	ventral	451	7.542038	0.659263	0.031043	7.48103	7.603047
1-3	unrestricted	controls	V3	left	dorsal	6404	1.961766	0.562552	0.00703	1.947986	1.975547
1-3	unrestricted	controls	V3	left	ventral	4135	1.975367	0.518761	0.008067	1.959551	1.991183
1-3	unrestricted	controls	V3	right	dorsal	7651	1.846366	0.531871	0.006081	1.834447	1.858286
1-3	unrestricted	controls	V3	right	ventral	5353	1.920088	0.546272	0.007466	1.905451	1.934725
1-3	unrestricted	rp	V3	left	dorsal	2152	1.84705	0.532155	0.011471	1.824554	1.869546
1-3	unrestricted	rp	V3	left	ventral	1662	2.001394	0.533679	0.013091	1.975718	2.02707
1-3	unrestricted	rp	V3	right	dorsal	3381	1.799942	0.503187	0.008654	1.782975	1.816909
1-3	unrestricted	rp	V3	right	ventral	2018	2.056793	0.515805	0.011482	2.034275	2.079311
1-3	unrestricted	stgd	V3	left	dorsal	418	2.150148	0.585924	0.028658	2.093815	2.206481

1-3	unrestricted	stgd	V3	left	ventral	24	2.265617	0.467784	0.095486	2.068089	2.463145
1-3	unrestricted	stgd	V3	right	dorsal	388	2.074903	0.580386	0.029465	2.016973	2.132834
1-3	unrestricted	stgd	V3	right	ventral	307	1.854729	0.509383	0.029072	1.797523	1.911935
3-6	unrestricted	controls	V3	left	dorsal	4956	4.278714	0.850772	0.012085	4.255022	4.302406
3-6	unrestricted	controls	V3	left	ventral	3045	4.304288	0.844756	0.015309	4.274272	4.334304
3-6	unrestricted	controls	V3	right	dorsal	4311	4.352179	0.870438	0.013257	4.326188	4.37817
3-6	unrestricted	controls	V3	right	ventral	3693	4.284484	0.850457	0.013995	4.257046	4.311922
3-6	unrestricted	rp	V3	left	dorsal	1965	4.376185	0.835622	0.018851	4.339216	4.413155
3-6	unrestricted	rp	V3	left	ventral	992	4.239218	0.882811	0.028029	4.184215	4.294222
3-6	unrestricted	rp	V3	right	dorsal	1233	4.307132	0.88872	0.025309	4.257478	4.356787
3-6	unrestricted	rp	V3	right	ventral	1360	4.206952	0.845404	0.022924	4.161982	4.251923
3-6	unrestricted	stgd	V3	left	dorsal	618	4.350275	0.904762	0.036395	4.278802	4.421748
3-6	unrestricted	stgd	V3	left	ventral	78	4.534838	0.7937	0.089869	4.355887	4.71379
3-6	unrestricted	stgd	V3	right	dorsal	419	4.38485	0.851011	0.041575	4.303128	4.466571

3-6	unrestricted	stgd	V3	right	ventral	123	4.412347	0.894122	0.08062	4.252751	4.571942
6-9	unrestricted	controls	V3	left	dorsal	3061	7.45215	0.827355	0.014954	7.422829	7.481471
6-9	unrestricted	controls	V3	left	ventral	1887	7.532603	0.824649	0.018984	7.495371	7.569834
6-9	unrestricted	controls	V3	right	dorsal	2419	7.369974	0.838134	0.017041	7.336557	7.40339
6-9	unrestricted	controls	V3	right	ventral	2726	7.527666	0.798052	0.015285	7.497695	7.557638
6-9	unrestricted	rp	V3	left	dorsal	1161	7.368245	0.856211	0.025128	7.318943	7.417547
6-9	unrestricted	rp	V3	left	ventral	950	7.538992	0.771134	0.025019	7.489893	7.58809
6-9	unrestricted	rp	V3	right	dorsal	836	7.410265	0.821677	0.028418	7.354486	7.466045
6-9	unrestricted	rp	V3	right	ventral	665	7.43876	0.80621	0.031263	7.377373	7.500147
6-9	unrestricted	stgd	V3	left	dorsal	321	7.476211	0.890804	0.04972	7.378392	7.57403
6-9	unrestricted	stgd	V3	left	ventral	335	7.855413	0.755114	0.041256	7.774258	7.936568
6-9	unrestricted	stgd	V3	right	dorsal	269	7.300448	0.821391	0.050081	7.201845	7.39905
6-9	unrestricted	stgd	V3	right	ventral	498	7.902917	0.625678	0.028037	7.847831	7.958003
1-3	limited	controls	V1	left	dorsal	10670	1.927213	0.536932	0.005198	1.917024	1.937402

1-3	limited	controls	V1	left	ventral	10955	1.907955	0.53398	0.005102	1.897954	1.917955
1-3	limited	controls	V1	right	dorsal	10864	1.920345	0.522837	0.005016	1.910513	1.930178
1-3	limited	controls	V1	right	ventral	7632	1.946538	0.541497	0.006198	1.934387	1.958688
3-6	limited	controls	V1	left	dorsal	6593	4.248499	0.848727	0.010453	4.228008	4.268989
3-6	limited	controls	V1	left	ventral	5945	4.28455	0.853105	0.011064	4.26286	4.30624
3-6	limited	controls	V1	right	dorsal	5239	4.286372	0.88462	0.012222	4.262412	4.310331
3-6	limited	controls	V1	right	ventral	5525	4.355936	0.874246	0.011762	4.332878	4.378993
6-9	limited	controls	V1	left	dorsal	3583	7.431492	0.828819	0.013846	7.404344	7.458639
6-9	limited	controls	V1	left	ventral	3813	7.428199	0.78482	0.01271	7.403281	7.453118
6-9	limited	controls	V1	right	dorsal	4032	7.556948	0.800121	0.012601	7.532244	7.581653
6-9	limited	controls	V1	right	ventral	4078	7.489246	0.787501	0.012332	7.465069	7.513423
1-3	limited	controls	V2	left	dorsal	8937	1.956312	0.512815	0.005425	1.945678	1.966945
1-3	limited	controls	V2	left	ventral	8900	1.936277	0.530039	0.005618	1.925263	1.94729
1-3	limited	controls	V2	right	dorsal	11994	1.889703	0.509855	0.004655	1.880578	1.898829

1-3	limited	controls	V2	right	ventral	7427	1.972954	0.545035	0.006324	1.960556	1.985351
3-6	limited	controls	V2	left	dorsal	5467	4.32455	0.85663	0.011586	4.301837	4.347262
3-6	limited	controls	V2	left	ventral	5487	4.346551	0.881694	0.011903	4.323217	4.369885
3-6	limited	controls	V2	right	dorsal	5238	4.281524	0.867364	0.011984	4.258029	4.305018
3-6	limited	controls	V2	right	ventral	4726	4.303226	0.880029	0.012801	4.27813	4.328322
6-9	limited	controls	V2	left	dorsal	3655	7.488995	0.835676	0.013823	7.461894	7.516097
6-9	limited	controls	V2	left	ventral	3160	7.367773	0.820853	0.014602	7.339142	7.396404
6-9	limited	controls	V2	right	dorsal	3852	7.492973	0.818076	0.013181	7.46713	7.518815
6-9	limited	controls	V2	right	ventral	3743	7.396055	0.771505	0.01261	7.371332	7.420779
1-3	limited	controls	V3	left	dorsal	6498	1.98989	0.558177	0.006924	1.976316	2.003464
1-3	limited	controls	V3	left	ventral	4782	1.978459	0.526549	0.007614	1.963531	1.993387
1-3	limited	controls	V3	right	dorsal	7278	1.848193	0.550257	0.00645	1.83555	1.860837
1-3	limited	controls	V3	right	ventral	5597	1.923032	0.526019	0.007031	1.909248	1.936816
3-6	limited	controls	V3	left	dorsal	4808	4.247769	0.859095	0.01239	4.22348	4.272058

3-6	limited	controls	V3	left	ventral	2713	4.307513	0.877882	0.016854	4.274465	4.340562
3-6	limited	controls	V3	right	dorsal	3743	4.282198	0.853074	0.013944	4.25486	4.309536
3-6	limited	controls	V3	right	ventral	3234	4.355428	0.915257	0.016094	4.323872	4.386984
6-9	limited	controls	V3	left	dorsal	2811	7.415831	0.817187	0.015413	7.385609	7.446054
6-9	limited	controls	V3	left	ventral	1973	7.533503	0.795405	0.017907	7.498384	7.568622
6-9	limited	controls	V3	right	dorsal	2013	7.341682	0.840029	0.018723	7.304964	7.378401
6-9	limited	controls	V3	right	ventral	2638	7.463794	0.803726	0.015648	7.433109	7.494478

9.1.1. 9.7.5. Supplementary Table 5 Pearson correlation between pRF size and Humphrey test

RP		right V1	right V2	right V3	left V1	left V2	left V3
center left eye	r	0.2436	0.0081	0.2001			
		p=.301	p=.973	p=.398			
center right eye	r				0.3203	0.2802	0.2131
					p=.169	p=.231	p=.367
fullfield left eye	r	0.1707	-0.0834	0.1362			
		p=.459	p=.719	p=.556			
fullfield right eye	r				0.2617	0.1194	0.1615
					p=.252	p=.606	p=.484
STGD							
center left eye	r	0.3526	0.3548	0.4174			
		p=.117	p=.115	p=.060			
center right eye	r				-0.1051	-0.4185	-0.3865
					p=.650	p=.059	p=.083
fullfield left eye	r	0.314	0.296	0.395			
		p=.164	p=.192	p=.076			
fullfield right eye	r				-0.206	-0.368	-0.246
					p=.370	p=.100	p=.282

9.7.6. Supplementary Table 6 Local maxima for motion-acuity tasks for separate tasks

				MNI coordinates		
Contrast	**Region**	**Cluster size**	**T**	**x**	**y**	**z**
Full > RP (fast negative)	right V1	1675	7.14	10	-84	2
	left V1		6.91	-8	-80	0
	right V1		6.66	10	-92	10
Full > RP (slow negative)	right V2	1987	6.44	12	-90	16
	left V1		5.56	-8	-80	0
	right V2		5.52	10	-72	-4
	left precentral gyrus	188	5.28	-40	2	50
	left precentral gyrus		3.85	-28	-4	44
Full > RP (fast positive)	right V1	253	5.05	10	-84	2
	right V1		4.60	12	-86	12
	right V1		4.15	10	-72	2
	left V2	153	4.41	-10	-80	-2
	left V1		3.86	-12	-96	8
	left V1		3.45	-8	-74	8
Full > RP (slow positive)	right V1	169	5.17	12	-88	12
	right V1		4.75	10	-84	4
	right V2		3.53	12	-74	0
Limited > RP (fast negative)	right V2	175	5.44	8	-92	14
	right V1		3.94	12	-88	6
	right V2		3.74	14	-84	-6
Limited vs RP (slow negative)	right V2	152	5.30	10	-92	14
	right V1		4.10	10	-86	8

9.7.7. Supplementary Table 7 Local maxima for motion-acuity tasks for separate tasks

				MNI coordinates		
Contrast	**Region**	**Cluster size**	**T**	**x**	**y**	**z**
Full > RP (fast negative)	right V1	1675	7.14	10	-84	2
	left V1		6.91	-8	-80	0
	right V1		6.66	10	-92	10
Full > RP (slow negative)	right V2	1987	6.44	12	-90	16
	left V1		5.56	-8	-80	0
	right V2		5.52	10	-72	-4
	left precentral gyrus	188	5.28	-40	2	50
	left precentral gyrus		3.85	-28	-4	44
Full > RP (fast positive)	right V1	253	5.05	10	-84	2
	right V1		4.60	12	-86	12
	right V1		4.15	10	-72	2
	left V2	153	4.41	-10	-80	-2
	left V1		3.86	-12	-96	8
	left V1		3.45	-8	-74	8
Full > RP (slow positive)	right V1	169	5.17	12	-88	12
	right V1		4.75	10	-84	4
	right V2		3.53	12	-74	0
Limited > RP (fast negative)	right V2	175	5.44	8	-92	14
	right V1		3.94	12	-88	6
	right V2		3.74	14	-84	-6
Limited vs RP (slow negative)	right V2	152	5.30	10	-92	14
	right V1		4.10	10	-86	8

9. Publications of the PhD candidate

1. Kozak, A., Wieteska, M., **Ninghetto, M.,** Szulborski, K., Gałecki, T., Szaflik, J., & Burnat, K. (2021). Motion-Based Acuity Task: Full Visual Field Measurement of Shape and Motion Perception. *Translational Vision Science & technology, 10*(1), 9.
2. Kozak, A., **Ninghetto, M.**, Wieteska, M., Fiedorowicz, M., Wełniak-Kamińska, M., Kossowski, B., Eysel, U. T., Arckens, L., & Burnat, K. (2024). Visual training after central retinal loss limits structural white matter degradation: an MRI study. *Behavioral and Brain Functions*, 20(1), 13.
3. Mueller, S. C., De Franceschi, M., Brzozowska, J., Herman, A. M., **Ninghetto, M.,** Burnat, K., Grymowicz, M., & Marchewka, A. (2024). An influence of menopausal symptoms on mental health, emotion perception, and quality of life: a multi-faceted approach. *Quality of Life Research: an International Journal of Quality of Life Aspects of Treatment, Care and Rehabilitation, 33*(7), 1925–1935.
4. **Ninghetto, M.,** Gammeri, R., Miccolis, R., Nobili, M., Salatino, A., & Ricci, R. (2019). Effects of Repeated Sessions of Transcranial Direct Current Stimulation on Major Depressive Disorder and Cognition. *The journal of ECT, 35*(3), e32–e33.
5. ***Ninghetto, M.,** Keliris, G. A., Szulborski, K., Gałecki, T., Kossowski, B., Panneman, D., Cremers, F. P. M., Ołdak, M., Szaflik, J. P., & Burnat, K. (under review). Cortical response to transient and long-term visual field loss. Cerebral Cortex.
6. ***Ninghetto, M.,** Kozak, A., Gałecki, T., Szulborski, K., Szaflik, J. P., Ołdak, M., Marchewka, A., & Burnat, K. (2024). Good vision without peripheries: behavioral and fMRI evidence. *Scientific Reports, 14*(1), 26264.
7. **Ninghetto, M.,** Wieteska, M., Kozak, A., Szulborski, K., Gałecki, T., Szaflik, J., Burnat, K. (2024). Motion-Acuity Test for Visual Field Acuity Measurement with Motion-Defined Shapes. *Journal of Visualized Experiments: JoVE,* (204), e66272.
8. Salatino, A., Miccolis, R., Gammeri, R., **Ninghetto, M.,** Belli, F., Nobili, M., Mouraux, A., & Ricci, R. (2022). Improvement of Impulsivity and Decision Making by Transcranial Direct Current Stimulation of the Dorsolateral Prefrontal Cortex in a Patient with Gambling Disorder. *Journal of Gambling Studies, 38*(2), 627–634.
9. Sarasso, P., **Ninghetto, M.**, Salatino, A., Ronga, I., Bongiardina, A., Iarrobino, I., Neppi-Modona, M., & Ricci, R. (2019). Everything is (still) illuminated: Dual right cathodal-left anodal tDCS of PPC prevents fatigue on a visual detection task. *Brain Stimulation, 12*(1), 187–189.
10. Torta, D. M. E., **Ninghetto, M.**, Ricci, R., & Legrain, V. (2020). Rating the Intensity of a Laser Stimulus, but Not Attending to Changes in Its Location or Intensity Modulates the Laser-Evoked Cortical Activity. *Frontiers in Human Neuroscience, 14*, 120.

* – the results are presented in PhD thesis